An application of Quantitative Systems Pharmacology to Repurpose Drugs for Non-Alcoholic Fatty Liver Disease

by

Daniel Edward Lefever

BSA, University of Georgia, 2014

Submitted to the Graduate Faculty of the

School of Medicine in partial fulfillment

of the requirements for the degree of

Doctor of Philosophy

University of Pittsburgh

2023

UNIVERSITY OF PITTSBURGH

SCHOOL OF MEDICINE

This thesis or dissertation was presented

by

Daniel Edward Lefever

It was defended on

January 6, 2023

and approved by

Ivet Bahar, Ph.D., Distinguished Professor & John K. Vries Chair, Department of Computational and Systems Biology, University of Pittsburgh

Satdarshan P. Monga, MD, Professor & Endowed Chair, Department of Pathology, University of Pittsburgh

Dennis Kostka, Ph.D., Associate Professor, Department of Developmental Biology, University of Pittsburgh

Andrew M. Stern, Ph.D., Research Associate Professor, Department of Computational and Systems Biology, University of Pittsburgh

Thesis Advisor/Dissertation Directors:

D. Lansing Taylor, Ph.D., Distinguished Professor and Allegheny Foundation Professor of Computational and Systems Biology, Department of Computational and Systems Biology, University of Pittsburgh

Albert Gough, Ph.D., Research Associate Professor, Department of Computational and Systems Biology, University of Pittsburgh

An application of Quantitative Systems Pharmacology to Repurpose Drugs for Non-Alcoholic Fatty Liver Disease

Daniel Edward Lefever, PhD

University of Pittsburgh, 2023

Biological research, like most other fields of research and technology, has experienced an exponential growth in productivity since the 1950's. However, drug discovery as one of the main practical applications of biological research has become exponentially more expensive and the efficiency of success remains low. Among the most important reasons for this low efficiency is that several major unmet medical needs involve diseases that are complex and heterogeneous, presenting challenges for traditional drug discovery approaches. Non-alcoholic fatty liver disease (NAFLD) is one such disease in which despite billions being spent, the approaches used by current drug discovery efforts has not yielded any Food and Drug Administration (FDA) approved drugs in the US. NAFLD is a disease driven by multiple independent pathways and molecular targets which may not be amenable to single targeted therapeutics. This dissertation demonstrates how a relatively new approach to drug discovery, Quantitative Systems Pharmacology (QSP), can be used to discover drugs for NAFLD by predicting existing drugs for repurposing and by identifying disease networks comprising potential molecular targets for novel drug discovery.

Chapter 1 gives an overview of NAFLD and the rationale for using QSP. Chapter 2 describes results using patient transcriptome data to comprehensively and unbiasedly define disease states that promote NAFLD progression. In Chapter 3, the Library of Integrated Network-Based Cellular Signatures (LINCS) L1000 database was used to predict drugs able to normalize these disease states and were then experimentally tested in a human liver acinus microphysiology system (LAMPS) of NAFLD. A proof-of-concept study in LAMPS demonstrated mitigation of steatosis, inflammation, and fibrosis especially with drug combinations. Chapter 4 further establishes the clinical relevancy of LAMPS as a model of NAFLD. Currently, experimental testing of more predicted compounds is being performed. In conjunction with iPSC-derived cells, this approach has the potential for developing personalized NAFLD therapeutic strategies, informing disease mechanisms, and defining optimal cohorts of patients for clinical trials.

Table of Contents

List of Tables

List of Figures

Preface

I want to start out by thanking all of the people who have helped over the years to finish my PhD. First and foremost, my advisors Lans and Bert for their scientific guidance. I'm extremely grateful for all the time Andy spent helping me to drive this project completion. All of the members of the UPDDI, especially Mark, Richard, Manush, Summer, Celeste, and Julio for all the lab work performed on my behalf, and emotional support. Neil, Shari for helping me through many difficult situations. I could not have made it through grad school without Scott, Kylia, Ricardo, and the rest of the ISB students. My family, notably my mom, dad, grandma, Joseph, and James for all their support. All of the people from the CMU and Pitt ballroom clubs, especially Bassam, and Matias have helped me stay sane coming out of the pandemic. I would like to thank Jennifer and my cat Orange.

1.0 Introduction

1.1 NAFLD background

1.1.1 NAFLD is a complex spectrum of liver diseases

NAFLD consists of a spectrum of potentially progressive disease states that, within a heterogeneous patient population, can range in severity from being clinically asymptomatic to becoming fatal [1]. Fatty liver diseases were first recognized by clinicians in the 1800's in sedentary individuals with unhealthy diets who overconsumed food and alcohol [2]. At that time, little distinction was made based on the disease etiology [2]. It was not until the 1980s that NAFLD was recognized as an independent condition [3]. As implied in the name, it shares many histological features with alcoholic liver disease [3]. The distinction is based on the underlying etiology; however, some morphological features are more prevalent in alcoholic liver disease than NAFLD [3]. Today, NAFLD is considered the hepatic manifestation of metabolic syndrome, and has been proposed by some gastroenterologists to be renamed metabolic associated fatty liver disease (MAFLD) to reflect this newfound appreciation of the disease [4].

Non-alcoholic fatty liver (NAFL, also called simple steatosis) is at the least severe end of the NAFLD spectrum, and is diagnosed when the liver contains ≥5% fat **(Figure 1A)** [5]. Patients at this stage rarely have liver related complications [6]. NAFL is contrasted with non-alcoholic steatohepatitis (NASH), by the presence of notable inflammation, hepatocyte damage (i.e., ballooning), and often pericellular fibrosis (**Figure 1B)** [1, 7]. NAFL is considered the non-progressive form of NAFLD, whereas NASH is progressive [8]. Patients with NASH are at greater risk than those with NAFL of developing cirrhosis and then end-stage liver disease (**Figure 1C)** [9]**.** If the disease progresses to this point, the only available treatment option is liver transplantation [9]. NASH can also lead to hepatocellular carcinoma (HCC) that can progress insidiously before cirrhosis is diagnosed (**Figure 1D)** [10].

Clinically NAFLD is diagnosed by observing a characteristic pattern of steatosis, inflammation, and fibrosis on a liver biopsy [11] (see **Figure 1** for representative images). Non-invasive methods have been developed but are not considered accurate enough for definitive diagnosis [12]. Due to the invasive nature, risk to the patient, and logistical requirements, biopsies are kept to a minimum [12]. This, combined with the fact that the disease is often subclinical, means that a diagnosis is not made until the pathophysiology has progressed to a late stage.

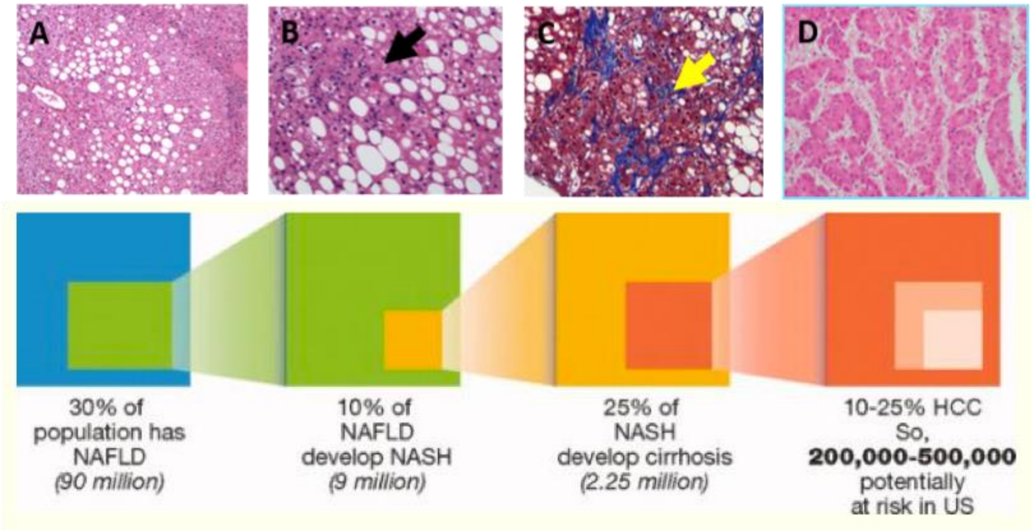

Figure 1. Natural progression of NAFLD and pathological hallmarks of NASH, cirrhosis, and HCC

A) H&E showing macrosteatosis in NAFLD; **B)** NASH is characterized by a combination of macroseatosis & immune cell infiltration (black arrow); **C)** Trichrome staining shows fibrosis (yellow arrow) in cirrhosis; **D**) H&E showing HCC with hepatocyte ballooning & death. Panel **E** shows the stage-wise rates of progression, which is considered reversible until cirrhosis. Adapted with permission from [13].

1.1.2 NAFLD has a heterogenous clinical presentation

NAFLD has traditionally been thought of as a disease which linearly progresses stage-wise over the course decades (left to right in **Figure 1**). However, the clinical presentation is subject to considerable inter-patient patient heterogeneity. NAFLD is usually diagnosed incidentally because most patients, even advanced patients with compensated cirrhosis, are asymptomatic [14]. Most patients who develop NAFL will not have liver related complications nor progress to NASH [1]. However, for those that do progress to NASH, it is not uncommon for patients to cycle back and forth between NAFL and NASH [15]. Although NAFL and NASH patients are at greater risk for liver related complications than the general public, cardiovascular diseases are the major driver of mortality within these patients [1].

Fibrosis is arguably the most important feature of NAFLD, because it has the strongest association with disease severity and patient mortality [16, 17]. However, fibrosis progression, like NAFLD itself has a heterogeneous clinical presentation, and is an imperfect prognostic indicator. Typically, fibrosis will develop in patients who have developed NASH. However, some patients with NAFL and milder clinical symptoms directly develop fibrosis [18, 19]. Singh et al., showed that only ~1/3 of patients with NAFLD had fibrosis progression, the remaining patients either had no progression or an improvement of fibrosis [20]. Of those who did progress, it took an average of ~14 years for NAFL and ~7 years for NASH patients to progress 1 fibrosis stage [20]. Fibrosis progression is measured based semi-quantitative histopathological staging from 0-4; 0 being no fibrosis and 4 being cirrhosis. It should be stressed that this timeline is an average: ~20% of patients progress 3-4 fibrosis stages in <6 years [20].

1.1.3 Epidemiology and Natural History

The overall proportion of adults with some form of NAFLD is estimated to be 30% in the US [8] and 25% worldwide [9] **(Figure 1).** The prevalence varies globally but is only projected to increase worldwide: current estimates for the Middle East and South America are ~30%, Europe 24%, Asia 27%, and Africa 14% [9]. The estimates for NASH are 1.5-6.5% [9]. Among ethnic groups in the US, NAFLD is most highly prevalent in Hispanic individuals, followed by non-Hispanic whites, and then African Americans [21]. Between 5-10% of children are estimated to have some form of NAFLD [22]. NAFLD rarely directly causes complications in children. However, the long-term consequences of developing NAFLD at a young age is unknown [5].

As NAFLD is considered the hepatic manifestation of metabolic syndrome, it is strongly co-morbid with type 2 diabetes (T2D) (60-78%), and morbid obesity (60-95%) [23]. The incidence is >95% in obese individuals undergoing bariatric surgery [24]. However, despite the strong association with NAFLD and obesity, between 10-20% of normal weight individuals have NAFLD [25]. These individuals typically have a normal BMI but have features of metabolic syndrome (dyslipidemia, insulin resistance, visceral obesity, poor diet, and sedentary lifestyle) [25]. T2D has a complex bidirectional relationship with NAFLD: T2D appears to directly contribute to NAFLD progression, and vice-versa [26]. NAFLD doubles the risk of developing T2D when all other clinical features are controlled [26]. T2D appears to directly contribute to NAFLD, as well as increase the severity of disease [24].

In addition to liver failure, NAFLD can lead to the development of liver cancers, notably hepatocellular carcinoma (HCC). The 5-year survival rate for patients with HCC varies according to stage at diagnosis and treatment, but can be less than 20% [27]. The exact risk is difficult to quantify at each stage of NAFLD, however, it is clear that patients with cirrhotic NASH are at the highest risk of developing HCC [28]. The annual incidence in patients with cirrhotic NASH is .7-2.6%, and ranges from 0.04% to 0.6% in NAFLD patients without cirrhosis [28]. An estimated 15-20% of HCCs develop from NAFLD without cirrhosis [18].

The overall mortality rate for patients diagnosed with NAFLD is 26% after 15 years [1]. The most common cause of death in patients without cirrhosis is cardiovascular disease [29]. NAFLD is only projected to increase in prevalence and to become the most common cause for liver transplantation [1].

1.1.4 Genetics and Mechanisms

NAFLD is considered to be heritable, however the estimated contribution of heredity varies widely from 20-70% [30]. This wide range of estimates can be attributed to study design, confounders, and the study’s definition of NAFLD [30]. However, these estimates are similar to the ranges seen in metabolic syndrome [30]. Twin studies have given heritability estimates of 38-50% [30] for NAFLD, and ~75% for steatosis and fibrosis [31]. Studies using unrelated individuals suggests heritability of 22-34% [30].

Like most complex diseases, NAFLD is subject to the “missing heritability” problem [32], because the known variants explain 10-20% of heritability [30]. There are variants in 5 genes which are robustly associated with NAFLD: PNPLA3, TM6SF2, MBOAT7, GCKR, and HSD17B13. The PNPLA3 I148M (rs738409 C>G), TM6SF2 E167K (rs58542926 C>T), and MBOAT7 (rs641738 C>T) variants all increase steatosis and are associated with disease severity [33]. PNPLA3 I148M is not associated with increased insulin resistance, and MBOAT7 actually decreases risk for cardiovascular disease by decreasing lipids in circulation [33]. GCKR P446L is thought to contribute to NAFLD by causing aberrant lipogenesis [30]. HSD17B13 has been associated with protection from NAFLD [30].

Efforts in untangling the mechanisms of NAFLD progression have been hampered by the difficulty in recapitulating the disease phenotype in traditional models. Early research into NAFLD using either high-fat diet or leptin deficient mouse models could induce a NAFL phenotype, but this did not progress to more advanced stages seen in some patients unless treated with LPS [7]. This lead to the ‘two-hit’ hypothesis: steatosis was considered largely incidental and required a pro-inflammatory insult for NAFLD progression occur [7]. This is now considered an oversimplification, because steatosis can be directly pathogenic.

As with other metabolic diseases, NAFLD is thought to be caused by a combination of an unhealthy hypercaloric diet and sedentary lifestyle. Under healthy conditions, the liver metabolizes fatty acids via beta oxidation or exporting them as very-low-density lipoprotein [14]. Under metabolic syndrome (MS) conditions, the liver’s capacity to properly manage free-fatty acids is overwhelmed ultimately causing lipotoxicity [14]. Excessive calories, particularly in the form of carbohydrates, cause aberrant *de novo lipogenesis* leading to fat accumulation [14]. Fat also accumulates because of excessive free fatty acids being delivered to the liver [14]. Insulin resistance contributes to these processes by promoting lipolysis of adipose derived triglycerides causing excess fatty acids to be delivered to the liver [14].

The consequences of lipotoxicity result in hepatocellular injury from ER and oxidant stress, and inflammasome activation [14]. ER stress induces apoptosis through several mechanisms including aberrant activation of unfolded protein response and JNK1 [7]. Stress induced apoptosis and necroptosis releases pro-inflammatory cytokines (IL-1β), IL-6, IL-18, TNF-α, TGF-β) which recruit pro-inflammatory immune cells such as macrophages, Kupffer cells, polymorphonuclear neutrophils [14]. This further causes the recruitment of hepatic stellate cells which leads to fibrosis [14]. The inflammatory cascade can be further activated from other insults such as LPS and palmitic acid through toll-like receptors [7]. This process also activates hepatic stellate cells through TGF-β and hedgehog signaling pathways [7].

1.1.5 Gaps in understanding NAFLD have prevented finding effective treatments

Although NAFLD is currently a considerable public health burden–which is projected to only increase–there are no approved drugs for this disease. This is in spite of billions having been spent on drugs which ultimately failed in late-stage clinical trials. Currently, Resmetirom a selective THR-β agonist, is the only compound which has successfully met its phase 3 endpoints [34]. This can be attributed to the disease heterogeneity which has been difficult to both track in patients and recapitulate in traditional models.

Unlike some other metabolic diseases such as T2D, NAFLD cannot be diagnosed using a simple blood test. NAFLD requires a liver biopsy for definitive diagnosis, because non-invasive methods are too inaccurate [12]. This is an invasive method with some (albeit small) risk to the patient which limits its use in clinical and research settings [35]. Logistical issues notwithstanding, biopsies can be subject to sampling variability [36] and human error [37] that can lead to an incorrect diagnosis.

These issues together with the long time-course and patient heterogeneity make performing NAFLD clinical trials particularly challenging. Under normal circumstances, a sizable proportion of patients will have spontaneous (without treatment) regression of NAFLD. For example, Singh et al. found that 1/3 of patients had a reduction of more than 1 stage of fibrosis [20]. This can make it harder for clinical trials to observe drug efficacy [35]. It is also important to consider that the mechanisms between different subsets of patients may not necessarily be the same [14].

It is not clear from the clinical trial failures whether the trialed drugs have been targeting the wrong targets, targeting the right targets but are ineffective, or that NAFLD requires combination therapy similar to HIV [35]. Because there is no clear mechanism of NAFLD, the drugs brought to clinical trial have each been optimized to be selective for different targets [35]. Furthermore, it is not clear whether the mechanisms of disease progression differ between subsets of patients [35]. The difficulty in both characterizing NAFLD in patients and finding effective drugs reflects the trends seen with many other complex diseases. It is therefore evident that a new approach to NAFLD drug discovery is needed, which is discussed in the next subsection.

1.2 Quantitative systems pharmacology background

1.2.1 Drug development history

In early modern drug discovery history, compounds were identified using classical or forward pharmacology. This is done by testing compounds against an *in vivo* model of disease without regard to the mechanism of action (MOA). This was done because most diseases did not have established targets [38]. Targets and MOA were only elucidated after a compound was found to be promising. Starting in the 1980's, the industry as whole moved away from classical pharmacology to instead pursue reverse pharmacology. This is a reductionist approach in which compounds were tested against a molecular target, usually a protein [39]. This became possible with the advent of molecular biology in 80's, and this trend was further extended in the 90's with the genomics revolution [38]. Biological research during this time period has experienced an unprecedented level of growth. As just one example, sequencing has become many orders of magnitude cheaper and faster: the 1st human genome took $300 million and 10 years, it can now be done for less than $1000 and less than a day.

It was thought that reverse pharmacology would obviate the labor intensive, trial and error approach required for classical pharmacology. Classical pharmacology was a very manual, low throughput process: realistically only a handful of compounds could be synthesized at a given time, which were then tested in *in vivo* models [40]. This made for a necessarily slow process [40]. Reverse pharmacology became in vogue when several technologies that were developed in the 80's and 90's made it possible for high throughput screening of compounds against specific targets [40]. This should have in principle greatly increased the throughput over the classical approach [40]. However, this switch from classical to reverse pharmacology did not have the intended effect—drug discovery has continued to be inefficient and more expensive during this time.

1.2.2 Eroom's law

This phenomena in which drug discovery productivity has progressively decreased despite the exponential growth of biological research has been dubbed tongue-in-cheek as Eroom's law [39]. This is Moore's law, the observation that the number of transistors on a microchip doubles every 2 years, spelled backwards. Moore's law more generally refers to technologies that undergo accelerating change. Despite Moore's law being applicable to biological research and technologies, the number of drugs per (inflation adjusted) billion $ spent has halved every 9 years since the 1950's [39].

There are many reasons for this trend, which include the fact that the bars for safety and efficacy have become higher, meaning that it is objectively harder to get a drug approved than in prior generations [39]. However, this trend coincides with the widescale adoption of reverse pharmacology [41], and there are many reasons to suspect that this is perhaps the biggest contributor to Eroom's law. The framework of reverse pharmacology leads to the idea that diseases are caused by single targets. This is likely an oversimplification for many, if not most, complex diseases (such as NAFLD) [39]. In fact, not only do most drugs not have single targets, but drug promiscuity—as opposed to selectivity—can be responsible for efficacy [39]. It was further recognized that despite the investment in reverse pharmacology, there is evidence suggesting that first in class drugs were more often discovered through phenotypic drug discovery [38].

However, simply performing classical pharmacology in the same way it was done in the 50's would likely not automatically reverse Eroom's law. Many diseases lack *in vivo* models which are able to recapitulate the human phenotype [42]. Many models have poor translatability to humans: for example Alzheimer's [43] and inflammatory [44] diseases. This is in contrast to animal models for infectious disease and seizures [45].

1.2.3 Quantitative systems pharmacology as a proposed solution

Many individuals within the pharmaceutical world have recognized Eroom's law in one form or another [39, 41, 46-48]. In 2008 and 2010, the NIH held conferences to address the productivity issue plaguing drug discovery [49]. The results from these conferences were summarized in a white paper by Sorger et al., [49], which concluded that although reverse pharmacology has had some success, many diseases are simply too complex to be reduced down a single target. For example, successful psychiatric drugs are known to modulate several targets, whereas highly specific drugs have not been successful [49]. Antibiotics would likely not have been discovered using reverse pharmacology owing to the fact that they target multiple transpeptidases [49].

The proposed solution was to combine a systems-based framework to drug discovery entitled: quantitative systems pharmacology. We have defined it as: "Determining the mechanism(s) of disease progression and mechanism(s) of action of drugs on multi-scale systems through iterative and integrated computational and experimental methods to optimize the development of therapeutic strategies"[50] (**Figure 2**). This seeks to combine what worked well in classical pharmacology (unbiased compound screening in a holistic model) with the advances in biological sciences (notably big data and omics).

We consider the use of biomimetic models to be intrinsic to our QSP approach, because part of the productivity crisis can be attributed to the failure of pre-clinical results to translate to the clinic [42]. Traditional *in vitro* models (both immortalized cell lines, and primary cells) use culture conditions which do not reflect the *in vivo* physiological conditions [51]. Cells are typically grown as static monocultures in a 2D planar arrangement on mechanically stiff glass or plastic unlike the flexible, multiculture conditions *in vivo* [51]. The cell culture media used is typically very unlike blood: most media, among other additives, contains fetal serum with high amounts of glucose under 20% oxygen [51]. This ultimately results in model systems which poorly reflect the disease. Micro-physiology systems in contrast are able to mimic the multicellular 3D architecture of *in vivo* microenvironment [51]. These systems can also incorporate media flow which recapitulates the dynamic conditions *in vivo* through shear stress and oxygen/nutrient gradients [51].

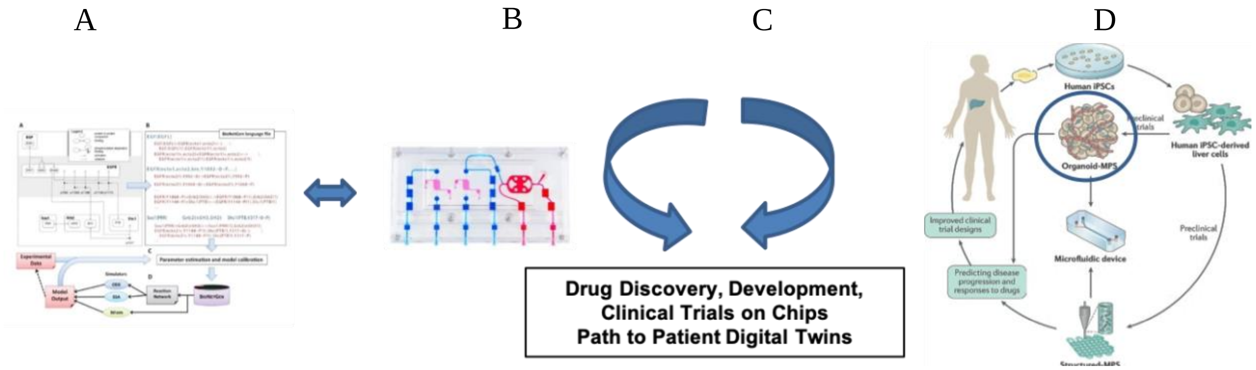

Figure 2. Quantitative systems pharmacology (QSP) overview

QSP: determining the mechanism(s) of disease progression and mechanism(s) of action of drugs on multi-scale systems through iterative and integrated computational (**A**) and experimental methods (**B**) to optimize the development of therapeutic strategies (**C**). A key component of QSP is the utilization of miniaturized functional units of organs, termed human microphysiological systems (MPS) models, which can be used to account for patient heterogeneity and complement animal models (**D**).

1.3 Rationale/motivation for project

1.3.1 Existing drug discovery approaches have not been successful to date

Given the prevalence and potential public health consequences of NAFLD, there is an urgent need to develop treatments for this disease. To do this, it is necessary to understand why drug discovery efforts have failed so that these issues can be addressed. All of the drug trials for NAFLD have been performed using a reverse pharmacology framework, which has ultimately not produced any effective treatments for NAFLD. A paper by Drenth et al identified 10 drugs that were brought to clinical trial, with some making it to phase 3 [35]. These drugs had a variety of different mechanisms which have been successful in pre-clinical models, however, these results did not translate to the clinic, with exception of Resmetirom which successfully met its phase 3 endpoints [34].

Ultimately no mouse model fully recapitulates the disease phenotype [52], as mice (for *in vitro* models see **section 1.2.3)** are in general resistant to developing advanced NAFLD [53]. For example, the severely obese strain ob/ob mice can develop notable steatosis, however, they are largely protected from developing liver related pathologies [53]. Liver fibrosis and inflammation can be induced by restricting dietary methionine and choline, however, these mice typically lose weight and are more sensitive to insulin [52]. Some of these differences can be directly related to the genome and subsequent gene regulation. For example, PNPLA3 (see **section 1.1.4**) is expressed mostly in adipose tissue in mice, unlike humans where it is mostly expressed in the liver [53]. These interspecies differences may mean that the targets discovered using models may be different than those which drive progression in patients. Lack of knowledge linking targets to the disease was identified as one of the reasons for drug failures [46].

1.3.2 Our approach using QSP coupled with MPS

The approach used in this dissertation addresses the inefficiencies identified for traditional drug discovery for NAFLD **(Figure 3)**. Because the mechanisms of disease progression are unknown, we use RNA seq data from patients to define disease states (molecular phenotypes) [54, 55]. We then use a type of surrogate phenotype drug discovery (PDD) by finding drugs which can normalize these disease states [55]. This partially addresses the issue of patient heterogeneity (by taking a data-centric view of NAFLD) and unbiasedly selects for the poly-pharmacology that is required to address the pleiotropy that is intrinsic to the complex pathophysiology of NAFLD [56]. We then test the predicted compounds in a biomimetic model of NAFLD disease progression to maximize the chance of the pre-clinical results translating to patients [57-59].

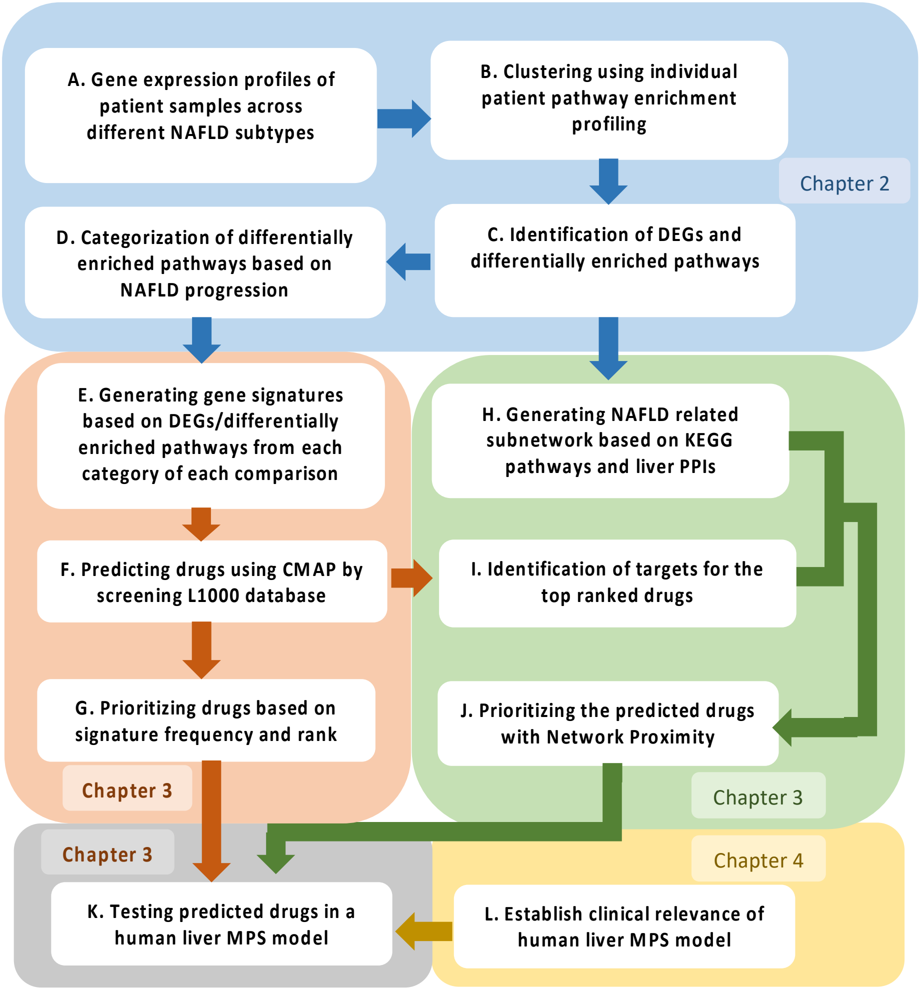

Figure 3. Roadmap of thesis project

The project is organized into 3 integrated chapters, each comprised of a set of steps detailed in the respective chapter's Methods and Results. **Chapter 2** (**A-D**) identifies and clusters individual patient hepatic gene expression and enriched pathway profiles associated with clinical subtypes and categorizes the differentially enriched pathways among these clusters within our current framework of NAFLD pathophysiology (**Figure 5-6**; **Table 2 & S1**, and **Data files S1-S2**). The rationale is presented in the Results for using clusters based on individual patient pathway enrichment profiles as an alternative to the clinical classifications (compare **Figure 6-8**) for determining both differentially expressed genes and enriched pathways between different stages of disease progression. **Chapter 3 (E-G)** generates disease progression-based gene expression signatures (**Table 3; Data file S3**) and, using the Connectivity Map (CMap) databases, identifies drugs that can normalize these signatures (**Tables 4, 6**; and **Data file S4-S5**). The highly integrative steps shown in **(H-J)** maps known protein targets of the predicted drugs from **(E-G)** to a NAFLD subnetwork encompassing protein targets from the gene expression analysis within **Chapter 2** (**Figure S1**; **Table 7**, and **Data file S6**). A network proximity score is then calculated that helps prioritize candidate drugs identified by CMap analysis for experimental testing, based on the proximity of their targets to the NAFLD subnetwork (**Table 8; Data file S7**). In **K**, the effects of the prioritized drugs on a diverse set NAFLD–associated biomarkers in a human MPS, independently shown to recapitulate critical aspects of NAFLD progression **Chapter 4L** (**Figure 10, 13-17**), are determined (**Figure 11-12)**. **Table 1** provides an index of tables, figures and data files associated with each step.

Table 1. Index of associated tables, figures, data files or notebook analyses for each step in Figure 3

			Output		
Chapter	**Step**	**Input data**	**Figures**	**Tables**	**Data files**
2	A. Gene expression profiles of patient samples across different NAFLD subtypes	Ensembl v94 Zerbino et al., 2017 [60] Transcriptome data Gerhard et al., 2018 [61]	**Figure 4**		Analysis notebook Lefever, 2021 [62]
	B. Clustering using individual patient pathway enrichment profiling	KEGG MSigDB v7.0 Liberzon et al., 2011 [63] Step A	**Figure 5**	**Table 2**	Analysis notebook Lefever, 2021 [62]
	C. Identification of DEGs and differentially enriched pathways	Steps A,B	**Figure 6** **Figure 7** **Figure 8** **Figure 9**	**Table S1**	**Data files S1-S2**
	D. Categorization of differentially enriched pathways based on NAFLD progression	Step C	**Figure 6** **Figure 7** **Figure 8** **Figure 9**	**Table S1**	**Data file S1**
3	E. Generating gene signatures based on DEGs/differentially enriched pathways from each category of each comparison	Steps C,D		**Table 3**	**Data file S3**
	F. Predicting drugs using CMAP by screening L1000 database	LINCS L1000 Subramanian et al., 2017 [64] Step E			**Data file S4**
	G. Prioritizing drugs based on signature frequency and rank	Step F		**Table 4** **Table 6**	**Data file S5**
	H. Generating NAFLD related subnetwork based on KEGG pathways and liver PPIs	BioSnap Marinka et al., 2018 [65] Step C	**Figure S1**	**Table 7**	**Data file S6**
	I. Identification of targets for the top ranked drugs	DrugBank v5.4.1 Wishart et al., 2018 [66] Step H			Analysis notebook Lefever, 2021 [62]
	J. Prioritizing the predicted drugs with Network Proximity	Step I		**Table 8**	**Data file S7**
	K. Testing predicted drugs in a human liver MPS model	Steps G, J	**Figure 10** **Figure 11** **Figure 12**	**Table 5**	
4	L. Establish clinical relevance of human liver MPS model	Step A LAMPS transcriptome data	**Figure 13** **Figure 14** **Figure 15** **Figure 16** **Figure 17**		**Data file S8-S10**

2.0 Identification of differentially expressed genes/pathways involved in NAFLD progression

2.1 Introduction

In comparison to other papers, the focus here was on comprehensively identifying disease states of NAFLD progression (as surrogate phenotypic drug discovery) [55]. To do this, I used an RNA-seq dataset [61] of 182 liver wedge biopsies encompassing the full spectrum of NAFLD (36 normal, 46 steatosis, 50 lobular inflammation and 50 fibrosis). Most liver transcriptome datasets are derived from needle biopsies which can be inconsistent [67]. Additionally, most of the microarray [68, 69] and RNA-seq papers [70, 71] tended to have few patients overall, and limited numbers with advanced disease (i.e., fibrosis 3-4). Other datasets [72-74] had limited patient metadata and apparent batch effects which precluded their use in this project.

I first performed an unsupervised clustering analysis of the pathway expression data to identify groupings of patients that could be used for the subsequent analyses. This was done in lieu of directly using the histopathological classifications for the following reasons. First, the histopathological classifications can be susceptible to bias and subjectivity as indicated through poor inter- and modest intra-observer reliability [37]. Second, even if the diagnostic accuracy were not an issue, histological features between paired biopsies from the same patient can be remarkably different [36]. Considering these issues along with the intrinsic heterogeneity of the disease outlined in the introduction, I considered the cluster derived patient groupings to potentially be more biologically meaningful patient groupings than the clinical classifications. This is similar to motivation for clustering in single cell RNAseq [75].

This approach revealed 3 distinct clusters of patients which could be ordered with respect to disease progression, and were used to identify differentially expressed/enriched genes and pathways. We then grouped the pathways into 1 or more of 7 categories based on their literature derived role (or lack thereof) in NAFLD in order to gain systems level insights. This was done because although each of these identified differentially enriched pathways has the potential to be a drug target, their large number and diversity, the prospect of redundancy, and the uncertainty regarding their individual contribution to NAFLD pathogenesis, all present challenges to translating this information into revealing pathophysiological mechanisms and informing therapeutic strategies. The results from this analysis were used in the subsequent chapter.

2.2 Methods

2.2.1 Generation of individual patient liver gene expression profiles

The RNAseq data were derived from samples of wedge biopsies taken from the livers of patients undergoing bariatric surgery as previously described [61]. Patients were diagnosed and samples were labeled according to the predominant liver histology finding as Normal, Steatosis, Lobular inflammation, or Fibrosis [61]. The patient cohort [61] is summarized in **Figure 5** and **Table 2**. The data processing is depicted in the context of the QSP workflow (**Figure 3A**) and the code used for these analyses can be found at: https://github.com/lefeverde/QSPpaper. Paired fastq-files were pseudo-aligned to the human Ensembl [60] v94 transcriptome using the Kallisto pipeline [76]. The resulting transcript abundances were converted into gene-level estimates using Tximport [77] with the settings recommended for VOOM [78, 79]. An exploratory analysis of the gene expression distributions suggested a technical bias exclusive to some of the earliest collected normal and steatotic patient samples that was corrected by the quantile normalization option in the LIMMA-VOOM pipeline [78] (**Figure 4A**). Principal component analysis (PCA) **(Figure 4B)** revealed technical heterogeneity (i.e., batch effect) that was accounted for without an appreciable over-correction using surrogate variable analysis [80, 81] **(Figure 4C).** The patient-gene expression matrix encompassing 182 patients and 18,307 genes per patient can be accessed by following the instructions at https://github.com/lefeverde/QSPpaper and served as the primary input for the analyses described below.

2.2.2 Clustering of individual patient KEGG pathway enrichment profiles associated with NAFLD clinical subtypes

The pathophysiology of NAFLD is intrinsically complex and heterogeneous involving a complex interplay of diverse signaling pathways [7, 14]. As an initial step towards understanding the relationship between individual patient pathway enrichment profiles and clinical subtypes we performed gene set variation analysis (GSVA) [82] (**Figure 3**), in conjunction with MSigDB v7.0 C2 KEGG pathways [63]. GSVA, being an intrinsically unsupervised method, enables individual patient pathway enrichment profiles to be generated across a heterogeneous population providing an advantage over GSEA [83], for example. Importantly and despite the known patient heterogeneity intrinsic to NAFLD, this classification was sufficient to identify and order the three clusters of distinct pathway enrichment profiles with different stages of NAFLD progression and serve as the basis for our subsequent studies. The aforementioned gene expression matrix provided the input for GSVA, resulting in a patient (column) by pathway enrichment (i.e., row of features) matrix. To enable relative comparisons across all identified features minimizing bias in the ensuing cluster analysis while preserving the presence of outliers within each feature, feature standardization (the mean for each value was subtracted then divided by the standard deviation across each KEGG pathway row) was performed [84]. The pathway enrichment matrix was then subjected to hierarchical clustering (Pearson correlation distance, Ward's linkage; for details see https://github.com/lefeverde/QSPpaper), and new groups were identified by cutting the column dendrogram at the 3rd level to create three clusters (**Figure 3B**; **Figure 5**). We chose the 3rd level because these clusters had a statistically significantly association (Pearson's Chi-squared Test) with NAFLD clinical subtype ($p < 2.2e-16$) and type 2 diabetes (T2D) status ($p = 0.01$). These clusters (**Table 2**) were named according to the predominant patient sub-classification in each cluster: the first encompassed almost entirely normal & steatosis (PN&S) patients, the second predominantly lobular inflammation (PLI) patients, and the third predominantly fibrosis (PF) patients. Cluster stability was evaluated using the bootstrapping method described in Hennig, 2007 [85]. The 3 identified clusters were compared to new clusters generated from re-sampling using Jaccard coefficients, a metric of similarity between 2 sets [85]. The coefficients are 0.95, 0.62, and 0.72 for PN&S, PLI, and PF, respectively and are above the minimum cutoff of 0.6 proposed by Hennig, 2007 [85].

2.2.3 Identification of differential gene expression signatures for the three pairwise comparisons within the pathway enrichment clusters and within the clinical classifications

Having shown an association between the pathway enrichment profiles resulting from unsupervised cluster analysis and the clinical phenotypes (**Figure 3B**), we next derived two sets of differential gene expression signatures associated with the processes involved in NAFLD development (**Figure 3C**). One set derived from the cluster analysis and the other from the clinical classifications. For the former, differentially expressed genes (DEGs) were identified from the aforementioned gene expression data applying the standard LIMMA-VOOM pipeline [78, 79] (**Figure 3C**) for three pairwise comparisons (PLI *vs*. PN&S, PF *vs*. PN&S, and PF *vs*. PLI) (**Data file S2**). Differentially enriched pathways were identified analogously except that the GSVA outputs were used (**Figure 6**; **Table S1**, and **Data file S1**). In total, 59, 125, 50 differentially enriched pathways (false discovery rate FDR p-value < .001) were identified for the 3 pairwise comparisons (**Figure 6**; **Table S1**, and **Data file S1**). A PubMed-directed literature search was performed to assign the differentially enriched pathways into one or more of seven categories (C) (**Figure 3D**). The first four categories, insulin resistance and oxidative stress (C1); cell stress, apoptosis and lipotoxicity (C2); inflammation (C3); and fibrosis (C4); comprise disease processes strongly associated with NAFLD and constitute our current conceptual framework of NAFLD progression [7]. The three additional categories include: general KEGG-annotated disease associated pathways (C5); pathways with limited literature association with NAFLD (C6); and pathways with no known association with NAFLD (C7) (**Figure 3D**).

2.3 Results

2.3.1 Data QC and exploratory analyses

Initial exploratory analysis suggested a technical artifact in the data which skewed the count distributions in a non-random manner (**Figure 4A**). This was corrected by applying quantile normalization which forces the distributions of the samples to be the same. Further exploratory analysis using PCA suggested the presence of further artifacts (**Figure 4B**) which were accounted for using surrogate variable analysis (SVA) (**Figure 4C)**.

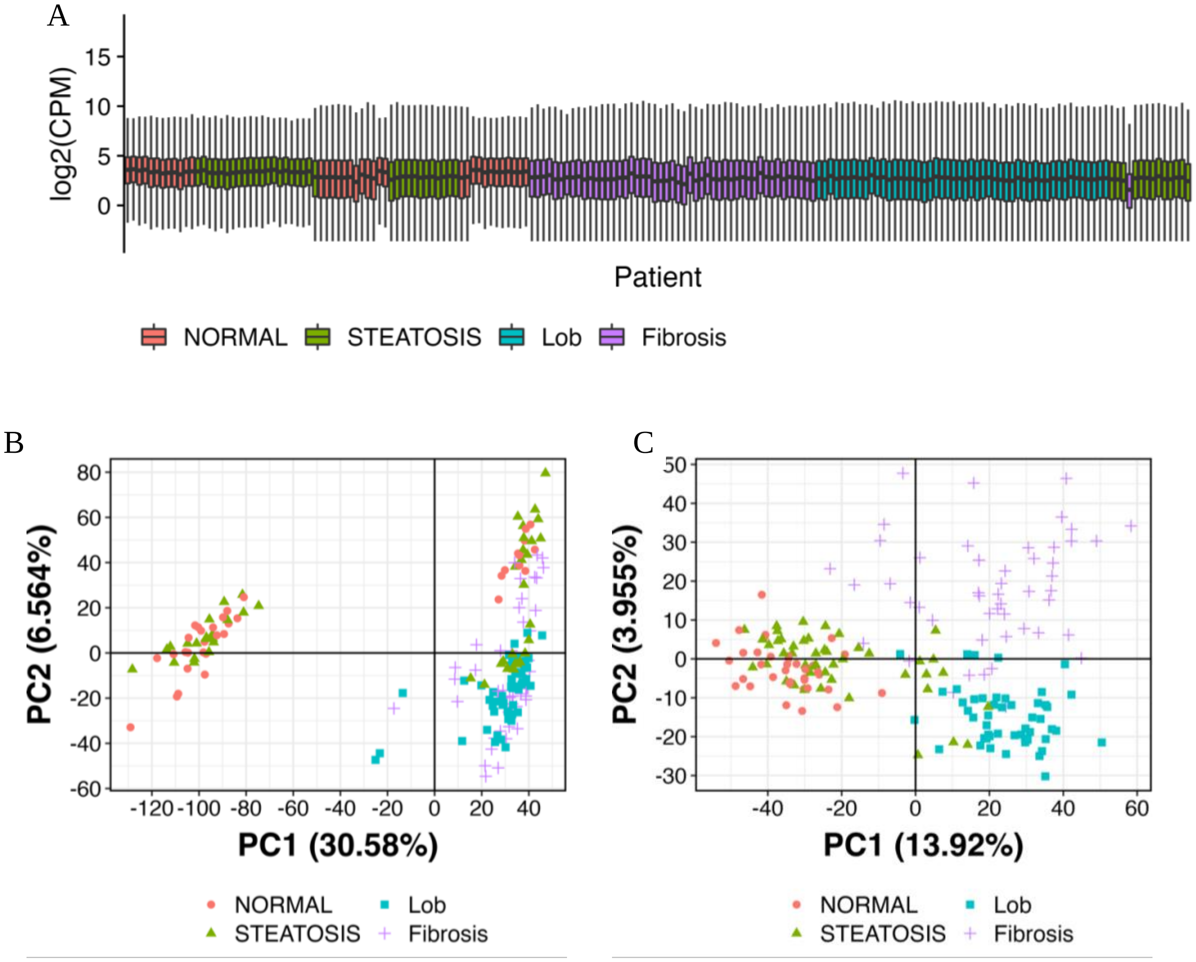

Figure 4. Exploratory data analysis and PCA of the patient transcriptome

A) Shows the boxplots (outliers are not shown) of the log2 transformed counts per million log2(CPM) gene expression values for each patient, ordered by the patient ID (i.e., the order the samples were processed). The distributions of normal and steatosis patients tend to vary in discrete blocks of samples in contrast to lobular inflammation, fibrosis, or a set of steatosis patients collected later on in the experiment. This suggests the presence of a technical artifact which affects the distribution that is confounded with the patient classifications. Hence, we used quantile normalization to correct for this effect. Principal component analysis (PCA) of the log2(CPM) gene expression values revealed the presence of a batch effect (**B**). We therefore used surrogate variable analysis (SVA) to estimate covariates that could account for this unwanted heterogeneity while still retaining the biological variation. **C**) Shows the PCA plot using the SVA corrected gene expression matrix.

2.3.2 Cluster analysis using KEGG enrichment profiles

To help distill NAFLD complexity at the molecular level and associate hepatic signaling network dysregulation with clinical subtypes, we performed an unsupervised gene set variation analysis (GSVA) derived from 182 individual patient liver biopsies representing different stages of NAFLD [61], that included 36 normal, 46 steatosis, 50 lobular inflammation and 50 fibrosis (**Figure 3A-B**). The resulting KEGG pathway enrichment profiles were then subjected to hierarchical clustering with the dendrogram cut at the third level to create three distinct clusters (see **Methods**) that were each enriched in different stages of the disease (**Figures 3B, 5; Table 2; Methods**). The first cluster is composed of 44% normal patients and 48% patients with simple steatosis (NAFL), termed Predominantly Normal & Steatosis (PN&S), highlighting the challenge of distinguishing these two cohorts by gene expression analysis alone when inflammation is not discernable; the second cluster is predominated by patients with lobular inflammation (70%) with little or no fibrosis, termed Predominantly Lobular Inflammation (PLI); and the third is predominantly comprised of patients with advanced disease having fibrosis (61%), termed Predominantly Fibrosis (PF) (**Figure 5**; **Table 2**).

The sample clustering is significantly associated (Pearson's Chi-squared Test) with NAFLD subclass ($p < 2.2e-16$) and T2D status ($p = 0.01$). **Figure 5** also shows that the distributions of sex, body mass index (BMI), and age are similar across the different clusters. In contrast, the occurrence of T2D in cluster PF (55%) is higher than in clusters PN&S (32%) and PLI (32%), corroborating that among individuals with T2D and NAFLD, the prevalence of NASH and advanced fibrosis is enriched when compared to nondiabetics with NAFLD, as observed in independent analyses of this particular cohort [61] and other cohorts [86-88].This is most evident among the 40 patients diagnosed with fibrosis within the PF cluster, with 78% having T2D (**Table 2**).

We next investigated in more detail the association between distinct pathway enrichment profiles (i.e., molecular disease phenotypes) and clinical subtypes by determining the differential pathway enrichment profiles of the pairwise comparisons among the 3 clusters and among the corresponding clinical subtypes (**Figure 3C**).

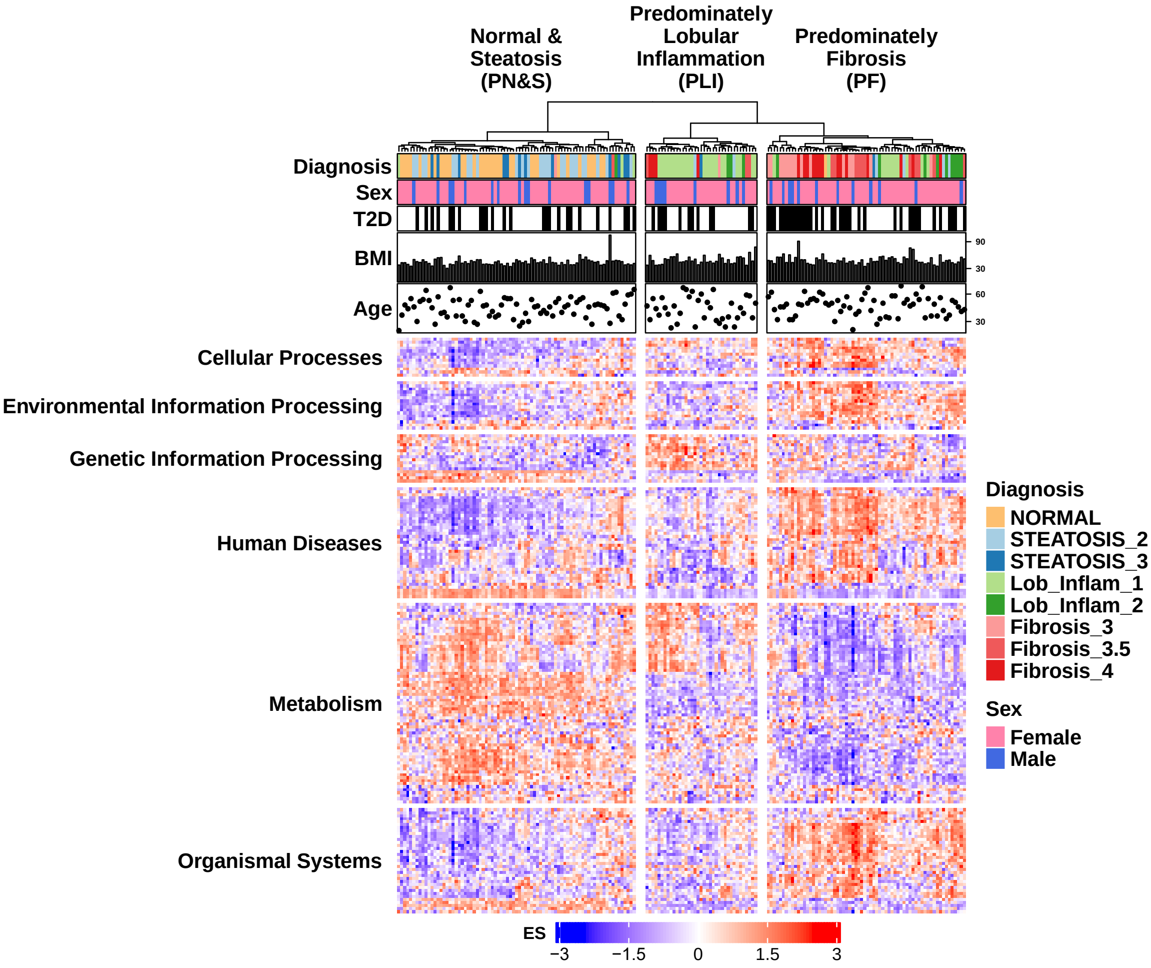

Figure 5. Individual patient liver transcriptome analysis yields distinct clusters based on their KEGG pathway enrichment profiles

The heatmap shows the hierarchical clustering of the liver KEGG pathway enrichment profiles (columns) from individual patients, determined by RNA sequencing and gene set variation analysis (GSVA) using MSigDB v7.0 C2 KEGG pathways [63] (see **2.2 Methods**). Pathways (rows) are grouped according to the top-level KEGG hierarchical classifications (labeled along the left ordinate) to which they belong. The color represents the enrichment score (ES; see the color-coded bar under the heatmap), which reflects the degree to which a pathway is over- or under-represented within that individual patient sample (see [82]). The plots above the heatmap show the patient metadata: the top two bars indicate the color-coded diagnosis (see panel on the right) and patient sex, the third indicates if the patient has been diagnosed with type 2 diabetes (T2D) (black bars), and the additional two plots show the body mass index (BMI) and age of the patient. The clinical subtype distribution for each of the three clusters (PN&S, PLI, PF) is shown in **Table 2**. More details on this analysis can be found in the associated R notebooks [62].

Table 2. Distribution of NAFLD patient subtypes within the three clusters defined in Figure 5.

The numbers of patients diagnosed with type 2 diabetes (T2D) are indicated in parentheses in each case. The clusters of the cohort samples are significantly associated (Pearson's Chi-squared test) with NAFLD subtype ($p < 2.2e-16$) and T2D status ($p = 0.01$). The red values denote the predominant clinical subtype within each cluster

Clinical diagnosis	Normal	Steatosis (Grade)		Lobular Inflammation (Score)		Fibrosis (Score)			Patients per cluster
Cluster		**2**	**3**	**1**	**2**	**3**	**3.5**	**4**	
PN&S	35 (9)	26 (8)	12 (7)	3 (1)	1 (0)	1 (0)	1 (0)	0 (0)	79 (25)
PLI	0 (0)	2 (0)	1 (0)	23 (9)	3 (0)	1 (0)	3 (1)	4 (2)	37 (12)
PF	1 (0)	4 (1)	1 (0)	11 (2)	9 (2)	15 (12)	11 (9)	14 (10)	66 (36)
total	36 (9)	32 (9)	14 (7)	37 (12)	13 (2)	17 (12)	15 (10)	18 (12)	182 (73)

2.3.3 Differentially expressed/enriched genes and pathway results

The pairwise cluster comparisons of PLI vs. PN&S, PF vs. PN&S and PF vs. PLI gene and pathway expression data yielded a total of 139 unique differentially enriched pathways (FDR p-value < 0.001) (**Figure 3C**; **Table S1; Data file S1**). Analogously, clinical subtype comparisons of Lobular inflammation vs Normal & Steatosis (Lob vs. N&S), Fibrosis vs Normal & Steatosis (Fib vs. N&S), and Fibrosis vs Lobular inflammation (Fib vs. Lob) gene and pathway expression data yielded a total of 140 unique differentially enriched pathways (FDR p-value < 0.001) (**Table S1; Data file S1**). The distributions of these differentially enriched pathways within their respective top-level KEGG hierarchical classifications in each pairwise comparison are presented in **Figure 6A** and **Figure 7A**, respectively**.** Overall, these distributions are consistent with the intrinsic heterogeneity of NAFLD that reflects the diverse but convergent impacts of the environment, metabolism, comorbidities, and genetic risk factors [14].

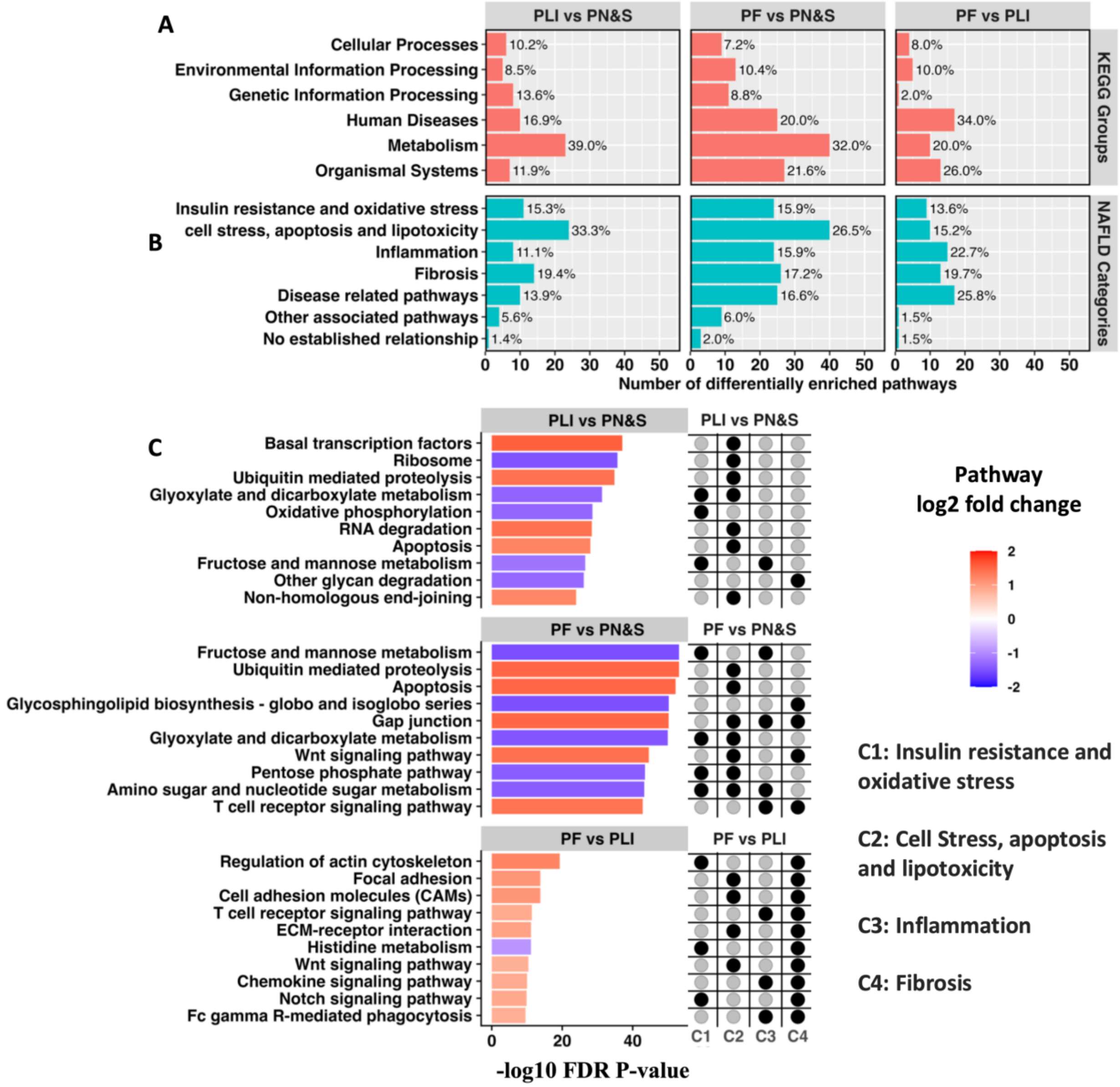

Figure 6. Distribution of differentially enriched pathways and their respective KEGG groups and NAFLD categories among the pairwise cluster comparisons defined in Figure 5.

The number of differentially enriched pathways identified between the PLI vs PN&S, PF vs PN&S, and PF vs. PLI pairwise comparisons were 59, 125, and 50, respectively (adj. p-value <0.001). Their distribution (and percent contribution) with respect to KEGG Groups (**A**) and NAFLD categories (**B**) are detailed in **Table S1** and **Data file S1**. The top ten differentially enriched pathways for each comparison (ranked by the FDR adjusted p values through the linear modelling equivalent of a two sample, moderated t-test) are shown along with their association (black circles) with NAFLD categories C1-4 (as indicated and defined in the Main Text) (**C**). The colors of the bars represent the directionality and relative enrichment of each pathway for each of the pairwise comparisons.

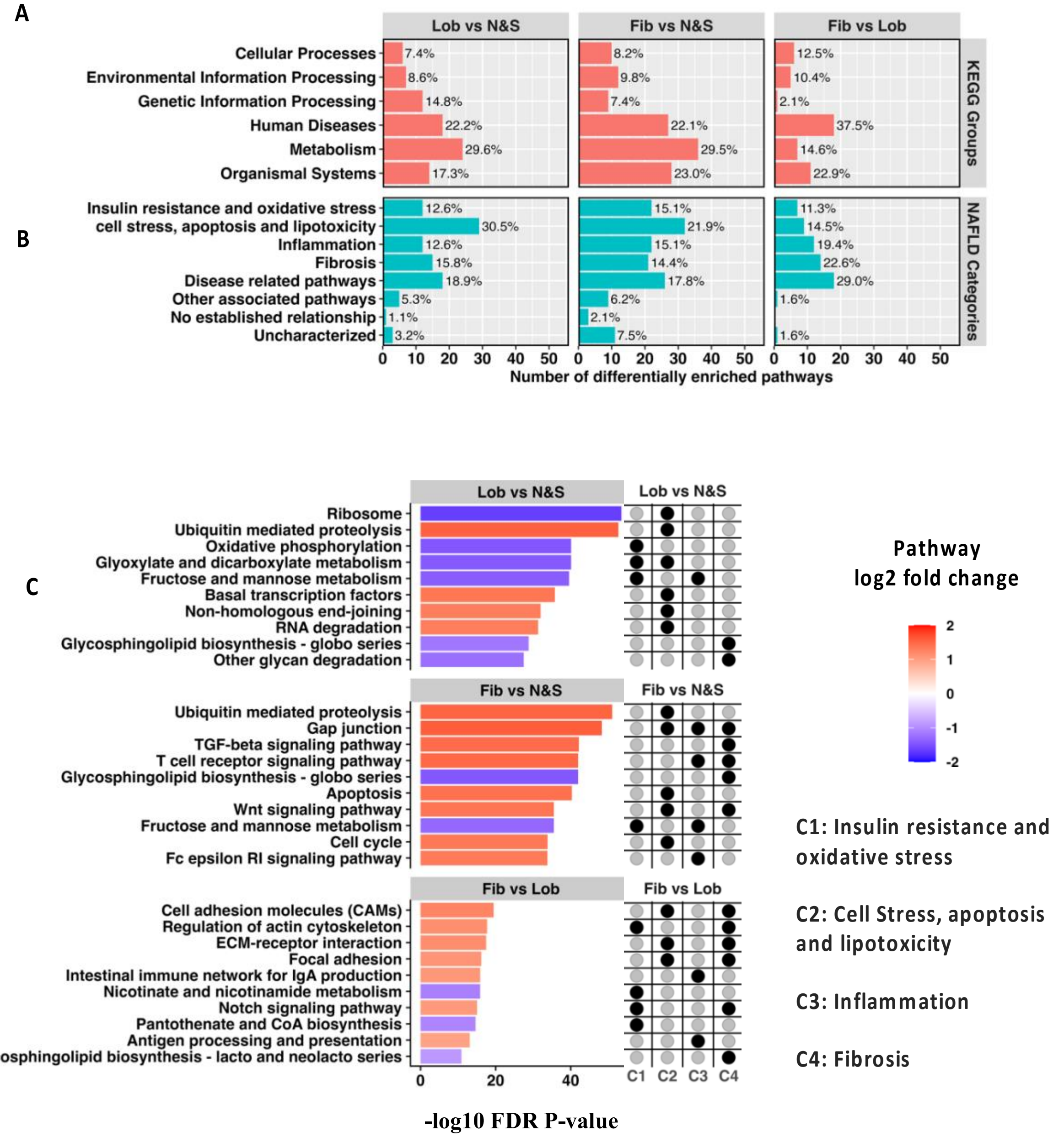

Figure 7. Distribution of differentially enriched pathways and their respective KEGG groups and NAFLD categories of pairwise comparisons performed using the patient clinical classifications (complements Figure 6). The number of differentially enriched pathways identified between the Lobular inflammation vs Normal & Steatosis (Lob vs N&S), Fibrosis vs Normal & Steatosis (Fib vs N&S), and Fibrosis vs Lobular inflammation (Fib vs Lob), pairwise comparisons were 81, 122, and 48, respectively (adj. p-value <0.001). Their distribution (and percent contribution) with respect to KEGG Groups (**A**) and NAFLD categories (**B**) are detailed in **Table S1** and **Data file S1**. The top ten differentially enriched pathways for each comparison (ranked by the FDR adjusted p values through

the linear modelling equivalent of a two sample, moderated t-test) are shown along with their association (black circles) with NAFLD categories C1-4 (as indicated and defined in section 2.2.3) (**C**). The colors of the bars represent the directionality and relative enrichment of each pathway for each of the pairwise comparisons

2.3.4 Categorization of pathways according to their role in NAFLD

The differentially enriched pathways were associated with at least one of four categories that comprise our current conceptual framework of NAFLD progression **(Figure 3D, Methods**): C1) Insulin resistance and oxidative stress, C2) Cell stress, apoptosis, and lipotoxicity, C3) Inflammation, and C4) Fibrosis (**Figures 6B, 7B**)[7, 14]. Apart from these four main categories, other pathways have been observed that are less directly associated with NAFLD or the metabolic syndrome (**Figures 3D, 6B,** 7**B**).

The 10 most differentially enriched pathways for all patient subgroup pairwise comparisons, and their association with the disease processes within these four categories (C1-C4) are shown in **Figure 6C** and **Figure 7C**. The 10 pathways for the PF vs. PN&S and the PLI vs. PN&S cluster-based comparisons, and the Fib vs. N&S and the Lob vs. N&S clinical subtype comparisons, are consistent with the metabolic underpinning, and the resultant cellular stress and inflammatory response intrinsic to NAFLD pathogenesis. Complementarily, the differentially enriched pathways within the comparisons between PF vs PLI and between Fib vs. Lob are consistent with fibrosis being the widely recognized hallmark of disease progression in NASH (**Figures 6C, 7C**).

The majority of the top 10 differentially enriched pathways in these comparisons have been shown to have a role in hepatic fibrosis [89-96] with several involved in hepatic stellate cell activation [89-91]. The majority of differentially enriched pathways derived from the unsupervised clusters are concordant with those derived from the clinical subtypes per se (**Figure 8**), corroborating an association of these pathways with NAFLD progression. The fraction of the top 10 differentially enriched pathways playing a role in multiple disease categories in the PF vs PLI comparison was greater than the fractions in the other two comparisons, indicative of enhanced disease complexity during progression (**Figure 6C)**. Details of the full list of differentially enriched pathways for each comparison can be found in **Table S1** and **Data file S1.** Together, the analysis of this transcriptomic data set appears to have corroborated the clinical relevance of these differentially enriched pathways in the context of the current conceptual framework of NAFLD progression [7, 14].

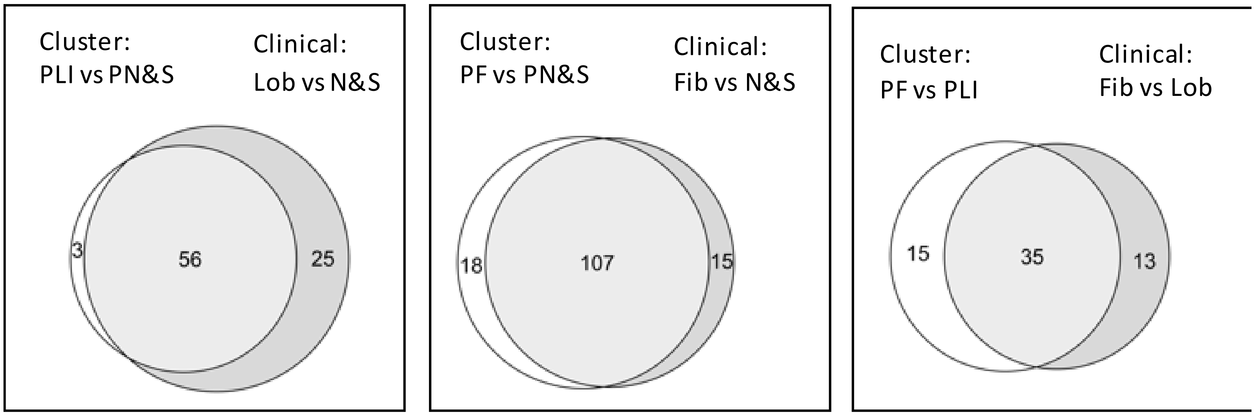

Figure 8. Venn diagrams showing the overlap of differentially enriched pathways (FDR p-value < .001) identified in the cluster (left circle) and clinical label (right circle) pairwise comparisons (Supports Figure 6-7).

Differentially enriched pathways (**Table S1** & **Data file S1**) were identified using the GSVA-limma-voom approach described in the Methods. All of the overlapping pathways were concordant.

2.3.5 External validation of pathway results using microarray datasets

A meta-analysis extending the unsupervised cluster comparisons to three independent NAFLD patient cohorts further supports an association of many of these differentially enriched pathways with NAFLD progression (**Figure 9**).

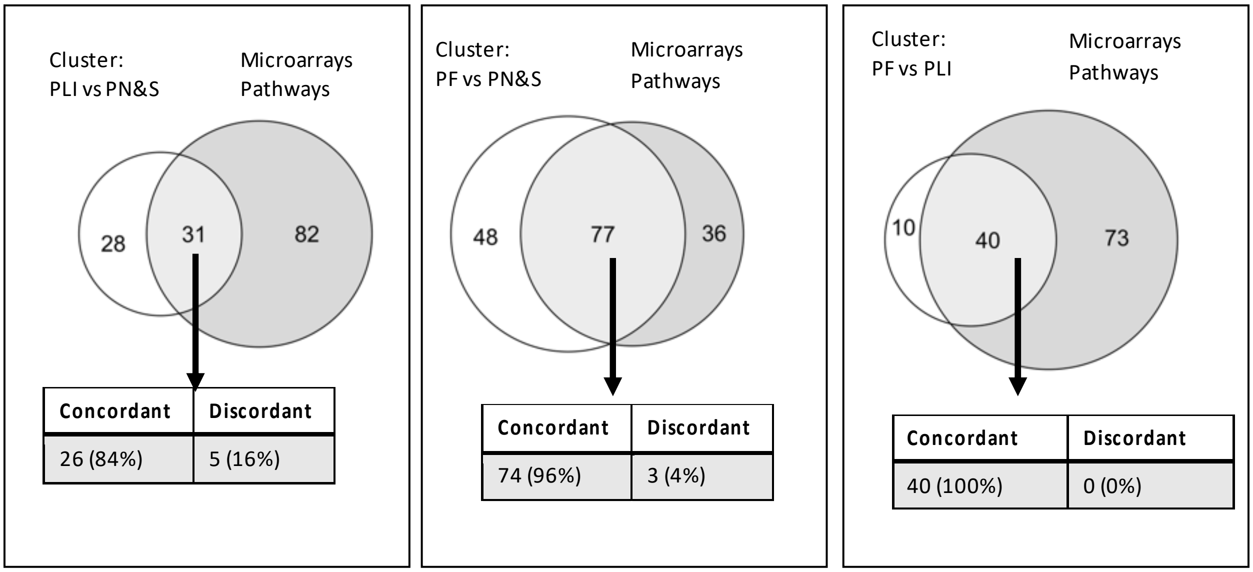

Figure 9. Concordance analysis of the differentially enriched pathways in the cluster pairwise comparisons (left circle) and pathway list derived from microarray datasets (right circle).

The microarray pathway list is the combined differentially enriched pathways found from re-analyzing the following datasets (the specific pairwise comparisons are indicated in the parenthesis): Ahrens et al., [68] (NASH vs healthy obese), Arendt et al., [69] (NASH vs simple steatosis), Murphy et al., [97] (Advanced vs mild fibrosis). See Methods and https://github.com/lefeverde/QSPpaper for details. Differentially enriched (FDR p-value < 0.05) pathways in the 182 patient cohort were considered concordant if they were also differentially enriched in the same direction (i.e., up-regulated or down-regulated) in one or more of the microarray cohorts. Conversely, discordance indicates that a pathway is still differentially enriched but in opposite directions. **p-value <= .004 (Exact Binomial Test, % is estimated effect size)

2.4 Discussion

An important outcome of the initial analysis in this study was the identification of differential pathway enrichment profiles among clinically defined stages of NAFLD progression. This information enabled disease states to be defined that could be targeted by systems-based approaches that are more comprehensive and less biased than traditional targeted approaches and therefore, may be better suited to address the heterogeneity and complex pathophysiology intrinsic to NAFLD. An unsupervised analysis of RNA-seq data from individual liver biopsies derived from a 182 NAFLD patient cohort encompassing a full spectrum of disease progression subtypes from simple steatosis to cirrhosis showed the presence of three patient clusters distinguishable by their pathway enrichment profiles and their predominant association with one of three clinical subtypes: normal/simple steatosis, lobular inflammation, or fibrosis.

Pairwise comparisons among these clusters identified differentially enriched pathways consistent with the metabolic underpinning of NAFLD and the pathophysiological processes implicated in its progression that included lipotoxicity, insulin resistance, oxidative and cellular stress, apoptosis, inflammation, and fibrosis. The differentially enriched pathways identified among the pairwise comparisons of clusters originally derived from the unsupervised analysis showed significant congruence with those derived from the clinical subtypes within this patient cohort and through a meta-analysis, additional patient cohorts.

Although from a traditional translational perspective each of these identified differentially enriched pathways has the potential to be a drug target, their large number and diversity, the prospect of redundancy, and the uncertainty regarding their individual contribution to NAFLD pathogenesis especially across a heterogeneous patient population, all present challenges to translating this information into therapeutic strategies. The recent failures of several NASH clinical trials due to lack of efficacy [98] are likely the result of this complex pathophysiology emphasizing the need to define and probe therapeutic targets more holistically from the perspective of disease states.

3.0 Predict drugs that could halt and/or reverse NAFLD progression using connectivity mapping and drug-target databases

3.1 Introduction

Connectivity Mapping (CMap) is an approach to drug discovery that uses large databases (e.g., LINCS [64]) of cellular responses to perturbations to identify compounds which can normalize a disease state. These perturbations and responses consist of a variety of different types, however, for the purposes here, we are focused on gene expression changes in response to small molecules. The benefit of CMap is that precise targets of neither the compounds nor the disease need to be known beforehand. The basic idea is if a disease state can be represented as a set of up- and a set of down-regulated genes, finding a compound which produces the inverse gene expression pattern would ameliorate the disease. This is analogous to phenotypic drug discovery (and has been dubbed surrogate phenotype drug discovery), in which a drug that reverts the disease phenotype in a model would do so in patients [55]. CMap has been used for a number of disease indications [99], and there is some evidence of this general concept working in liver disease. Growth hormone-releasing hormone (GHRH) has been shown to reduce steatosis and prevent fibrosis progression in HIV-induced NAFLD [100, 101]. Treatment with GHRH normalized pathway expression profiles, notably upregulating oxidative phosphorylation and down-regulating inflammatory and fibrotic pathways [101].

In order for the CMap results to be meaningful it is critical that the gene signatures representing the disease states reflect the disease in question. To ensure that the gene signatures were able to best represent the disease states of NAFLD progression, we created DEG signatures that map to differentially enriched pathways involved in the disease processes comprising the four NAFLD categories C1-C4 (see below and **Figure 3E; Table 3; Data file S3; Methods**). These signatures mirror emergent disease-specific networks (i.e., disease states) at different stages of disease progression. We then applied CMap using the LINCS 2017 and 2020 databases to identify compounds which have the potential to normalize the disease state. We performed a separate, complementary prioritization approach using network proximity. We hypothesize that pharmacologically normalizing these gene signatures using the integrative approach outlined in **Figure 3E-J** and below will similarly modify disease progression in a clinically relevant human MPS model of NAFLD (**Figure 3K)**.

As discussed in the introduction, NAFLD has been difficult to recapitulate in traditional animal models. We are therefore using the Human biomimetic Liver Acinus Microphysiology system (LAMPS) models of NAFLD. We have recently demonstrated that this model system recapitulates critical aspects of NAFLD progression including lipid accumulation, stellate cell activation, and the production of pro-inflammatory cytokines and fibrotic markers, using media containing key NAFLD drivers including increased levels of glucose, insulin and free fatty acids [58, 59] (**Figure 10B**; **3.2 Methods**). The LAMPS model has been tested and reproduced by the Texas A&M Tissue Chip Validation Center (Tex-Val), one of the National Center for Advancing Translational Sciences (NCATS) funded Tissue Chip Testing Centers (TCTC) [102].

3.2 Methods

3.2.1 Generation of Gene Signatures

The first four NAFLD pathway categories (C1-C4) were used for the subsequent generation of NAFLD associated gene signatures (See **Chapter 2**). The gene signatures were created by identifying DEGs (FDR *p*-value < .001) that were a component of the [103] differentially enriched pathways (FDR *p*-value < .001) associated with the disease processes in categories C1-C4 **(Figure 3E; Table 3,** and **Data file S3**) for each of the three pairwise comparisons among the three patient clusters (**Figure 5**). Four category-specific gene signatures were generated containing the aggregated up- and down-regulated genes for each of these three pairwise comparisons (12 gene signatures in total; **Figure 3E; Table 3**; and **Data file S3**). An analogous set of gene signatures was derived from the 3 pairwise clinical classification comparisons Lobular inflammation vs Normal & Steatosis (Lob vs. N&S), Fibrosis vs Normal & Steatosis (Fib vs. N&S), and Fibrosis vs Lobular inflammation (Fib vs. Lob) **Figure 3E; Table 3**; **Data file S3,** for details see https://github.com/lefeverde/QSPpaper).

In sum, two sets of 12 differentially expressed gene signatures were generated, one set derived from distinguishable pathway enrichment profiles associated with different clinical subtypes and the other set derived directly from the clinical classifications (**Figure 3E; Table 3** and **Data file S3)**. The differentially expressed genes in each signature reflect pathway dysregulation in NAFLD-associated processes and the signatures themselves are indicative of a particular disease state at different stages of disease development.

Table 3. Gene signature index (created using Data file S3)

The 24 gene signatures (**Data file S3)** are composed of 2 sets of 12 signatures, with one set derived from the cluster groupings and the other from the clinical classifications (*). Each set is a unique combination of their respective 3 pairwise comparisons and 4 NAFLD pathway categories (see **Methods** for details on the methodology, see **Figure 6-8; Table S1;** and **Data file S1** for the distribution and details of these pathways in the pairwise comparisons) .

NAFLD pathway category	**Cluster gene signature ID**	**Cluster comparison**	**Clinical gene signature ID**	**Clinical Comparison**
C1: Insulin resistance and oxidative stress	s1	PLI vs. PN&S	s*1	Lob vs N&S
C2: cell stress, apoptosis and lipotoxicity	s2	PLI vs. PN&S	s*2	Lob vs N&S
C3: Inflammation	s3	PLI vs. PN&S	s*3	Lob vs N&S
C4: Fibrosis	s4	PLI vs. PN&S	s*4	Lob vs N&S
C1: Insulin resistance and oxidative stress	s5	PF vs. PN&S	s*5	Fib vs N&S
C2: cell stress, apoptosis and lipotoxicity	s6	PF vs. PN&S	s*6	Fib vs N&S
C3: Inflammation	s7	PF vs. PN&S	s*7	Fib vs N&S
C4: Fibrosis	s8	PF vs. PN&S	s*8	Fib vs N&S
C1: Insulin resistance and oxidative stress	s9	PF vs. PLI	s*9	Fib vs Lob
C2: cell stress, apoptosis and lipotoxicity	s10	PF vs. PLI	s*10	Fib vs Lob
C3: Inflammation	s11	PF vs. PLI	s*11	Fib vs Lob
C4: Fibrosis	s12	PF vs. PLI	s*12	Fib vs Lob

3.2.2 Drug predictions using the LINCS L1000 database

Connectivity mapping (CMap) (15) (**Figure 3F**) was used to identify drugs and small molecule perturbagens with the potential to normalize the disease state by reverting the aforementioned NAFLD-associated gene signatures (**Figure 3E; Table 3** and **Data file S3)**. A pilot study using the two sets of 12 signatures obtained in the previous step were employed to query the LINCS L1000 level 5 (GSE92742, released in 2017) expression database [64] as the initial CMap resource. This database consists of perturbation instances, defined as compound-induced differential gene expression output from a unique combination of cell type, time-point, compound, and compound concentration [64, 99]. A subset of the LINCS database with compounds that could be mapped to DrugBank [66] (v5.1.4 used in all analyses) annotations was created by matching the compounds by common name, then by SMILES and/or PubChem ID in cases where the common name differed between databases (see https://github.com/lefeverde/QSPpaper). In total, 1103 DrugBank compounds could be matched to 1495 LINCS compound IDs (there were cases of multiple LINCS compound IDs for the same compound in DrugBank). A LINCS-DrugBank database was generated, comprising a set of 41,710 perturbation instances describing the response to 1103 DrugBank compounds for 70 cell types, at 6 & 24 hr time-points, and a range of concentrations.

During the course of our initial studies, an updated and expanded 2020 LINCS database was released (see https://clue.io) that we used to generate a 2020 LINCS-DrugBank database see https://github.com/lefeverde/QSPpaper. This version included the 1103 previously matched compounds and an additional 1033 compounds yielding 334,393 instances comprising 2136 DrugBank compounds (2795 LINCS compounds IDs) across 228 cell types, and a range of time-points and concentrations (https://clue.io).

The connectivity between each of these drug-induced perturbation instances and each of the 24 input gene signatures was measured by a CMap score (CS) [64, 104], composed of two enrichment scores, one for the upregulated genes (ES_{up}) and the other for the downregulated genes (ES_{down}). The CS was calculated as follows: If the sign of ES_{up} and ES_{down} are the same, CS = 0; otherwise, $CS = (ES_{up} - ES_{down})/2$ [64]. We obtained results using both the 2017 and 2020 databases (**Figure 3F; Data file S4**). The former contains 41,710 CSs (one CS for each of the DrugBank perturbation instances), the latter 334,393 CSs (**Data file S4**). We calculated the p-values for the CSs using methods adapted from Chen et al., 2017 [105]. For each gene signature, a distribution of random CSs was generated by calculating the CS between a random perturbation instance and random gene set with the same number of up- and down-regulated genes as the gene signature. This was repeated 50,000 times for each gene signature to calculate a *p*-value for each CS. The *p*-values represent the probability of observing the CS using a random set of genes with the same size as the gene signature. The *p*-values were adjusted for multiple testing using the FDR method [106].

In order to rank compounds for each of the 24 signature queries, creating a representative CS (i.e., summary statistic) for each compound is necessary since multiple CSs exist for each compound in a single query (**Figure 3G**). Two approaches were used. The first approach is similar to that used by Liu, 2015[107] where the most negative CS (predictive of the compound having the largest effect for inverting the disease gene signature) was chosen for ranking compounds. This approach has the advantage of potentially identifying compounds with maximal efficacy in reversing the gene signature. However, relying on a single or small number of perturbation instances and, therefore limiting the connection to relevant biological context, may reduce the robustness for translating the CMap predictions to a particular experimental model or clinical cohort. The second approach uses the maximum quantile statistic as described by Subramanian et al., 2017[64]. The instances are normalized by cell type then 33rd (Q_{lo}) and 67th (Q_{hi}) quantiles of the CSs are computed for each compound, and whichever is larger in magnitude becomes the summary score. If the CSs for a compound are predominantly < 0, then the $|Q_{lo}| > |Q_{hi}|$ and the summary score is Q_{lo}, and vice-versa when the CSs are predominantly > 0 ($|Q_{lo}| < |Q_{hi}|$ and so the summary score is Q_{hi}. The advantage of the maximum quantile approach is that the score is representative of more biological contexts than the single most negative CS approach.

We initially prioritized the CMap results from the 2017 LINCS database [64] by ranking each drug by the most negative CMap score among all instances for that particular drug, then retaining the top 20 drug predictions from each signature query (**Figure 3G**, **Table 4** and **Data file S5**). The predictions were further filtered using a threshold of FDR *p*-value <0.05, and then ranked based on their frequency of appearance across the 12 cluster signatures (**Figure 3G**, **Table 4** and **Data file S5**). The top 25 compounds from this initial approach are shown in **Table 4**. We performed a similar approach in a follow up study using the expanded 2020 LINCS database (accessible at clue.io), except compounds were ranked (in ascending order) using the maximum quantile summary score (described above and in [64]) (**Figure 3G**, **Table 6** and **Data file S5**). The top 25 predictions from the follow up study are shown **Table 6.**

3.2.3 Drug prioritization using network proximity analysis

As a complementary alternative to ranking compounds by frequency of appearance across the signature CMap queries, we adopted the network proximity method as previously described by Guney et al [108]. The method evaluates the distance between the compound's targets and a given disease module, based on the premise that a compound is effective against a disease if its target proteins are within or in the immediate vicinity of the disease module. In essence, this approach provides an independent criterion for selecting from amongst CMap-extracted compounds, to enable further prioritization for experimental testing (**Figure 3H-J**).

For determining network proximity, information on a liver-specific PPI network (referred to as the background network) is required. The liver BioSnap network [65] which contains 3,180 nodes and 48,409 edges was retrieved to this aim. A subnetwork from this background network representing the PPIs specific to NAFLD was generated as follows: we selected the KEGG pathway map of NAFLD which represents a stage-dependent progression of NAFLD (pathway id: hsa04932, [103, 109]) in addition to 10 interrelated pathways [103, 109]: TNF-signaling (hsa04668), insulin signaling (hsa04910), Type II diabetes mellitus (hsa04930), PI3K-Akt signaling (hsa04151), adipocytokine signaling (hsa04920), PPAR signaling (hsa03320), fatty acid biosynthesis (hsa00061), protein processing in the endoplasmic reticulum (hsa04141), oxidative phosphorylation (hsa00190) and apoptosis (hsa04210). We then created an initial subnetwork by taking the intersection of the background network and the genes from these 11 pathways, yielding 390 nodes. We further filtered this initial subnetwork to only include the nodes that were differentially expressed in the three pairwise comparisons (PLI vs. PN&S, PF vs. PN&S and PF vs. PLI), resulting in a subnetwork of 234 nodes and 1,130 edges, termed the NAFLD subnetwork (**Figures 3H, S1; Table 7,** and **Data File S6**).

We performed network proximity analysis (**Figure 3I-J**) on the results from the cluster signatures queried against the 2020 database prioritized by maximum quantile (**Data File S5**). The NAFLD subnetwork was used as the disease module to determine the proximity of the 126 CMap prioritized compounds (**Data File S5**) described above. Among these, 45 are known to target liver-expressed proteins and were subjected to network proximity analysis (**Figure 3J, Data file S7**) and summarized here. For each drug, we extracted the set of targets (T) from DrugBank v5.1.4 [66], and a distance (d) to the NAFLD subnetwork of 234 nodes (S) was calculated using the liver PPI network as the shortest distance between node t (belonging to T) and the closest node s (belonging to S) averaged over all nodes in T,

$$d(S,T) = \frac{1}{\|T\|}\sum_{t \in T} \min_{s \in S} d(s,t)$$

A reference distance distribution was constructed, corresponding to the expected distance between two randomly selected groups of proteins of the same size and degree of distribution as the disease proteins and drug targets in the network. This bootstrapping procedure [32] was repeated 1,000 times and the mean (μ) and standard deviation (δ) of the reference distance distribution in conjunction with the distance (*d*) determined above were used to calculate a *z*-score (*d*-μ)/δ for each drug. The *z*-score provides a relative ranking of the drugs vis-à-vis each drug's potential effects on the NAFLD disease module; a lower *z*-score means a drug's target profile is closer to the disease module. The resulting top-ranking 25 compounds selected to be prioritized in experiments are presented in **Table 8** and the full list of 45 compounds is in **Data file S7**.

3.2.4 Experimental drug testing using the human Liver Acinus Microphysiology System (LAMPS)

LAMPS studies (**Figures 3K, 10-12; Table 6**) were carried out as previously described [57, 58, 110, 111] using a single chamber commercial microfluidic device (HAR-V single channel device, SCC-001; Nortis, Inc.). LAMPS models were composed of four liver cell types: primary cryopreserved human hepatocytes (HU1960; ThermoFisher), primary liver sinusoidal endothelial cells (LSECs; HL160019ECP1; LifeNet Health), and THP-1 (Kupffer cell; ATCC) and LX-2 (stellate cell; EMD Millipore) human cell lines. The percentages of hepatocytes, THP-1, LSEC, and LX-2 cells are consistent with the scaling used in our previously published models [57, 58, 110, 111]. For the drug testing studies described here, LAMPS models were assembled and maintained for 10 days under flow (5 ul/h) in early metabolic syndrome (EMS) media containing 11.5 mM glucose, 10 nM insulin, 100 μM palmitic acid and 200 μM oleic acid [58]. LAMPS were maintained for this period in EMS containing (in triplicate for each condition) either vehicle control (0.1% DMSO) or the following drug treatments: 10 μM obeticholic acid (Selleck Chemicals), 30 μM pioglitazone (Selleck Chemicals), 1.7 μM or 5 μM vorinostat (Selleck Chemicals). For drug combination studies, 30 μM pioglitazone was combined with either 1.7 μM or 5 μM vorinostat for the duration of the experimental time course. A panel of time course and endpoint NAFLD disease-specific metrics were then examined including albumin, blood urea nitrogen, lactate dehydrogenase secretion, lipid accumulation, stellate cell activation, secretion of the pro-fibrogenic markers pro-collagen 1a1 and TIMP-1, and secretion of the cytokines IL-1β, IL-6, IL-8, TNF-α, and MCP-1 [58]. A detailed description for both LAMPS assembly and NAFLD disease progression metrics is provided in the **Supplementary Methods** and the MPS-Db (https://mps.csb.pitt.edu/assays/assaystudyset/27/) [58, 112] .

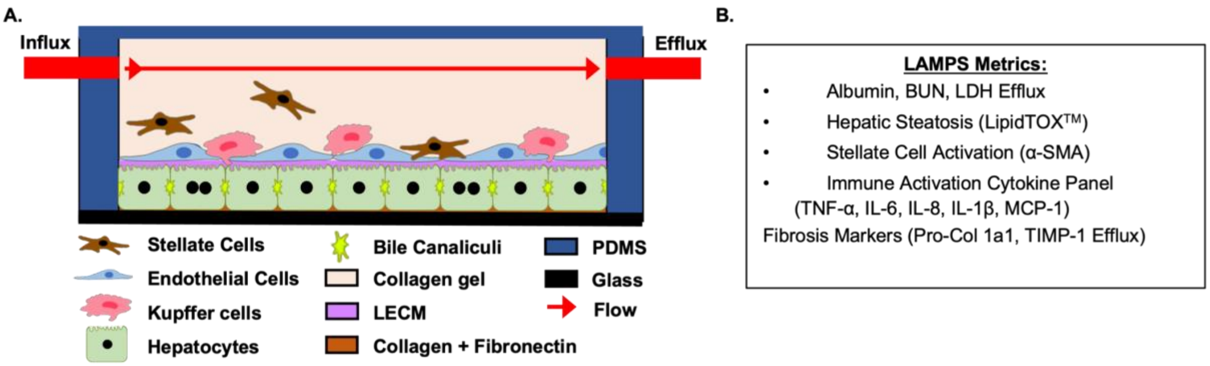

LAMPS Metrics:

- Albumin, BUN, LDH Efflux
- Hepatic Steatosis (LipidTOX™)
- Stellate Cell Activation (α-SMA)
- Immune Activation Cytokine Panel (TNF-α, IL-6, IL-8, IL-1β, MCP-1)

Fibrosis Markers (Pro-Col 1a1, TIMP-1 Efflux)

Figure 10. Using the Biomimetic Human Liver Acinus MicroPhysiology System (LAMPS) for proof-of-concept experimental testing of CMap-predicted drugs.

A) Diagram illustrating the typical cell organization in the LAMPS model after cell seeding. The LAMPS is a polydimethylsiloxane (PDMS)-based all-human, single flow channel, microfluidic cell platform designed to partially recapitulate the structure and functions of the human liver acinus [57, 59, 102, 110, 111]. Primary hepatocytes are first seeded on a layer of collagen and fibronectin. Primary liver sinusoidal endothelial cells (LSEC) and Kupffer-like THP-1 cells are seeded 18-24 h after hepatocytes on a layer of decellularized porcine liver extracellular matrix (LECM). Following this, the LX-2 stellate cell line is seeded last, settling in collagen that fills the chamber. The direction of media flow is indicated by the arrow. A detailed description of the model setup can be found in the Supplementary Materials section. (**B**) We have recently demonstrated that this model system recapitulates key aspects of NAFLD progression using media containing key NAFLD drivers including increased levels of glucose, insulin and free fatty acids [58, 59]. Using this platform, we examined a panel of metrics to monitor NAFLD disease-specific phenotypes, in the presence of CMap-predicted drugs, including model functionality (albumin and blood urea nitrogen (BUN) secretion) and cytotoxicity (lactate dehydrogenase secretion), hepatocellular steatosis (LipidTOXTM labeling), stellate cell activation [α-smooth muscle actin (SMA) antibody staining], and the production of a panel of pro-inflammatory cytokines (TNF-α , IL-6, IL-8, IL-1β and MCP-1) and fibrotic markers (Pro-collagen 1A1 and TIMP-1).

3.3 Results

3.3.1 Initial CMap Prioritization

To predict drugs/small molecules that modulate individual components of NAFLD progression, we initially focused on the DEGs (**Data file S2**) that mapped to the categorized (four NAFLD categories, C1-C4; **Methods**) differentially enriched pathways **(Figures 3D-E; Table S1; Data file S1; 3.2 Methods)** identified above in each of the 3 comparisons of unsupervised clusters (i.e., PLI vs. PN&S, PF vs. PN&S and PF vs. PLI) resulting in a total of 12 gene signatures (**Table 3; Data file S3; 3.2 Methods**). Each of these 12 gene signatures was then used as input to perform connectivity mapping (CMap) on the LINCS database (see Subramanian et al., 2017 [64] and **Methods**). CMap connects the DEG signature between different disease states (including the non-disease state) to drugs and other pharmacologically active compounds predicted to normalize the disease-associated gene signature (see **3.2 Methods**)[64, 99, 104]. In the context of this study, the output of CMap [64, 99, 104] enables the pharmacologic testing of the hypothesis that normalization of the gene signatures between two disease states will halt or perhaps reverse disease progression in an experimental human NAFLD model (see below; **3.2 Methods**).

Since a key objective is to identify drugs that can be repurposed for preventing NAFLD progression, we focused on CMap outputs present in DrugBank (see **3.2 Methods**) that could promote the normalization of the disease-associated gene signature in each NAFLD category (**3.2 Methods; Figure 3F**). For our initial study using the 2017 LINCS database [64], we selected the top 20 drugs (ranked by their most negative CMap score among all instances for that particular drug, see **Methods**) for each of the 12 queries, resulting in 106 unique predicted drugs, 35 of which appeared as an output in more than one query (**Figure 3G; Table 4; Data file S4**). Given the complex interplay among dysregulated metabolic pathways, oxidative and ER stress, inflammation, and fibrosis during NAFLD progression, our initial prioritization of 25 drugs focused on those predicted to modulate multiple gene expression signatures (**Figure 3G; Table 4**). Enriched in this set are drugs with targets known to be associated with NAFLD and with the potential to act pleiotropically, to modulate several pathways. For example, vorinostat is predicted to normalize 5 of the 12 signatures focused primarily on inflammation and fibrosis and previous studies in rodent models of NAFLD suggested efficacy with other HDAC inhibitors [113, 114].

Table 4. 25 highest ranked predicted drugs based on initial CMap analysis

For each gene signature (indexed in **Table 3** & **Data file S3**, as signatures: s1-s12), the 20 highest ranking compounds were selected (FDR p-value < .05) using their respective most negative CMap score among the perturbation instances from the 2017 LINCS database [64] (see Methods). Drugs/small molecules perturbagens identified in more than 1 gene signature-based query were prioritized based both on the number of occurrences across the 12 queries and termed: Gene signature-query frequency (**Data Files S4-S5**) and the number of unique LINCS perturbation instances across the gene signatures. Each signature-based query is ordered (from highest to lowest) according to the relative rank of the drug within each query from which the drug was identified (i.e., occurrence). Each gene signature-based query is associated with a predominate feature (i.e., disease category) of NAFLD. The canonical targets derive from DrugBank (v5.1.4).

Drug name (DrugBank ID)	Gene signature-query frequency	Unique instances	Gene signature indices (see **Table 3**) and their disease categorization	Canonical targets
vorinostat (DB02546)	**5**	**4**	**s11: Inflammation** **s8: Fibrosis** **s6: Cell Stress, Apoptosis and Lipotoxicity** **s3: Inflammation** **s7: Inflammation**	**HDAC1, HDAC2, HDAC3, HDAC6, HDAC8**
SN-38 (DB05482)	**5**	**3**	**s7: Inflammation** **s6: Cell Stress, Apoptosis and Lipotoxicity** **s2: Cell Stress, Apoptosis and Lipotoxicity** **s4: Fibrosis** **s5: Insulin Resistance and Oxidative Stress**	**TOP1**

Drug name (DrugBank ID)	Gene signature-query frequency	Unique instances	Gene signature indices (see **Table 3**) and their disease categorization	Canonical targets
auranofin (DB00995)	**5**	**2**	**s3: Inflammation s5: Insulin Resistance and Oxidative Stress s7: Inflammation s4: Fibrosis s8: Fibrosis**	**PRDX5, IKBKB**
PX-12 (DB05448)	**5**	**2**	**s5: Insulin Resistance and Oxidative Stress s6: Cell Stress, Apoptosis and Lipotoxicity s2: Cell Stress, Apoptosis and Lipotoxicity s3: Inflammation s8: Fibrosis**	**TXNRD1**
methylene-blue (DB08167)	**4**	**3**	**s4: Fibrosis s8: Fibrosis s7: Inflammation s5: Insulin Resistance and Oxidative Stress**	**ACHE**
teniposide (DB00444)	**4**	**2**	**s2: Cell Stress, Apoptosis and Lipotoxicity s6: Cell Stress, Apoptosis and Lipotoxicity s7: Inflammation s4: Fibrosis**	**TOP2A**
trichostatin-a (DB04297)	**3**	**3**	**s3: Inflammation s5: Insulin Resistance and Oxidative Stress s7: Inflammation**	**HDAC8, HDAC7**
camptothecin (DB04690)	**3**	**2**	**s2: Cell Stress, Apoptosis and Lipotoxicity s6: Cell Stress, Apoptosis and Lipotoxicity s7: Inflammation**	**TOP1**
dexamethasone (DB01234)	**3**	**2**	**s1: Insulin Resistance and Oxidative Stress s5: Insulin Resistance and Oxidative Stress s4: Fibrosis**	**NR3C1, NR0B1, ANXA1, NOS2, NR1I2**
geldanamycin (DB02424)	**3**	**2**	**s7: Inflammation s11: Inflammation s4: Fibrosis**	**HSP90AB1, HSP90AA1, HSP90B1**
capsaicin (DB06774)	**3**	**1**	**s6: Cell Stress, Apoptosis and Lipotoxicity s7: Inflammation s3: Inflammation**	**TRPV1, PHB2**
curcumin (DB11672)	**3**	**1**	**s8: Fibrosis s4: Fibrosis s6: Cell Stress, Apoptosis and Lipotoxicity**	**PPARG, VDR, ABCC5, CBR1, GSTP1**
itraconazole (DB01167)	**3**	**1**	**s2: Cell Stress, Apoptosis and Lipotoxicity s1: Insulin Resistance and Oxidative Stress s6: Cell Stress, Apoptosis and Lipotoxicity**	**CYP51A1**
midazolam (DB00683)	**3**	**1**	**s1: Insulin Resistance and Oxidative Stress s6: Cell Stress, Apoptosis and Lipotoxicity s2: Cell Stress, Apoptosis and Lipotoxicity**	**GABRA1, GABRA2, GABRA5, GABRA3, GABRA4, GABRA6**

Drug name (DrugBank ID)	Gene signature-query frequency	Unique instances	Gene signature indices (see **Table 3**) and their disease categorization	Canonical targets
olaparib (DB09074)	**3**	**1**	**s8: Fibrosis** **s4: Fibrosis** **s7: Inflammation**	**PARP1, PARP2, PARP3**
chlorpromazine (DB00477)	**2**	**2**	**s4: Fibrosis** **s3: Inflammation**	**DRD2, DRD1, HTR1A, HTR2A, ADRA1A, ADRA1B, HRH1, KCNH2, DRD3, DRD4, DRD5, HTR2C, ADRA2A, CHRM1, CHRM3, SMPD1, CALM1, ORM1, HTR6, HTR7, HRH4**
fulvestrant (DB00947)	**2**	**2**	**s1: Insulin Resistance and Oxidative Stress** **s4: Fibrosis**	**ESR1**
gemcitabine (DB00441)	**2**	**2**	**s4: Fibrosis** **s7: Inflammation**	**RRM1, TYMS, CMPK1**
alvocidib (DB03496)	**2**	**1**	**s1: Insulin Resistance and Oxidative Stress** **s5: Insulin Resistance and Oxidative Stress**	**CDK2, CDK5, CDK9, CDK1, CDK6, EGFR, CDK4, CDK8, CDK7, PYGM, PYGB, PYGL**
brompheniramine (DB00835)	**2**	**1**	**s1: Insulin Resistance and Oxidative Stress** **s6: Cell Stress, Apoptosis and Lipotoxicity**	**HRH1, CHRM1, CHRM2, CHRM3, CHRM4, CHRM5**
cladribine (DB00242)	**2**	**1**	**s4: Fibrosis** **s3: Inflammation**	**RRM1, RRM2, RRM2B, POLA1, POLE, POLE2, POLE3, POLE4, PNP**
dasatinib (DB01254)	**2**	**1**	**s8: Fibrosis** **s4: Fibrosis**	**ABL1, SRC, EPHA2, LCK, YES1, KIT, PDGFRB, STAT5B, ABL2, FYN, BTK, NR4A3, BCR, CSK, EPHA5, EPHB4, FGR, FRK, HSPA8, LYN, ZAK, MAPK14, PPAT**
dinoprost (DB12789)	**2**	**1**	**s6: Cell Stress, Apoptosis and Lipotoxicity** **s5: Insulin Resistance and Oxidative Stress**	**PTGDR2**
fexaramine (DB02545)	**2**	**1**	**s2: Cell Stress, Apoptosis and Lipotoxicity** **s1: Insulin Resistance and Oxidative Stress**	**NR1H4**
fexofenadine (DB00950)	**2**	**1**	**s5: Insulin Resistance and Oxidative Stress** **s3: Inflammation**	**HRH1**

3.3.2 Proof-of-concept test in LAMPS

We next used our LAMPS model of NAFLD to test the control and predicted drugs. The LAMPS model comprises an all-human cell platform containing primary hepatocytes and liver sinusoidal endothelial cells (LSECs) as well as Kupffer (differentiated THP-1) and stellate (LX-2) cell lines layered in a microfluidic device that recapitulates several key structural features and functions of the human liver acinus [57-59] (**Figures 3K, 10; 3.2 Methods**). We first examined the effects of two control drugs that have shown appreciable clinical benefit in NAFLD clinical trials, obeticholic acid (OCA) [115, 116] and pioglitazone (PGZ) [117] using the LAMPS experimental model (**Figures 3K, 11**). EMS conditions were selected since biomarker and imaging analysis indicate that steatosis, inflammation, and fibrosis are progressively induced during the 10-day testing period [58]. We determined drug concentrations to test in LAMPS guided by the concentrations indicated in the LINCS L1000 database, reported PK/PD and by the absence of cytotoxicity at these concentrations during pre-testing in primary hepatocytes (**Table 5**). In addition, we determined the amount of each compound that was adsorbed by the PDMS component of the LAMPS device (**Table 5**). LAMPS were maintained for 10 days in EMS media containing either the indicated concentration of drug or DMSO vehicle control. We examined a panel of metrics to monitor disease-specific phenotypes including model functionality (albumin and blood urea nitrogen production), cytotoxicity (lactate dehydrogenase secretion), hepatocellular steatosis (LipidTOX® labeling), stellate cell activation (α-smooth muscle actin staining), and the production of a panel of pro-inflammatory cytokines (TNF-α, IL-6, IL-8, IL-1β and MCP-1) and fibrotic markers (Pro-collagen 1A1 and TIMP-1) [58] (**Figure 10**). LAMPS models were maintained for 10 days in EMS media containing 10 µM OCA, 30 µM PGZ, or vehicle control (**Figure 11**). Throughout the experimental time course, albumin, blood urea nitrogen and lactate dehydrogenase showed no significant differences between vehicle control and drug treatment groups (**Figure 11A-C**), suggesting no overt cytotoxicity and loss of function. However, there was a significant decrease in LipidTOX® and α-SMA staining intensity in the OCA and PGZ treatment groups compared to vehicle control demonstrating that both hepatocellular steatosis (**Figure 11D-E**) and stellate cell activation (**Figure 11F-G**) were reduced. Although there was a ~20% decrease in secretion of the pro-fibrotic marker Pro-collagen 1a1 (**Figure 11H**) with treatment of OCA, or PGZ, this decrease was not statistically significant. In addition, there was also no significant change in the secreted levels of TIMP-1, another pro-fibrotic marker, in any of the treatment groups compared to vehicle (**Figure 11I**).

We next examined the effect of the HDAC inhibitor, vorinostat, the highested ranking drug predicted from our initial CMap analysis (**Figures 3K, 11J-S; Table 4**). LAMPS models maintained for 10 days in EMS disease media contained either vorinostat (1.7 µM or 5 µM), or DMSO vehicle control. As shown in **Figure 11**, albumin and blood urea nitrogen curves showed no significant differences between vehicle and drug treatment groups (**Figure 11J-K**), suggesting that these drug treatments do not induce appreciable loss of hepatic functionality. There was a significant decrease in LDH secretion (**Figure 11C**) at days 8 and 10 in the 5 µM vorinostat treatment group, suggesting that treatment with this drug alleviates disease media-induced cytotoxicity. This result is further supported by the overall significant decrease in the day 10 measurements of stellate cell activation (**Figure 11O-P**; α-SMA intensity), production of the pro-fibrotic markers pro-collagen 1a1 and TIMP-1 (**Figure 11Q-R**) and inflammatory cytokine production (**Figure 11S**) observed in the vorinostat treatment group. In contrast to PGZ and OCA, and despite its significant effect on profibrotic markers, vorinostat treatment did not appreciably alleviate lipid accumulation at day 10 (**Figure 11M-N**), indicating no significant effect on steatosis.

Overall, the CMap predicted drug vorinostat in comparison to the control drugs PGZ and OCA, exhibited complementary effects that mitigated NAFLD progression in the LAMPS. To extend our initial proof-of-concept (PoC) findings, we tested LAMPS models maintained in EMS media containing either control or combinations of pioglitazone (30 µM) and vorinostat (1.7 µM or 5 µM) and monitored the same panel of disease-specific metrics. As shown in **Figure 12**, while albumin secretion profiles showed no significant differences between vehicle and drug treatment groups, suggesting that these drug combinations did not result in loss of model functionality **(Figure 12A)**, a significant increase in urea nitrogen secretion was observed in both drug combination groups compared to control, suggesting increased model metabolic activity **(Figure 12B)**. In addition, like the LDH profile in **Figure 11**, there was a significant decrease in LDH secretion **(Figure 12C)** in the 5 µM vorinostat treatment group, suggesting a reduction in disease-induced cytotoxicity. In contrast to the individual drug testing studies shown in **Figure 11**, we found an effect on the full complement of disease progression markers measured in this study when pioglitazone and vorinostat were used in combination, as we observed a significant reduction in both lipid accumulation **(Figure 12D-E)** and stellate cell activation **(Figure 12F-G**), as well as in the production of the pro-fibrotic markers pro-collagen 1a1 and TIMP-1 **(Figure 12H-I)** and inflammatory cytokine production **(Figure 12J).**

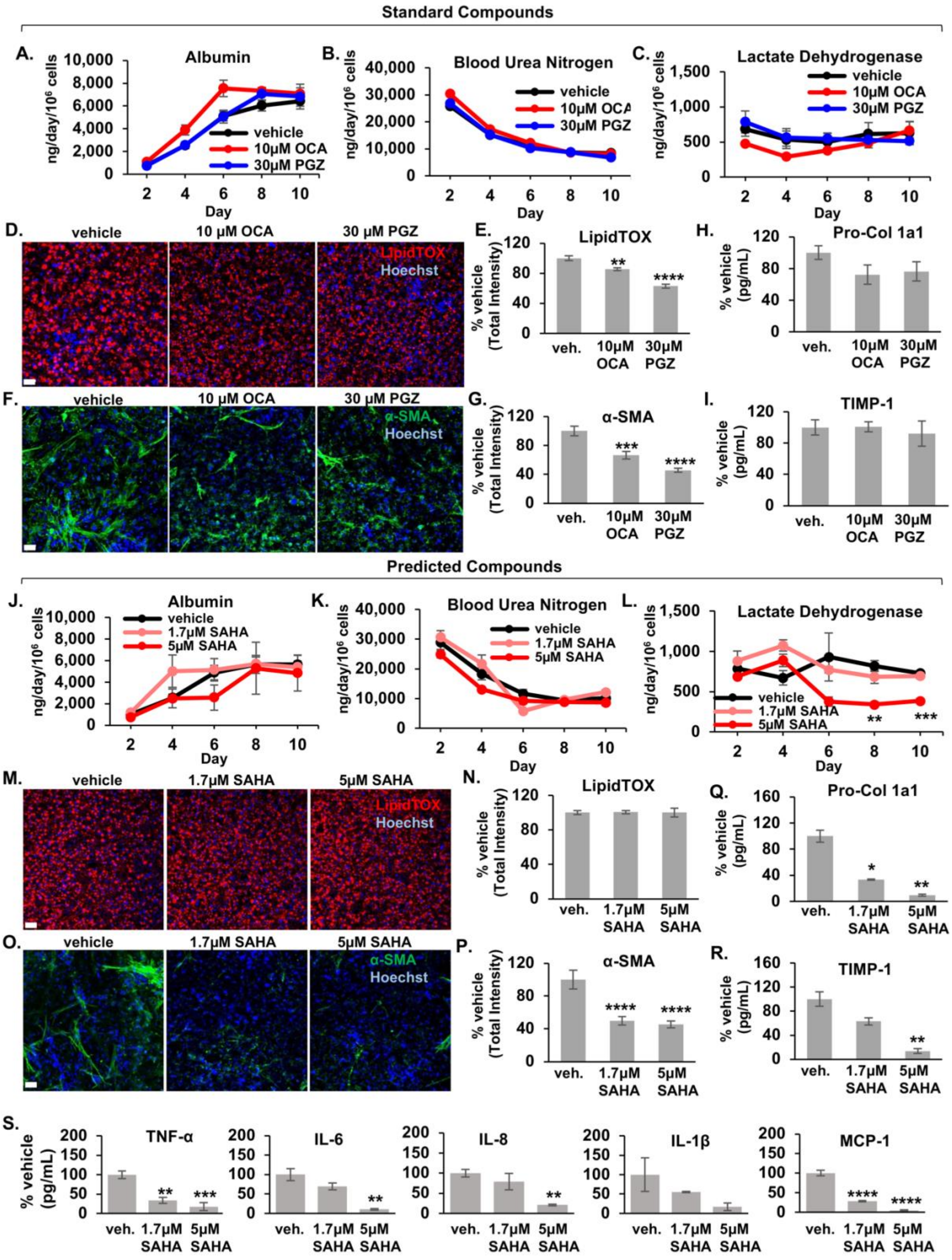
Standard Compounds
A.
Albumin
ng/day/10⁶ cells
10,000
8,000
6,000
4,000
2,000
0
vehicle
10μM OCA
30μM PGZ
2
4
6
8
10
Day
B.
Blood Urea Nitrogen
ng/day/10⁶ cells
40,000
30,000
20,000
10,000
0
vehicle
10μM OCA
30μM PGZ
Day
C.
Lactate Dehydrogenase
ng/day/10⁶ cells
1,500
1,000
500
0
vehicle
10μM OCA
30μM PGZ
Day
D.
vehicle
10 μM OCA
30 μM PGZ
LipidTOX
Hoechst
E.
LipidTOX
% vehicle (Total Intensity)
120
80
40
0
**
****
veh.
10μM OCA
30μM PGZ
H.
Pro-Col 1a1
% vehicle (pg/mL)
F.
vehicle
10 μM OCA
30 μM PGZ
α-SMA
Hoechst
G.
α-SMA
***
****
I.
TIMP-1
Predicted Compounds
J.
Albumin
vehicle
1.7μM SAHA
5μM SAHA
K.
Blood Urea Nitrogen
L.
Lactate Dehydrogenase
**
***
M.
vehicle
1.7μM SAHA
5μM SAHA
LipidTOX
Hoechst
N.
LipidTOX
Q.
Pro-Col 1a1
160
*
**
O.
α-SMA
Hoechst
P.
α-SMA
****
****
R.
TIMP-1
**
S.
% vehicle (pg/mL)
200
150
100
50
0
TNF-α
**
***
IL-6
**
IL-8
**
IL-1β
MCP-1
****
****
veh.
1.7μM SAHA
5μM SAHA

Figure 11. Control and predicted drugs reduce different NAFLD disease phenotypes in LAMPS models treated with EMS media

LAMPS models were maintained for 10 days in Early Metabolic Syndrome (EMS) media containing either vehicle control, 10 µM obeticholic acid (OCA) and 30 µM Pioglitazone (PGZ) [standard compounds], or vorinostat (suberoylanilide hydroxamic acid; SAHA) at 1.7 µM or 5 µM [predicted compounds]. A panel of metrics were examined to monitor disease-specific phenotypes. For standard drugs, albumin, blood urea nitrogen, and lactate dehydrogenase curves throughout the time course show no significant differences between vehicle and drug treatment groups, suggesting no overt model cytotoxicity or loss of function (**A-C**). At day 10, there is a significant decrease in steatosis (**D & E**; LipidTOX^{TM} intensity) and stellate cell activation (**F & G**; α-SMA intensity) for both OCA and PGZ groups compared to vehicle. Panels **D & F** display representative 20X Day 10 LipidTOX^{TM} (**D**) and and α-SMA (**F**) images of LAMPS; Scale bar; 50 µm. There is no significant change in the secreted levels of the pro-fibrotic markers Pro-Col 1a1 (**H**) TIMP-1 (**I**) in either treatment group compared to vehicle. For the predicted drug vorinostat (SAHA), albumin and blood urea nitrogen curves show no significant differences between vehicle and treatment groups (**J & K**), suggesting that these drug treatments do not result in loss of model functionality; however, a significant decrease in LDH secretion (**L**) at days 8 and 10 in the 5 µM vorinostat treatment group, suggesting decreased cytotoxicity. This is further supported by the significant decrease in stellate cell activation (**O & P**; α-SMA intensity), production of the pro-fibrotic markers pro-collagen 1a1 and TIMP-1 (**Q & R**) and inflammatory cytokine production (**S**) observed in the vorinostat group. In contrast, vorinostat does not reduce lipid accumulation compared to vehicle control (**M & N**), indicating no effect on steatosis. Panels **M & O** display representative 20X Day 10 LipidTOX^{TM} (**D**) and α-SMA images of LAMPS under each treatment condition; Scale bar; 50 µm. For each control and drug treatment group, n = 3 chips were analyzed and plotted ± SEM for each assay and statistical significance was assessed using a One-Way ANOVA with Dunnett’s test to make comparisons between each drug treatment group and the vehicle control (* $P< 0.05$; ** $p < 0.01$; *** $p < 0.001$; **** $p < 0.0001$).

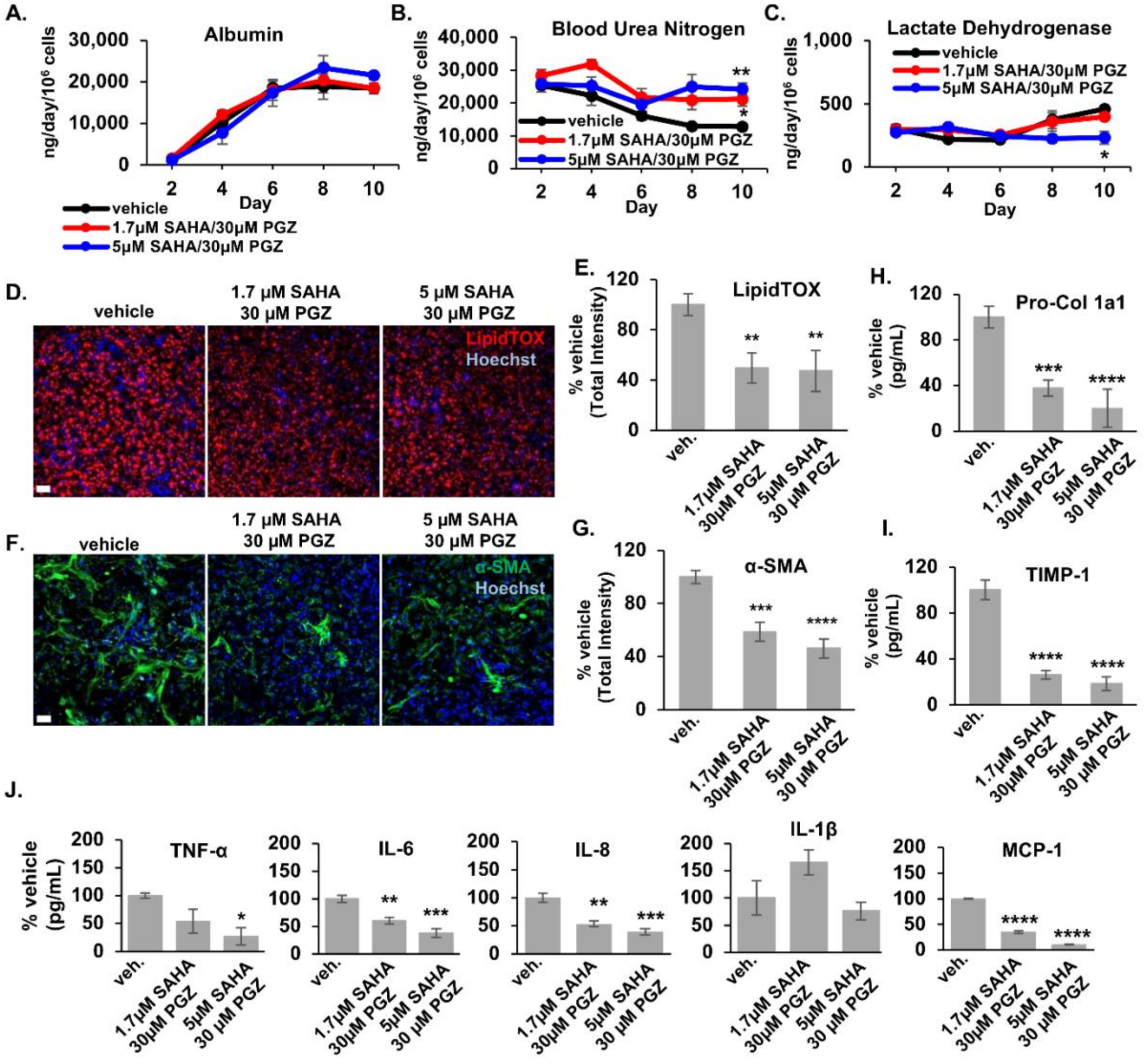

Figure 12. Pioglitazone and vorinostat used in combination results in the reduction of steatosis and stellate cell activation as well as the secretion of pro-fibrotic markers and production of inflammatory cytokines in LAMPS models treated with EMS media

LAMPS models were maintained for 10 days in NAFLD disease media containing combinations of pioglitazone (30 µM) and vorinostat (1.7 µM or 5 µM) or DMSO vehicle control. A panel of metrics were examined to monitor disease-specific phenotypes under these treatment conditions. While albumin secretion profiles show no significant differences between vehicle and drug treatment groups, suggesting that these drug combinations do not result in loss of model functionality (**A**), a significant increase in urea nitrogen secretion is observed in both drug combination groups compared to control, suggesting increased model metabolic activity (**B**). In addition, like the LDH profile in **Figure**

11, there is a significant decrease in LDH secretion (**C**) in the 5 µM vorinostat treatment group, suggesting a reduction in cytotoxicity. Compared to the contrasting effects observed in the individual drug testing studies shown in **Figure 11**, we observe an overall decrease in both lipid accumulation (**D & E**) and stellate cell activation (**F & G**), as well as in the production of the pro-fibrotic markers pro-collagen 1a1 and TIMP-1 (**H & I**) and inflammatory cytokine production (**J**) when pioglitazone and vorinostat are used in combination. Panels **D & F** display representative 20X Day 10 LipidTOX ^{TM} (**D**) and and α-SMA (**F**) images of LAMPS under each treatment condition; Scale bar; 50 μm. For each control and drug treatment group, n = 3 chips were analyzed and plotted ± SEM for each assay and statistical significance was assessed using a One-Way ANOVA with Dunnett's test to make comparisons between each drug treatment group and the vehicle control (* $P< 0.05$; ** $p < 0.01$; *** $p < 0.001$; **** $p < 0.0001$).

Table 5. Drug binding and cytotoxicity profiles for compounds used in LAMPS studies

To assess the drug binding capability of the polydimethylsiloxane (PDMS)-containing LAMPS device for compounds used in these studies, we used perfusion flow tests and mass spectrometry analysis of efflux collected from LAMPS devices at 72 h to determine the overall effective concentration of each compound compared to the starting concentration of drug as previously described [110, 111]. The TC_{50} (Toxic Concentration inducing 50% hepatocyte death) was determined in a 5-day hepatocyte cytotoxicity assay (**Supplementary Methods**). ND- not determined. The TC_{50} assay was not conducted on Obetacholic acid or Pioglitazone. The concentration of these compounds was based on previous experimentation in the LAMPS model.

Compound	**Target**	**LogP value (PubChem)**	**% drug recovery at 72 h**	**TC_{50} (µM)**
Obeticholic Acid (OCA)	FXR	5.1	90%	ND
Pioglitazone (PGZ)	PPARγ	3.9	95%	ND
Vorinostat (SAHA)	HDAC	1.4	86%	29.8

3.3.3 Expansion of CMap results using the updated 2020 LINCS database

During the course of these initial studies the LINCS L1000 database (accessible at https://clue.io) was significantly expanded providing an additional 1033 drugs that were annotated in DrugBank and accordingly, a more comprehensive set of perturbation instances that also encompassed additional cell lines. We took advantage of this larger biological representation by incorporating a percentile statistic for defining an overall CMap score for ranking drugs (**Figure 3F-G**; **3.2 Methods** and [64]). Using this updated database, many drugs were identified ranking higher than vorinostat with the 25 highest shown in **Table 6**. Some of these drugs having canonical targets associated with NAFLD are predicted to revert 7 of the 12 cluster-based signatures. For example, the NSAID fenoprofen inhibits cyclooxygenase 1 and 2 to modulate prostaglandin synthesis and also activates the peroxisome proliferator receptors, alpha and gamma (PPARα/γ). The androgen receptor agonist oxandrolone, also predicted to revert 7 of the 12 signatures, promoted hepatic ketogenesis in an observational trial of adult males [118] consistent with enhanced fatty acid partitioning from intrahepatic triglycerides towards mitochondrial beta oxidation and 4-hydroxybutyrate formation as proposed for the reversal of NAFLD resulting from a short-term ketogenic diet [119, 120]. Although several of the ranked drugs (**Table 6**) were structurally steroid-like, considerable structural diversity was evident in the predicted antibiotic and oncology drug classes. The cephalosporin, cefotaxime, interacts with the family of organic anion transporters (OATs or SLC22) whose expression is significantly altered during NAFLD progression [121]. These transporters mediate the hepatic disposition of drugs, xenobiotic metabolites and endogenous intermediates and metabolites. Targeting NAFLD associated hepatic proteins that have critical roles both in xenobiotic and endobiotic metabolism may be an emerging theme (see Discussion and [122]) that can be extended to nuclear receptor transcription factors as the diverse drugs tetracycline, SN-38, and the endogenous steroid, pregnanolone, have been shown to interact with PXR [123, 124]. In a parallel CMap analysis based on queries derived from 12 patient subtype signatures (complementary to the set of 12 signatures derived from the unsupervised clusters, **Table 3**; **Data files S3-5**), 17/25 of the same predicted drugs (**Table 6**) were also identified and enriched in the highest ranked drugs.

Table 6. The 25 highest ranked CMap-predicted drugs based on frequency of occurrence across multiple NAFLD-associated gene signature queries

Drugs/small molecules perturbagens identified in more than 1 of the 12 cluster-based gene signature queries were prioritized according to the number of occurrences across the 12 queries and termed: Gene signature-query frequency (Data File S4-S5). Each signature-based query is indexed s1-12 (see **Table 3** and **Data file S3**) and ordered (from highest to lowest) according to the relative rank of the drug within each query that the drug was identified (i.e., occurrence). Each gene signature-based query is associated with a predominate feature (i.e., disease category) of NAFLD (see **Table 3**; **Data File S3**, and Methods). The canonical targets derive from DrugBank (v5.1.4) except for (PXR) (explained in Results). Distinct from Table S5 CMap scores were calculated as percentile scores (see Methods, Results, and [64]) and the 2020 expanded LINCS Database was used as indicated in the Methods and Results. *Denotes compounds also found in a parallel top 25 CMap-predicted drug analysis using clinical classification-based signature queries (**Table 3** and **Data File S3**).

Drug name (DrugBank ID)	Gene signature-query frequency	Gene signature indices (see **Table 3**) and their disease categorization	Canonical targets
eltanolone* (DB12308) (pregnanolone)	**7**	**s5: Insulin Resistance and Oxidative Stress** **s6: Cell Stress, Apoptosis and Lipotoxicity** **s7: Inflammation** **s3: Inflammation** **s2: Cell Stress, Apoptosis and Lipotoxicity** **s8: Fibrosis** **s1: Insulin Resistance and Oxidative Stress**	**(PXR)**

Drug name (DrugBank ID)	Gene signature-query frequency	Gene signature indices (see **Table 3**) and their disease categorization	Canonical targets
fenoprofen* (DB00573)	**7**	**s5: Insulin Resistance and Oxidative Stress** **s6: Cell Stress, Apoptosis and Lipotoxicity** **s7: Inflammation** **s8: Fibrosis** **s2: Cell Stress, Apoptosis and Lipotoxicity** **s3: Inflammation** **s4: Fibrosis**	**PTGS2, PTGS1, PPARA, PPARG**
oxandrolone* (DB00621)	**7**	**s2: Cell Stress, Apoptosis and Lipotoxicity** **s6: Cell Stress, Apoptosis and Lipotoxicity** **s3: Inflammation** **s4: Fibrosis** **s8: Fibrosis** **s1: Insulin Resistance and Oxidative Stress** **s5: Insulin Resistance and Oxidative Stress**	**AR**
cefotaxime* (DB00493)	**6**	**s2: Cell Stress, Apoptosis and Lipotoxicity** **s6: Cell Stress, Apoptosis and Lipotoxicity** **s1: Insulin Resistance and Oxidative Stress** **s7: Inflammation** **s3: Inflammation** **s5: Insulin Resistance and Oxidative Stress**	**SLC22A6, SLC22A8, SLC22A11, SLC22A7, SLC15A1, ALB, SLC15A2**
amorolfine* (DB09056)	**5**	**s3: Inflammation** **s7: Inflammation** **s8: Fibrosis** **s5: Insulin Resistance and Oxidative Stress** **s6: Cell Stress, Apoptosis and Lipotoxicity**	
dexamethasone* (DB01234)	**5**	**s3: Inflammation** **s6: Cell Stress, Apoptosis and Lipotoxicity** **s2: Cell Stress, Apoptosis and Lipotoxicity** **s7: Inflammation** **s12: Fibrosis**	**NR3C1, NR0B1, ANXA1, NOS2, NR1I2 (PXR)**
proxyphylline (DB13449)	**5**	**s5: Insulin Resistance and Oxidative Stress** **s10: Cell Stress, Apoptosis and Lipotoxicity** **s11: Inflammation** **s12: Fibrosis** **s9: Insulin Resistance and Oxidative Stress**	
sn-38* (DB05482)	**5**	**s4: Fibrosis** **s2: Cell Stress, Apoptosis and Lipotoxicity** **s5: Insulin Resistance and Oxidative Stress** **s6: Cell Stress, Apoptosis and Lipotoxicity** **s7: Inflammation**	**TOP1, (PXR)**
sulfanitran* (DB11463)	**5**	**s5: Insulin Resistance and Oxidative Stress** **s6: Cell Stress, Apoptosis and Lipotoxicity** **s2: Cell Stress, Apoptosis and Lipotoxicity** **s3: Inflammation** **s1: Insulin Resistance and Oxidative Stress**	

Drug name (DrugBank ID)	Gene signature-query frequency	Gene signature indices (see **Table 3**) and their disease categorization	Canonical targets
tetracycline* (DB00759)	**4**	**s12: Fibrosis** **s6: Cell Stress, Apoptosis and Lipotoxicity** **s8: Fibrosis** **s7: Inflammation**	**PRNP, PADI4, (PXR)**
7-hydroxystaurosporine* (DB01933)	**4**	**s8: Fibrosis** **s6: Cell Stress, Apoptosis and Lipotoxicity** **s2: Cell Stress, Apoptosis and Lipotoxicity** **s4: Fibrosis**	**PDPK1**
dopamine (DB00988)	**4**	**s12: Fibrosis** **s9: Insulin Resistance and Oxidative Stress** **s11: Inflammation** **s10: Cell Stress, Apoptosis and Lipotoxicity**	**DRD2, DRD1, DRD5, DRD3, DRD4, SLC6A3, DBH, HTR1A, HTR7, SLC6A2, SLC6A4, HTR3A, HTR3B, SOD1, SLC18A2**
medrysone* (DB00253)	**4**	**s2: Cell Stress, Apoptosis and Lipotoxicity** **s6: Cell Stress, Apoptosis and Lipotoxicity** **s5: Insulin Resistance and Oxidative Stress** **s1: Insulin Resistance and Oxidative Stress**	**NR3C1**
mestranol* (DB01357)	**4**	**s2: Cell Stress, Apoptosis and Lipotoxicity** **s6: Cell Stress, Apoptosis and Lipotoxicity** **s4: Fibrosis** **s7: Inflammation**	**ESR1**
norethindrone* (DB00717)	**4**	**s10: Cell Stress, Apoptosis and Lipotoxicity** **s12: Fibrosis** **s9: Insulin Resistance and Oxidative Stress** **s8: Fibrosis**	**PGR**
troxerutin* (DB13124)	**4**	**s5: Insulin Resistance and Oxidative Stress** **s8: Fibrosis** **s7: Inflammation** **s6: Cell Stress, Apoptosis and Lipotoxicity**	
brequinar* (DB03523)	**3**	**s7: Inflammation** **s4: Fibrosis** **s3: Inflammation**	**DHODH**
bromocriptine (DB01200)	**3**	**s1: Insulin Resistance and Oxidative Stress** **s11: Inflammation** **s12: Fibrosis**	**DRD2, DRD3, HTR1D, ADRA2A, HTR1A, ADRA2C, ADRA2B, HTR2B, DRD4, HTR2A, HTR1B, HTR2C, DRD5, DRD1, ADRA1A, ADRA1B, ADRA1D, HTR7**
cebranopadol* (DB12830)	**3**	**s4: Fibrosis** **s7: Inflammation** **s8: Fibrosis**	

Drug name (DrugBank ID)	Gene signature-query frequency	Gene signature indices (see **Table 3**) and their disease categorization	Canonical targets
flucloxacillin (DB00301)	**3**	**s9: Insulin Resistance and Oxidative Stress s11: Inflammation s2: Cell Stress, Apoptosis and Lipotoxicity**	
granisetron (DB00889)	**3**	**s11: Inflammation s10: Cell Stress, Apoptosis and Lipotoxicity s12: Fibrosis**	**HTR3A**
hexestrol (DB07931)	**3**	**s9: Insulin Resistance and Oxidative Stress s10: Cell Stress, Apoptosis and Lipotoxicity s11: Inflammation**	**AKR1C1, ESR1, NR1I2 (PXR), NR1I3**
iohexol (DB01362)	**3**	**s1: Insulin Resistance and Oxidative Stress s4: Fibrosis s2: Cell Stress, Apoptosis and Lipotoxicity**	
melphalan* (DB01042)	**3**	**s3: Inflammation s5: Insulin Resistance and Oxidative Stress s6: Cell Stress, Apoptosis and Lipotoxicity**	
oxacillin (DB00713)	**3**	**s9: Insulin Resistance and Oxidative Stress s12: Fibrosis s11: Inflammation**	**SLC15A1, SLC15A2**

3.3.4 Network proximity results

As a complementary approach to prioritizing the 126 drugs from the initial CMap analysis (**Figure 3G**; **Tables 4, 6**) we constructed a NAFLD subnetwork **(Figures 3H, S1; 3.2 Methods**) and used proximity to this network [108] as an approach to potentially enhance the specificity and relevance of the CMap analysis. In essence, this algorithm connects NAFLD-associated gene signatures to drug-target profiles and maps the targets of a particular drug to the network protein nodes (**Figure 3H-J; 3.2 Methods**). Drugs with target profiles that most closely overlap with a subset of protein nodes in the NAFLD network are prioritized for pharmacological testing in our human liver biomimetic MPS experimental models (**Figure 3K** and **3.2 Methods**). The KEGG pathway database contains an annotated map of the stage-dependent progression of NAFLD (pathway id: hsa04932, [103, 109]). We used this NAFLD progression pathway as an anchor extending it with 10 interrelated pathways to generate a NAFLD subnetwork in the context of the liver protein-protein interactome (**Figures 3H, S1; 3.2 Methods**). From the total number of 9,904 DEGs (FDR p-value < .001) in our three comparisons PLI vs. PN&S, PF vs. PN&S and PF vs. PLI, (**Data file S2**) 234 DEGs mapped to these 11 NAFLD associated pathways and the background liver PPI network (**Figures 3H, S1; 3.2 Methods**). The degrees of the subnetwork nodes range from 0 to 64, with 9.7 neighbors on average for the 234 DEGs and ranges from 0 to 354, with 52.1 neighbors on average for the background liver network (**Data file S6**). Among the top 20 hub proteins (**Table 7; Data file S6**) were HSP90, MAP kinase 8 (MAPK8), NFKB essential modulator (IKBKG), protein kinase C alpha (PRKCA), caspase 8 (CASP8), signal transducer and activator of transcription 3 (STAT3), mitogen-activated protein kinase kinase kinase 7 (MAP3K7), and protein kinase C zeta type (PRKCZ).

Among the 126 unique drugs identified by our CMap analysis *per se*, 45 had targets in the liver background network (see **3.2 Methods**). These were further evaluated by determining the network proximity between their targets and the NAFLD subnetwork (**Figure S1; 3.2 Methods**) [108]. The network proximity measure for each drug was represented by a z-score ranging from -2.8 to 2.1 (**Data file S7; 3.2 Methods**). Negative z-scores indicate that the targets of the drug are more intrinsic to the disease module than a random set of targets. Therefore, the lower the z-score of a predicted drug the more likely it is to modulate the signaling in the NAFLD disease module. The 25 highest priority drugs and their known targets are shown in **Table 8**. Among the highest ranked drugs was fenoprofen, also highly ranked by signature frequency (**Table 6**) bolstering its prioritization for future testing. The HSP90 inhibitor, alvespimycin was also highly ranked by network proximity, consistent with HSP90 being a critical hub protein in the NAFLD subnetwork (**Figure S1; Table 8**; **Data file S6**). In addition, a closely related HSP90 inhibitor has been reported to modulate the activation of the NLRP3 inflammasome resulting in efficacy in murine models of NASH [125]. A hallmark of NAFLD is hepatic calcium dyshomeostasis induced by steatosis that further promotes steatosis, insulin resistance and ROS that can be ameliorated in murine NASH models by the calcium channel blocker nifedipine [126, 127]. Nifedipine and another calcium channel blocker, cinnarizine, were among the drugs ranked higher by network proximity. Two statins, fluvastatin and mevastatin were also identified by network proximity, consistent with recent meta-analyses [128, 129], suggesting the benefit of statin use in NASH development and progression.

Table 7. The 20 highest ranked hubs (proteins/targets) by degree in the NAFLD subnetwork.

The hubs are indicated by gene name and the degree is defined by the number of interactions with proteins encoded by other NAFLD DEGs. For comparison, the degree of the hub is also indicated in the context of the background human liver protein-protein interactome. This Table was generated using **Data file S6** and provides additional detail to **Figure S1.**

Rank	Gene name	Entrez gene ID	NAFLD Subnetwork Degree	Liver interactome Degree
1	HSP90AA1	3320	64	354
2	FBXO6	26270	40	220
3	MAPK1	5594	35	192
4	CDK2	1017	32	342
5	HSP90AB1	3326	32	213
6	IKBKG	8517	31	189
7	TNFRSF1A	7132	30	126
8	PIK3R1	5295	30	137
9	STAT3	6774	30	134
10	MAP3K7	6885	29	122
11	HSPA5	3309	28	214
12	MAPK8	5599	27	131
13	SHC1	6464	27	123
14	ATF2	1386	27	118
15	MAPK14	1432	26	154
16	CASP8	841	26	111
17	PRKCZ	5590	25	105
18	PRKCA	5578	25	166
19	YWHAE	7531	24	162
20	STUB1	10273	24	144

Table 8. Prioritization of CMap-predicted drugs and small-molecule perturbagens based on NAFLD subnetwork proximity.

This table is derived from **Data file S7.** The common name of the drug/small molecule with the DrugBank ID in parenthesis is shown. The Z-scores were calculated as described in the **3.2 Methods** and Guney et al.[108]. The targets are extracted from DrugBank (v5.1.4), those in red are directly in the NAFLD subnetwork (**Figure S1**; **Table 7**, and **Data file S6**). The CMap analysis was performed precisely as described in **Table 4.**

Rank	Drug name	Z-score	Targets
1	isoprenaline (DB01064)	-2.78	ADRB1, ADRB2, ADRB3, MAPK1, PIK3R1, PIK3R2, PIK3R3, PDE4A, SOD1
2	fenoprofen (DB00573)	-2.61	PTGS2, PTGS1, PPARA, PPARG
3	streptozotocin (DB00428)	-2.47	SLC2A2, MGEA5
4	palbociclib (DB09073)	-2.27	CDK4, CDK6
5	7-hydroxystaurosporine (DB01933)	-2.23	PDPK1
6	alvespimycin (DB12442)	-1.96	HSP90AA1
7	k-252a (DB02152)	-1.44	MET, RNMT, MAP2K1
8	adenosine-phosphate (DB00131)	-1.25	CREB1, PIM1, PDE4B, PYGL, PRKAB1, HINT1, PDE4D, ACSS1, ACSS2, PRKAA1, PRKAB2, ADCY1, ACSL1, FBP1, ADK
9	alfacalcidol (DB01436)	-1.22	CYP27B1, VDR, RXRA
10	cinnarizine (DB00568)	-0.77	DHX8, HRH1, DHX34, CACNA1C, CACNA1D, CACNA1F, CACNA1S, CACNA1G, CACNA1H, CACNA1I, ENTHD1, DRD2, DRD1, CHRM1
11	ambrisentan (DB06403)	-0.75	EDNRA, EDNRB
12	hexestrol (DB07931)	-0.61	AKR1C1, ESR1, NR1I2, NR1I3
13	nifedipine (DB01115)	-0.55	CACNA1C, CACNA2D1, CACNB2, CACNA1D, CACNA1S, CALM1, KCNA1, CACNA1H, NR1I2
14	mifepristone (DB00834)	-0.31	PGR, NR3C1, KLK3, KLKB1, NR1I2

Rank	Drug name	Z-score	Targets
15	fluvastatin (DB01095)	-0.26	HMGCR
16	mevastatin (DB06693)	-0.26	HMGCR
17	cytarabine (DB00987)	-0.19	POLB, POLG2
18	ephedrine (DB01364)	0.12	SLC6A2, ADRA1D, ADRA1A, SLC18A2, ACHE
19	ethinylestradiol (DB00977)	0.14	ESR1, NR1I2, SHBG
20	tetracycline (DB00759)	0.14	PRNP, PADI4
21	fluocinolone (DB00591)	0.21	NR3C1, ANXA1, ANXA2, ANXA3, ANXA4, ANXA5
22	indirubin (DB12379)	0.24	CYP1A1, AHR
23	dopamine (DB00988)	0.27	DRD2, DRD1, DRD5, DRD3, DRD4, SLC6A3, DBH, HTR1A, HTR7, SLC6A2, SLC6A4, HTR3A, HTR3B, SOD1, SLC18A2
24	flucytosine (DB01099)	0.28	DNMT1
25	vemurafenib (DB08881)	0.34	BRAF

3.4 Discussion

Guided by systems-based concepts and building upon the gene expression and pathway enrichment analyses, we implemented a QSP approach for defining NAFLD states, predicting drugs that target these states and testing the predicted drugs in human clinically relevant liver MPS NAFLD models. We defined disease states by first identifying differentially expressed genes for each of the pairwise comparisons among either the three unsupervised cluster groupings or among the three clinically defined clinical groups associated with disease progression. The differentially expressed genes that mapped to differentially enriched pathways were then categorized according to one (or more) of four categories of NAFLD pathophysiological processes in which the pathways are known to participate. This analysis resulted in two sets of twelve gene expression signatures reflecting different states of NAFLD progression. These signatures were then used to query the LINCS L1000 database to identify and rank drugs predicted to revert these gene signatures and accordingly, normalize their respective corresponding disease states [64, 99]. Among the higher CMap-ranked drugs two complementary criteria, frequency of appearance within each set of 12 signatures or NAFLD subnetwork proximity based on a predicted drug's known target profile were used for further prioritization for experimental testing.

To test the predicted drugs in a clinically relevant experimental system, we implemented a human liver acinus MPS, LAMPS, that recapitulates critical structural and functional features of the liver acinus [57, 110]. A large and diverse set of biomarkers and image-based analyses measured over time under different media that reflect normal fasting and early and late metabolic syndrome conditions, indicated that the human LAMPS also recapitulates critical aspects of NAFLD progression (e.g., simple steatosis, lipotoxicity, oxidative stress, insulin resistance, lobular inflammation, stellate cell activation and fibrosis) [58, 59]. Two mechanistically distinct drugs, obeticholic acid and pioglitazone, that have shown some clinical benefit for NAFLD, were then tested as controls and both exhibited a hepatocellular antisteatotic effect and inhibition of stellate cell activation without an appreciable effect on profibrotic markers.

We then tested the top ranked drug from an initial CMap analysis, the HDAC inhibitor vorinostat, predicted to primarily modulate inflammation and fibrosis. Consistent with the NAFLD CMap analysis and in contrast to the control drugs obeticholic acid and pioglitazone, vorinostat showed significant inhibition of proinflammatory and fibrotic biomarkers without an appreciable effect on steatosis. In addition, vorinostat ameliorated disease-induced cytotoxicity. Based on the complementary effects exhibited by vorinostat and the control drugs, the combination of vorinostat and pioglitazone was tested and demonstrated significant improvement across the full complement of NAFLD biomarkers. Altogether, these studies provide initial proof-of-concept for a patient-derived QSP platform that can infer disease states from gene expression signatures, predict drugs and drug combinations that can target these disease states and experimentally test these predictions in clinically relevant NAFLD models.

With the recent expansion of the LINCS L1000 database, we have identified several drugs predicted to be more efficacious than vorinostat for future testing and providing mechanistic inferences. Several of these predicted drugs have known interactions with proteins associated with NAFLD such as nuclear receptors, and bile and fatty acid transporters. In contrast, others had no known interactions with targets associated with NAFLD despite being predicted to reverse many of the same signatures. These drugs were either highly selective for a particular target such as topoisomerase (e.g., SN-38) or were antibiotics having minimum interactions with human proteins. Further analysis suggested a common thread among many of the predicted drugs that involve nuclear receptors such as PXR [130] and the related constitutive androstane receptor. PXR is a transcriptional regulator capable of interacting with diverse exogenous and endogenous ligand modulators that has evolved in the liver to have xenobiotic/endobiotic metabolic functions in addition to functions regulating glucose/lipid metabolism/energy, inflammation, and stellate cell activation. Traditional targeted drug discovery approaches have identified FXR and PPAR agonists converging on this broader family of nuclear receptors intimately associated with NAFLD pathophysiology.

4.0 Determine the extent that the experimental LAMPS NAFLD model of disease progression recapitulates patient progression at the transcriptome level

4.1 Introduction

As discussed in the main introduction, one of the limiting factors in drug discovery has been the use of models which are not predictive of response in humans [46, 51]. It is therefore critical that the mechanisms driving the phenotype in the experimental model translate to patients. This concept is called the “chain of transmissibility” which can be established through disease relevant gene expression patterns [54]. We have previously shown that the LAMPS NAFLD models are able to phenotypically recapitulate NAFLD [57-59, 102]. However it is important that the phenotypes occur through clinically relevant mechanisms [46]. For example, CCL4 treatment induces fibrosis in mice, but the pathogenesis is distinct from patients as other features such as insulin resistance are absent [131].

To further establish the chain of transmissibility between NAFLD patients and the LAMPS models, we compared the transcriptomes of the LAMPS NAFLD models to patients with similar disease phenotypes. This was done by first training a machine learning model, to differentiate between the disease stages using the patient transcriptome data, and then using this machine learning model to predict the disease stage of the individual LAMPS NAFLD models. More specifically, I used a multinomial logistic regression with elastic net penalization (MLENet) model, which have been used in a variety of applications [132-135]. This particular model was used because it is a feature selecting classifier, which unbiasedly selected the most biologically relevant genes while discarding irrelevant genes. Salvadores et al. [135], performed a study similar to the one in this chapter in which they used an MLENet model to compare cancer cell lines to cancer subtypes [135].

We then examined the concordance of differentially expressed/enriched pathways and genes between the LAMPS and patient pairwise comparisons. This was done so that we could see if specific pathways were congruent with patient NAFLD. These results are important for determining qualitatively whether specific mechanisms are recapitulated in the LAMPS NAFLD models. This is in contrast to mouse models which have little overlap with patients [136].

4.2 Methods

4.2.1 Performing RNA-seq on the LAMPS NAFLD models

Separate LAMPS experiments were carried out as described above and previously from our group [58]: LAMPS devices were treated with media mimicking metabolic conditions such as normal fasting (NF), early metabolic syndrome (EMS), and late metabolic syndrome (LMS) (**Figure 3L**). The LAMPS experiments were carried out at 3-time points: 4, 7, and 10 days with all 3 media conditions (3-4 replicates). Total RNA was extracted from the liver LAMPS chips using Qiazol Reagent (Sigma, USA # R4533) and a 1-Bromo-3 chloropropane (BCP) (Sigma, USA #B9673) phase separation reagent. Further, the aqueous phase of the samples was adsorbed onto Qiagen RNEasy Mini cleanup columns (Qiagen#74204) and subjected to DNAse treatment (Qiagen#79254) to avoid DNA contamination. Subsequently, the purified RNA was eluted using RNase-free distilled water after washing with 80% ethanol. RNA purity was checked using the

Nanophotometer (IMPLEN, USA). RNA degradation and contamination was monitored on 1% agarose gels. The integrity of RNA was assessed by RNA Nano 6000 Assay Kitof the Agilent 2100 bioanalyzer (Agilent Technologies, USA). Samples were required to have a minimum of 200 ng RNA and RIN value greater than 4.0.

A total of 1 µg of total RNA was used as input to each sample preparation. Sequencing libraries were generated using NEBNext Ultra RNA Library Prep Kit for Illumina (NEB, USA). Briefly, mRNA was purified from total RNA using poly-T oligo-attached magnetic beads. Fragmentation was carried out using divalent cations under elevated temperature in NEB Next First Strand Synthesis Reaction Buffer (5X). First strand cDNA was synthesized using random hexamer primer and M-MuLV Reverse Transcriptase (RNase H-). Second strand cDNA synthesis was subsequently performed using DNA Polymerase I and RNase H. Remaining overhangs were converted into blunt ends via exonuclease/polymerase activities. After adenylation of 3’ ends of DNA fragments, NEB Next Adaptor with hairpin loop structure were ligated to prepare for hybridization. To select cDNA fragments of preferentially 150~200 bp in length, the library fragments were purified with AMPure XP system (Beckman Coulter, Beverly, USA). Then 3 µl USER Enzyme (NEB, USA) was used with size-selected, adaptor-ligated cDNA at 37 °C for 15 min followed by 5 min at 95 °C before PCR. Then PCR was performed with Phusion High-Fidelity DNA polymerase, Universal PCR primers and Index (X) Primer. Then, PCR products were purified (AMPure XP system) and library quality was assessed on the Agilent Bioanalyzer 2100 system. Samples were required to have a cDNA library concentration > 0.5 ng/microL, a single qPCR peak at 2nM-30nM, no adapter contaminations or primer dimers, and product size of 350-520 bp.

The clustering of the index-coded samples was performed on a cBot Cluster Generation System using PE Cluster Kit cBot-HS (Illumina) according to the manufacturer's instructions. After cluster generation, the library preparations were sequenced on an Illumina platform and 125 bp/150 bp paired-end reads were generated.

4.2.2 Concordance analysis of differentially enriched pathways in patients and LAMPS

The raw LAMPS transcriptome data (accessible following the instructions at https://github.com/lefeverde/QSPpaper) were processed using the same pipeline as described for the patients (**Figure 3L**). Differentially expressed genes were identified using the standard LIMMA-VOOM protocol [78, 79] in which the genes were fit with a linear model for media treatment and timepoint. As we are interested in the treatment effects, time point was treated here as confounding variable [137]. We identified differentially expressed genes (**Data file S8**) for LAMPS by performing three pairwise comparisons consisting of EMS vs NF, LMS vs NF, and LMS vs EMS, which are meant to be analogous to the patient pairwise comparisons (Lob vs. N&S, Fib vs. N&S, and Fib vs. Lob). The phenotypes of NF, EMS, and LMS range from minimal, moderate, and pronounced levels of steatosis, inflammation, and fibrosis, respectively [58] (**Figure 14B**). Differentially enriched pathways were identified by ranking the genes by *t*-statistic for each pairwise comparison and then performing GSEA [83] using the MSigDB v7.0 C2 KEGG pathways [63] for both the LAMPS and patient comparisons (**Figures 3L, 17; Data file S9**).

Using this differential enrichment pathway analysis as input, we performed a concordance analysis of the LAMPS and matched patient pairwise comparisons (**Figures 3L, 16**). A pathway was considered concordant if it was significantly (FDR p–value $< .05$) regulated in the same direction in both the LAMPS and matched patient pairwise comparisons (**Figure 16**). Conversely, discordance indicates that a differentially enriched pathway identified in both comparisons, is regulated in opposite directions.

4.2.3 Comparing LAMPS NAFLD model transcriptomes to patients via multinomial logistic regression with elastic net penalization (MLENet)

We used an MLENet model [138] to compare the LAMPS to patients since this is a classifier that performs feature (i.e., gene) selection (**Figure 3L**; For details see https://github.com/lefeverde/QSPpaper). The patient gene expression data (accessible following the instructions at https://github.com/lefeverde/QSPpaper) was prepared by first ranking the genes by variance and taking the top 7,500 (this is done to reduce overfitting by removing uninformative features). The same variance thresholding was applied to the LAMPS expression matrix (see https://github.com/lefeverde/QSPpaper). Next genes which were not in both the variance filtered LAMPS and patient expression matrixes were removed from both, yielding a set of 4057 genes. For the LAMPS gene expression matrix, we used surrogate variable analysis [80, 81] to predict and then remove unwanted sources of variation (timepoint, and possible cell ratio differences). Both the patient and LAMPS matrixes were standardized (gene-wise) to have zero mean and unit variance.

We used a nested cross-validation approach to ensure that MLENet could successfully differentiate between the 4 patient histological classifications (Normal, Steatosis, Lobular inflammation, or Fibrosis). To do this, we used the Glmnet package [138] applying the appropriate distribution (multinomial) and setting (alpha=.95) that in initial trials enabled optimal performance for classifying the LAMPS samples. The nested cross-validation was performed by first generating

100 sets of training and test data (**Figure 14A**). This was done by sampling 70% of the patient from each class to create a training subset and then using the remaining 30% for the testing subset (**Figure 14A**). For each of the 100 sets, we trained an MLENet model on the training subset using *cv.glmnet* [138] and then used the testing subset to evaluate the model's performance by calculating the specificity and sensitivity of the 4 patient classes (**Figure 14A**).

After ensuring that that the MLENet approach could accurately classify patients with a mean (numbers in parenthesis are standard deviation) specificity of .93 (.03), .83 (.03), .98 (.02), .95 (.03) for Normal, Steatosis, Lobular inflammation, and Fibrosis respectively, we trained a final model using the 182 patients using the parameters described above (**Figures 3L, 14B**). The final MLENet model selected 71 genes, of which, the majority (80%) had prior association with NAFLD in independent studies (usually being differentially expressed in other studies, see **Data file S10**). We used this final MLENet model to classify the LAMPS samples as belonging to one of the 4 patient classes (**Figure 14B;** for details see https://github.com/lefeverde/QSPpaper).

4.3 Results

4.3.1 LAMPS Data QC and exploratory analyses

PCA of the LAMPS transcriptome data suggested that no major artifacts are present, and that the experimental variables timepoint and media treatment are responsible for the majority of the variance (**Figure 13**). The later time points, (days 7 & 10) are mostly mixed together, suggesting that the overall transcriptome differences between these time points is minor compared to the differences between the later timepoints (days 7 & 10) and the early timepoint (day 4) (**Figure 13**).

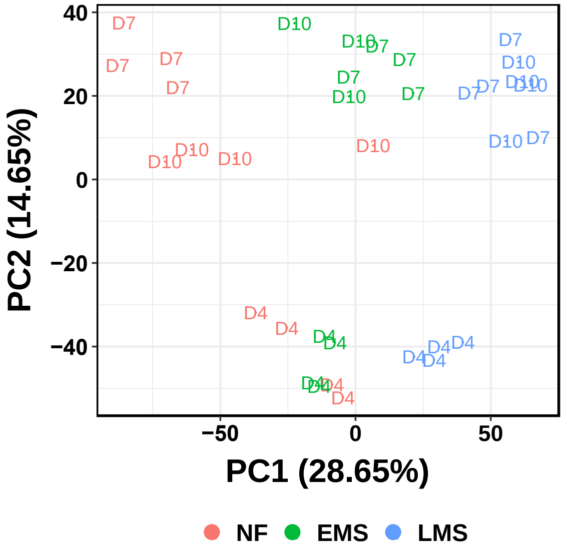

Figure 13. PCA plot of the LAMPS NAFLD model transcriptomes suggests no technical artifacts are present in the data.

Principal component analysis (PCA) of the log2(CPM) gene expression values show that the experimental variables, timepoint and media treatment drive the global transcriptomic variation. Notably, Day 4 is separated from the later timepoints (Days 7 & 10). The Day 4 NF and EMS are mixed however this would expected because they are just starting to be treated with EMS media.

4.3.2 MLENet results

To gain further evidence supporting the clinical relevance of the LAMPS NAFLD model, we implemented a machine learning approach based on transcriptomic analysis of the 182 patient cohort [61] described in (**Figure 3L**). We first trained a multinomial logistic regression with elastic net penalization model (MLENet) using nested cross-validation to successfully differentiate among 4 clinical classifications of NAFLD (**Figure 14**). The final model used 71 genes with 80% of these having prior association with NAFLD (**Figure 15**, **Data file S10**). Using this patient-based model, we then classified the transcriptome of individual LAMPS under three media conditions, normal fasting (NF), early metabolic syndrome (EMS), and late metabolic syndrome (LMS) as shown in **Figures 3L, 14B and 4.2 Methods**. At the transcriptome level, progression of NAFLD in LAMPS upon media treatment mimics disease progression observed in patients, independently corroborating the biomarker and imaging data (**Figures 3L, 14B**).

The comparatively low true positive rate for the steatosis class can be attributed to the ambiguity of these patients with respect to the other classes, rather than poor performance of the of the machine learning model. This can be observed by noting that the "misclassifications" are not randomly distributed between the 3 other classes, but follow the expected similarity of patient classifications. The majority of the misclassified steatosis patients were classified as normal but few as fibrosis. Because the source of this error is biological, improving the accuracy with respect to the steatosis class will cause the machine learning model to overfit. Interestingly these results are consistent with the clustering analysis in Figure 2 showing the difficulty of distinguishing between normal and steatosis solely at the RNA level.

A

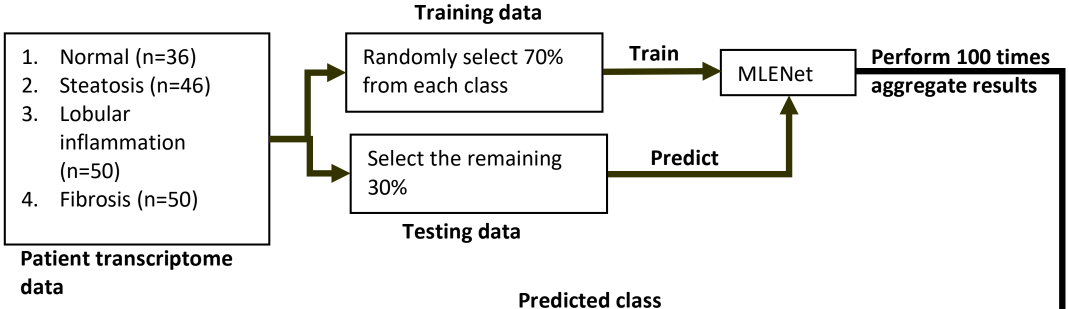

Predicted class

Actual Class	Normal	Steatosis	Lob	Fibrosis
Normal	794 (72.2%)	306 (27.8%)	0 (0%)	0 (0%)
Steatosis	459 (32.8%)	609 (43.5%)	278 (19.9%)	54 (3.9%)
Lob	7 (0.5%)	17 (1.1%)	1420 (94.7%)	56 (3.7%)
Fibrosis	17 (1.1%)	68 (4.5%)	177 (11.8%)	1238 (82.5%)

B

Phenotype matching of LAMPS to patients

LAMPS treatment	LAMPS Biomarker	Patient phenotype
NF	○ Mild steatosis (LipidTOX)	Normal, Steatosis
EMS	○ Increased steatosis (LipidTOX) ○ Oxidative stress (biosensor) ○ Stellate cell activation (α-SMA expression) ○ Secretion of inflammatory cytokines (TNF-α, IL-6, IL-8, IL-1β, MCP-1) ○ Secretion of fibrotic markers (pro-col 1A1 and TIMP-1)	Steatosis, Lob.
LMS	○ Further increase in EMS metrics ○ Hepatic ballooning (CK8/18) ○ Hepatic insulin resistance (FOXO1 biosensor)	Lob., Fibrosis

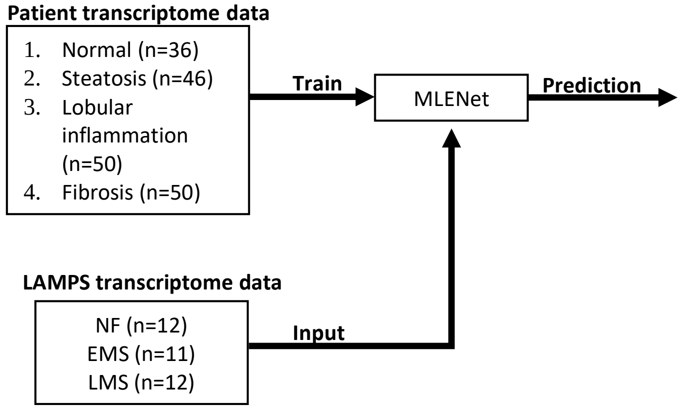

Predicted patient class

LAMPS Class	Normal	Steatosis	Lob	Fibrosis
NF	8	4	-	-
EMS	2	6	1	2
LMS	-	-	1	11

Classification of LAMPS using the ML model trained on patients

Figure 14. Unbiased machine learning model of patient transcriptomic data identifies and predicts congruent clinical phenotypes within LAMPS.

(**A**) The bootstrapping procedure used to develop and validate the transcriptome-based machine learning model (MLENet) capable of differentiating and predicting 4 NAFLD patient classifications (see Methods) (red indicates the clinically defined true positives). The average sensitivity (numbers in parenthesis are standard deviations) are: .66 (.11), .64 (.12), .77 (.08), .93 (.07); average specificity .93 (.03), .83 (.03), .98 (.02), .95 (.03) for Normal, Steatosis, Lob, and Fibrosis respectively. **B**) The workflow and table of outcomes from implementing MLENet to identify and predict congruent NAFLD patient phenotypes from LAMPS transcriptomic analytes generated under normal fasting (NF); early metabolic syndrome (EMS); or late metabolic syndrome (LMS) conditions (see Methods). The phenotype matching of LAMPS to patients results from extensive parallel biochemical and imaging analyses [58] indicating that the three different media conditions drive distinct phenotypes congruent with clinical phenotypes of NAFLD progression and are independently consistent with the machine learning approach.

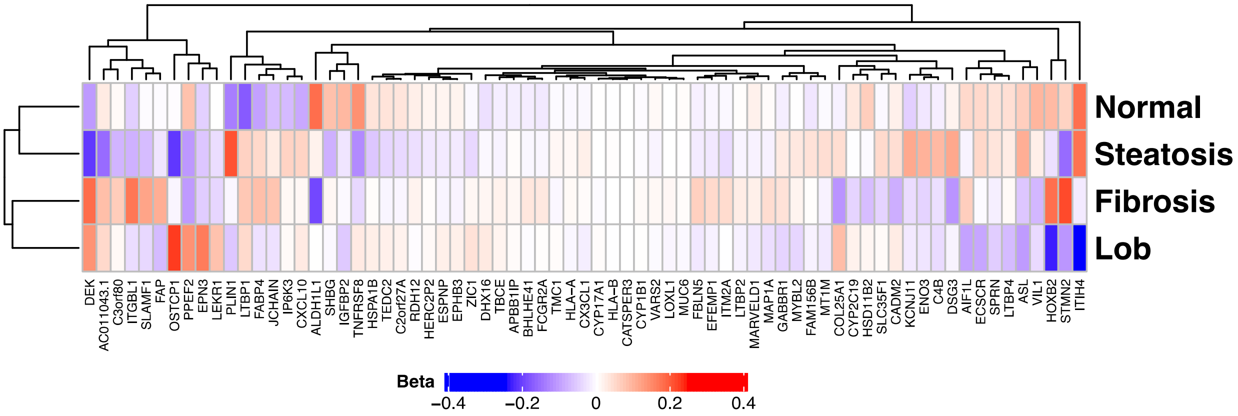

Figure 15. Heatmap of the beta coefficients (i.e., weights) of the 71 features selected by MLENet to differentiate between the patient classes.

The values can be interpreted as representing the association with each of the 4 patient classes. Approximately 80% of these genes have some prior association with NAFLD **(Data file S10)**.

4.3.3 LAMPS Differentially expressed/enriched gene and pathways show statistically significant concordance with patients

The concordance analyses of the genes (**Figure 16**) and pathways (**Figure 17)** further support the LAMPS "chain of transmissibility". Some notable concordant pathways which are consistently upregulated in NAFLD patients include: Focal adhesion, ECM, and T Cell receptor interaction [139]. Oxidative phosphorylation is downregulated in LAMPS and patients[139]. There are also several pathways which are concordant between LAMPS and patients, but discordant with respect to patients and mouse models. Ribosome is upregulated in LAMPS and patients, but downregulated in many mouse models [136]. PPAR signaling [140], Valine, leucine and isoleucine degradation [141], Lysine degradation, Starch and sucrose metabolism, and Butanoate metabolism were down regulated in LAMPS and patients but notably upregulated in NAFLD mouse models.

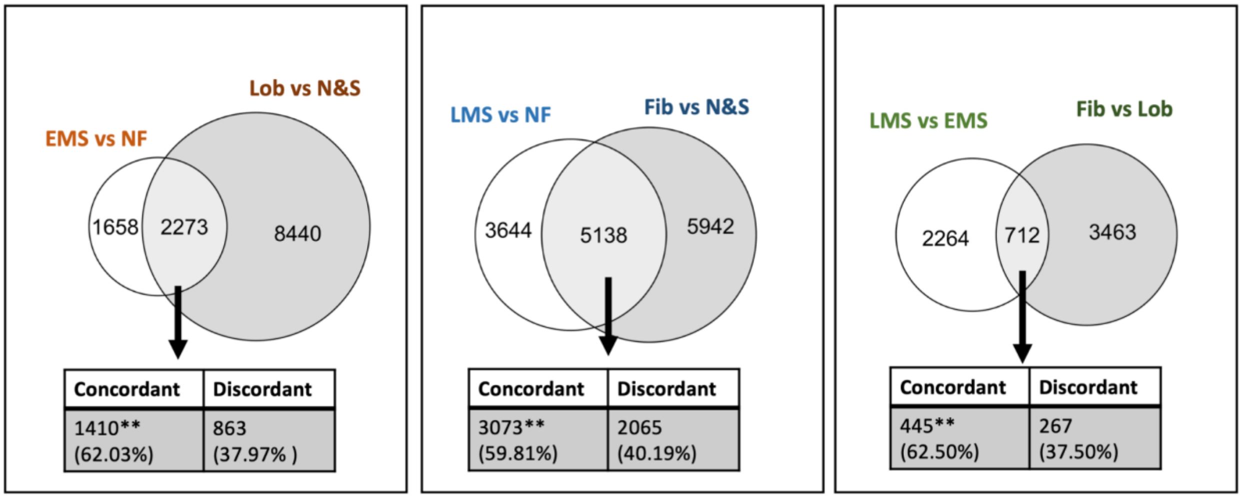

Figure 16. Concordance analysis of the differentially expressed genes in the LAMPS (left circle) and phenotypically matched patient pairwise comparisons (right circle).

A gene was considered concordant if it was significantly expressed (FDR p-value < .05) in the same direction (up/down) in the LAMPS and patient comparisons, discordance is when genes are differentially expressed but have opposite signs. *FDR p-value < .01 **p-value <= 1.3e-11 (Exact Binomial Test, % is estimated effect size)

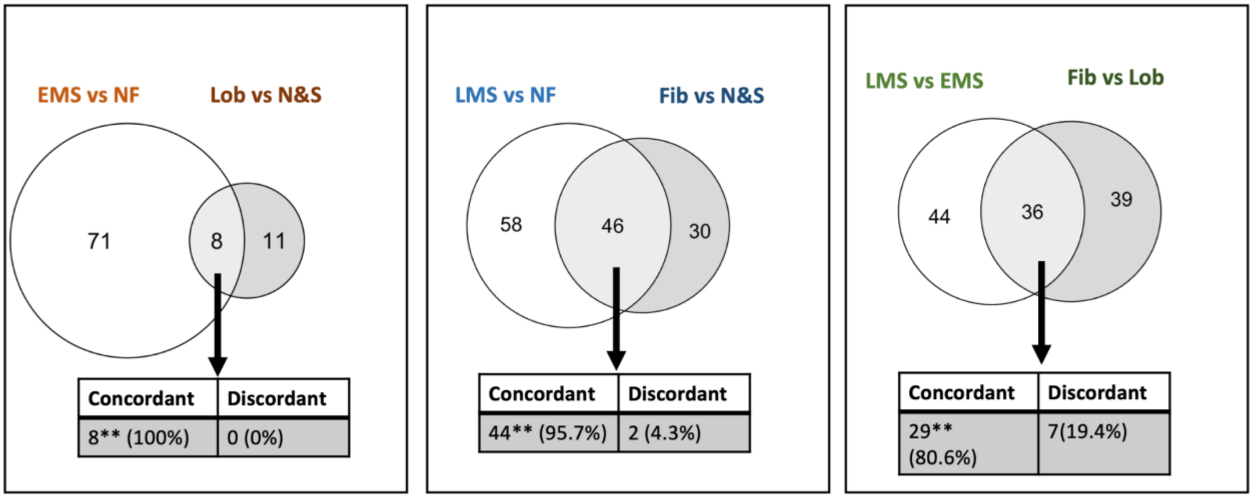

Figure 17. Concordance analysis of the differentially enriched pathways in the LAMPS (left circle) and phenotypically matched patient pairwise comparisons (right circle).

The pathways were identified using GSEA as described in the Methods for the pairwise comparisons. A pathway was considered concordant if it was significantly regulated (FDR p-value < .05) in the same direction (up/down) in the LAMPS and patient comparisons, discordance is when pathways are differentially expressed but have opposite signs

4.4 Discussion

With the translational goal in mind of identifying disease modifying therapies, it is important to know if these clinical phenotypes observed pre-clinically, arise through those mechanisms that occur in patients. To further establish the clinical relevance of LAMPS NAFLD model, we implemented a machine learning approach. We trained a transcriptome–based machine learning model from the 182 NAFLD cohort representing a full spectrum of disease progression subtypes to classify patients with high specificity. We then implemented this patient-based model consisting of 71 genes, with 57 of these having an independently determined association with NAFLD, to classify the transcriptomes of individual LAMPS models treated under media conditions mirroring different stages of disease progression. The congruence between the patient-derived transcriptome-based classification of individual LAMPS and the diverse panel of NAFLD associated biomarker measurements supports the clinical relevance of the LAMPS as a NAFLD model. The results from this Aim have given us confidence that our model is clinically relevant, and so we will expand the experimental testing of the predicted compounds.

5.0 General discussion

5.1 Conclusion

This project demonstrates how a comprehensive and unbiased approach to drug discovery (as guided by QSP) and harnessing the power of biomimetic human MPS can be used to identify drugs for NAFLD and other complex diseases. In essence, the systems-based platform described here can inform therapeutic strategies that are inherently more pleiotropic than traditional approaches and thus has the potential to address the complexity of transcriptional dysregulation intrinsic to diseases such as NAFLD [142]. The finding that this can be achieved by repurposing approved drugs suggests that acceptable therapeutic indices could result by selectively modulating disease states. Additionally, the identification of pathways involved could also lead to identifying novel targets for drug discovery. In conjunction with the advances in patient-derived iPSC technology [143] and in situ methods for RNA, metabolomic, and proteomic analyses, we anticipate the QSP platform described in this study will become a mainstay for a personalized approach towards developing effective NAFLD therapeutic strategies.

5.2 Future directions

Studies are currently being carried out by Mark T. Meidel to test more of the predicted drugs. He has generated preliminary results suggesting that SN-38 and Sulfanitran have some efficacy in ameliorating NAFLD. Both drugs appear effective in reducing steatosis while SN-38 can also reduce fibrosis, which was predicted by the CMap analysis. Further work is being done to determine these drugs effect’s on inflammatory and stress readouts. This is further confirmation of the approach presented here. Future studies will test more of the predicted compounds and successful compounds will be used as mechanistic probes. Optimal drugs and combinations that show great promise will initiate a clinical trial.

The approach outlined in this dissertation can be used as a basis for future work. First, it provides a way of rationally selecting drug combinations which normalize complementary disease features. This was demonstrated experimentally using the combination of pioglitazone and vorinostat, which normalized the full set of NAFLD biomarkers. Second, extending the integrative QSP approach used here can pave the way for creating patient “digital twins”. This will be done by combining deep phenotyping of patients with omics to allow for an unbiased, holistic picture of disease states. In parallel, microphysiology experimental models using patient-derived iPSC cells are being developed to experimentally account for heterogeneous genomic and disease backgrounds. While this can be directly used for personalized medicine purposes, it also allows for the potential of combining patient clinical twins combined with patient biomimetic twins (i.e., MPS of specific patient cells) to predict and test effect of drugs on specific patient cohorts. The QSP approach demonstrated in this project can be readily applied for other diseases in which the mechanisms are poorly recapitulated in animals (e.g., Asthma).

6.0 Acknowledgements

6.1 Chapter 2

All of the analysis presented in chapter 2 were carried out by me except most of the pathway categorization was performed by Fen Pei.

6.2 Chapter 3

The drug prediction analyses were all carried out by me. Mark T. Miedel performed the LAMPS experiments.

6.3 Chapter 4

All of the RNA-seq analyses were performed by me, Manush Saydmohammed carried out the LAMPS experiments.

Bibliography

1. Hardy, T., F. Oakley, Q.M. Anstee, and C.P. Day, *Nonalcoholic Fatty Liver Disease: Pathogenesis and Disease Spectrum.* Annu Rev Pathol, 2016. **11**: p. 451-96.

2. Ayonrinde, O.T., *Historical narrative from fatty liver in the nineteenth century to contemporary NAFLD – Reconciling the present with the past.* JHEP Reports, 2021. **3**(3): p. 100261.

3. Geier, A., D. Tiniakos, H. Denk, and M. Trauner, *From the origin of NASH to the future of metabolic fatty liver disease.* Gut, 2021. **70**(8): p. 1570-1579.

4. Eslam, M., A.J. Sanyal, and J. George, *MAFLD: A Consensus-Driven Proposed Nomenclature for Metabolic Associated Fatty Liver Disease.* Gastroenterology, 2020. **158**(7): p. 1999-2014.e1.

5. Brunt, E.M., D.E. Kleiner, D.H. Carpenter, M. Rinella, S.A. Harrison, R. Loomba, Z. Younossi, B.A. Neuschwander-Tetri, and A.J. Sanyal, *NAFLD: Reporting Histologic Findings in Clinical Practice.* Hepatology, 2021. **73**(5): p. 2028-2038.

6. Fraile, J.M., S. Palliyil, C. Barelle, A.J. Porter, and M. Kovaleva, *Non-Alcoholic Steatohepatitis (NASH) - A Review of a Crowded Clinical Landscape, Driven by a Complex Disease.* Drug Des Devel Ther, 2021. **15**: p. 3997-4009.

7. Sanyal, A.J., *Past, present and future perspectives in nonalcoholic fatty liver disease.* Nat Rev Gastroenterol Hepatol, 2019. **16**(6): p. 377-386.

8. Loomba, R., S.L. Friedman, and G.I. Shulman, *Mechanisms and disease consequences of nonalcoholic fatty liver disease.* Cell, 2021. **184**(10): p. 2537-2564.

9. Younossi, Z.M., G. Marchesini, H. Pinto-Cortez, and S. Petta, *Epidemiology of Nonalcoholic Fatty Liver Disease and Nonalcoholic Steatohepatitis: Implications for Liver Transplantation.* Transplantation, 2019. **103**(1): p. 22-27.

10. Anstee, Q.M., H.L. Reeves, E. Kotsiliti, O. Govaere, and M. Heikenwalder, *From NASH to HCC: current concepts and future challenges.* Nat Rev Gastroenterol Hepatol, 2019. **16**(7): p. 411-428.

11. Brunt, E.M., D.E. Kleiner, L.A. Wilson, P. Belt, and B.A. Neuschwander-Tetri, *Nonalcoholic fatty liver disease (NAFLD) activity score and the histopathologic diagnosis in NAFLD: distinct clinicopathologic meanings.* Hepatology, 2011. **53**(3): p. 810-20.

12. Paul, J., *Recent advances in non-invasive diagnosis and medical management of non-alcoholic fatty liver disease in adult.* Egyptian Liver Journal, 2020. **10**(1): p. 37.

13. Siegel, A.B. and A.X. Zhu, *Metabolic syndrome and hepatocellular carcinoma: two growing epidemics with a potential link.* Cancer, 2009. **115**(24): p. 5651-61.

14. Friedman, S.L., B.A. Neuschwander-Tetri, M. Rinella, and A.J. Sanyal, *Mechanisms of NAFLD development and therapeutic strategies.* Nature Medicine, 2018. **24**(7): p. 908-922.

15. Adams, L.A., J.F. Lymp, J. St. Sauver, S.O. Sanderson, K.D. Lindor, A. Feldstein, and P. Angulo, *The Natural History of Nonalcoholic Fatty Liver Disease: A Population-Based Cohort Study.* Gastroenterology, 2005. **129**(1): p. 113-121.

16. Angulo, P., D.E. Kleiner, S. Dam-Larsen, L.A. Adams, E.S. Bjornsson, P. Charatcharoenwitthaya, P.R. Mills, J.C. Keach, H.D. Lafferty, A. Stahler, et al., *Liver Fibrosis, but No Other Histologic Features, Is Associated With Long-term Outcomes of Patients With Nonalcoholic Fatty Liver Disease.* Gastroenterology, 2015. **149**(2): p. 389-97.e10.

17. Ekstedt, M., H. Hagström, P. Nasr, M. Fredrikson, P. Stål, S. Kechagias, and R. Hultcrantz, *Fibrosis stage is the strongest predictor for disease-specific mortality in NAFLD after up to 33 years of follow-up.* Hepatology, 2015. **61**(5): p. 1547-54.

18. Grgurevic, I., K. Podrug, I. Mikolasevic, M. Kukla, A. Madir, and E.A. Tsochatzis, *Natural History of Nonalcoholic Fatty Liver Disease: Implications for Clinical Practice and an Individualized Approach.* Can J Gastroenterol Hepatol, 2020. **2020**: p. 9181368.

19. Ipsen, D.H., J. Lykkesfeldt, and P. Tveden-Nyborg, *Molecular mechanisms of hepatic lipid accumulation in non-alcoholic fatty liver disease.* Cell Mol Life Sci, 2018. **75**(18): p. 3313-3327.

20. Singh, S., A.M. Allen, Z. Wang, L.J. Prokop, M.H. Murad, and R. Loomba, *Fibrosis progression in nonalcoholic fatty liver vs nonalcoholic steatohepatitis: a systematic review and meta-analysis of paired-biopsy studies.* Clin Gastroenterol Hepatol, 2015. **13**(4): p. 643-54.e1-9; quiz e39-40.

21. Rich, N.E., S. Oji, A.R. Mufti, J.D. Browning, N.D. Parikh, M. Odewole, H. Mayo, and A.G. Singal, *Racial and Ethnic Disparities in Nonalcoholic Fatty Liver Disease Prevalence, Severity, and Outcomes in the United States: A Systematic Review and Meta-analysis.* Clin Gastroenterol Hepatol, 2018. **16**(2): p. 198-210.e2.

22. Yu, E.L. and J.B. Schwimmer, *Epidemiology of Pediatric Nonalcoholic Fatty Liver Disease.* Clinical Liver Disease, 2021. **17**(3): p. 196-199.

23. Godoy-Matos, A.F., W.S. Silva Júnior, and C.M. Valerio, *NAFLD as a continuum: from obesity to metabolic syndrome and diabetes.* Diabetology & Metabolic Syndrome, 2020. **12**(1): p. 60.

24. Mitra, S., A. De, and A. Chowdhury, *Epidemiology of non-alcoholic and alcoholic fatty liver diseases.* Transl Gastroenterol Hepatol, 2020. **5**: p. 16.

25. Younossi, Z., Q.M. Anstee, M. Marietti, T. Hardy, L. Henry, M. Eslam, J. George, and E. Bugianesi, *Global burden of NAFLD and NASH: trends, predictions, risk factors and prevention.* Nat Rev Gastroenterol Hepatol, 2018. **15**(1): p. 11-20.

26. Targher, G., K.E. Corey, C.D. Byrne, and M. Roden, *The complex link between NAFLD and type 2 diabetes mellitus - mechanisms and treatments.* Nat Rev Gastroenterol Hepatol, 2021. **18**(9): p. 599-612.

27. Brar, G., T.F. Greten, B.I. Graubard, T.S. McNeel, J.L. Petrick, K.A. McGlynn, and S.F. Altekruse, *Hepatocellular Carcinoma Survival by Etiology: A SEER-Medicare Database Analysis.* Hepatol Commun, 2020. **4**(10): p. 1541-1551.

28. Huang, D.Q., H.B. El-Serag, and R. Loomba, *Global epidemiology of NAFLD-related HCC: trends, predictions, risk factors and prevention.* Nat Rev Gastroenterol Hepatol, 2021. **18**(4): p. 223-238.

29. Kasper, P., A. Martin, S. Lang, F. Kütting, T. Goeser, M. Demir, and H.-M. Steffen, *NAFLD and cardiovascular diseases: a clinical review.* Clinical Research in Cardiology, 2021. **110**(7): p. 921-937.

30. Eslam, M. and J. George, *Genetic contributions to NAFLD: leveraging shared genetics to uncover systems biology.* Nature Reviews Gastroenterology & Hepatology, 2020. **17**(1): p. 40-52.

31. Cui, J., C.H. Chen, M.T. Lo, N. Schork, R. Bettencourt, M.P. Gonzalez, A. Bhatt, J. Hooker, K. Shaffer, K.E. Nelson, et al., *Shared genetic effects between hepatic steatosis and fibrosis: A prospective twin study.* Hepatology, 2016. **64**(5): p. 1547-1558.

32. Eichler, E.E., J. Flint, G. Gibson, A. Kong, S.M. Leal, J.H. Moore, and J.H. Nadeau, *Missing heritability and strategies for finding the underlying causes of complex disease.* Nat Rev Genet, 2010. **11**(6): p. 446-50.

33. Trépo, E. and L. Valenti, *Update on NAFLD genetics: From new variants to the clinic.* J Hepatol, 2020. **72**(6): p. 1196-1209.

34. Gatlin, A. *Madrigal Pharma Stock Soars 268% After Knocking NASH Study Out Of The Park* 2022; Available from: https://www.investors.com/news/technology/mdgl-stock-triples-after-knocking-nash-study-out-of-the-park/.

35. Drenth, J.P.H. and J.M. Schattenberg, *The nonalcoholic steatohepatitis (NASH) drug development graveyard: established hurdles and planning for future success.* Expert Opin Investig Drugs, 2020. **29**(12): p. 1365-1375.

36. Ratziu, V., F. Charlotte, A. Heurtier, S. Gombert, P. Giral, E. Bruckert, A. Grimaldi, F. Capron, and T. Poynard, *Sampling variability of liver biopsy in nonalcoholic fatty liver disease.* Gastroenterology, 2005. **128**(7): p. 1898-906.

37. Davison, B.A., S.A. Harrison, G. Cotter, N. Alkhouri, A. Sanyal, C. Edwards, J.R. Colca, J. Iwashita, G.G. Koch, and H.C. Dittrich, *Suboptimal reliability of liver biopsy evaluation has implications for randomized clinical trials.* J Hepatol, 2020. **73**(6): p. 1322-1332.

38. Swinney, D.C. and J. Anthony, *How were new medicines discovered?* Nat Rev Drug Discov, 2011. **10**(7): p. 507-19.

39. Scannell, J.W., A. Blanckley, H. Boldon, and B. Warrington, *Diagnosing the decline in pharmaceutical R&D efficiency.* Nature Reviews Drug Discovery, 2012. **11**: p. 191 EP.

40. Lombardino, J.G. and J.A. Lowe, 3rd, *The role of the medicinal chemist in drug discovery--then and now.* Nat Rev Drug Discov, 2004. **3**(10): p. 853-62.

41. Sams-Dodd, F., *Target-based drug discovery: is something wrong?* Drug Discov Today, 2005. **10**(2): p. 139-47.

42. Scannell, J.W. and J. Bosley, *When Quality Beats Quantity: Decision Theory, Drug Discovery, and the Reproducibility Crisis.* PLOS ONE, 2016. **11**(2): p. 1-21.

43. Keene, C.D., M. Darvas, B. Kraemer, D. Liggitt, C. Sigurdson, and W. Ladiges, *Neuropathological assessment and validation of mouse models for Alzheimer's disease: applying NIA-AA guidelines.* Pathobiol Aging Age Relat Dis, 2016. **6**: p. 32397.

44. Seok, J., H.S. Warren, A.G. Cuenca, M.N. Mindrinos, H.V. Baker, W. Xu, D.R. Richards, G.P. McDonald-Smith, H. Gao, and L. Hennessy, *Genomic responses in mouse models poorly mimic human inflammatory diseases.* Proceedings of the National Academy of Sciences, 2013. **110**(9): p. 3507-3512.

45. Swinney, D.C. and J.A. Lee, *Recent advances in phenotypic drug discovery.* F1000Res, 2020. **9**.

46. Cook, D., D. Brown, R. Alexander, R. March, P. Morgan, G. Satterthwaite, and M.N. Pangalos, *Lessons learned from the fate of AstraZeneca's drug pipeline: a five-dimensional framework.* Nature Reviews Drug Discovery, 2014. **13**(6): p. 419-431.

47. Horrobin, D.F., *Innovation in the pharmaceutical industry.* Journal of the Royal Society of Medicine, 2000. **93**(7): p. 341-345.

48. Paul, S.M., D.S. Mytelka, C.T. Dunwiddie, C.C. Persinger, B.H. Munos, S.R. Lindborg, and A.L. Schacht, *How to improve R&D productivity: the pharmaceutical industry's grand challenge.* Nat Rev Drug Discov, 2010. **9**(3): p. 203-14.

49. Sorger, P.K., S.R.B. Allerheiligen, D.R. Abernethy, R.B. Altman, K.L.R. Brouwer, A. Califano, D.Z. D'Argenio, R. Iyengar, W.J. Jusko, R. Lalonde, et al. *Quantitative and systems pharmacology in the post-genomic era: new approaches to discovering drugs and understanding therapeutic mechanisms*. in *An NIH white paper by the QSP workshop group*. 2011.

50. Stern, A.M., M.E. Schurdak, I. Bahar, J.M. Berg, and D.L. Taylor, *A Perspective on Implementing a Quantitative Systems Pharmacology Platform for Drug Discovery and the Advancement of Personalized Medicine.* J Biomol Screen, 2016. **21**(6): p. 521-34.

51. Horvath, P., N. Aulner, M. Bickle, A.M. Davies, E.D. Nery, D. Ebner, M.C. Montoya, P. Östling, V. Pietiäinen, L.S. Price, et al., *Screening out irrelevant cell-based models of disease.* Nat Rev Drug Discov, 2016. **15**(11): p. 751-769.

52. Hebbard, L. and J. George, *Animal models of nonalcoholic fatty liver disease.* Nat Rev Gastroenterol Hepatol, 2011. **8**(1): p. 35-44.

53. Mann, J.P., R.K. Semple, and M.J. Armstrong, *How Useful Are Monogenic Rodent Models for the Study of Human Non-Alcoholic Fatty Liver Disease?* Front Endocrinol (Lausanne), 2016. **7**: p. 145.

54. Moffat, J.G., F. Vincent, J.A. Lee, J. Eder, and M. Prunotto, *Opportunities and challenges in phenotypic drug discovery: an industry perspective.* Nature Reviews Drug Discovery, 2017. **16**(8): p. 531-543.

55. Vincent, F., A. Nueda, J. Lee, M. Schenone, M. Prunotto, and M. Mercola, *Phenotypic drug discovery: recent successes, lessons learned and new directions.* Nat Rev Drug Discov, 2022.

56. Lefever, D.E., M.T. Miedel, F. Pei, J.K. DiStefano, R. Debiasio, T.Y. Shun, M. Saydmohammed, M. Chikina, L.A. Vernetti, A. Soto-Gutierrez, et al., *A Quantitative Systems Pharmacology Platform Reveals NAFLD Pathophysiological States and Targeting Strategies.* Metabolites, 2022. **12**(6).

57. Lee-Montiel, F.T., S.M. George, A.H. Gough, A.D. Sharma, J. Wu, R. DeBiasio, L.A. Vernetti, and D.L. Taylor, *Control of oxygen tension recapitulates zone-specific functions in human liver microphysiology systems.* Exp Biol Med (Maywood), 2017. **242**(16): p. 1617-1632.

58. Saydmohammed, M., A. Jha, V. Mahajan, D. Gavlock, T.Y. Shun, R. DeBiasio, D. Lefever, X. Li, C. Reese, E.E. Kershaw, et al., *Quantifying the progression of non-alcoholic fatty liver disease in human biomimetic liver microphysiology systems with fluorescent protein biosensors.* Exp Biol Med (Maywood), 2021. **246**: p. 2420-2441.

59. Gough, A., A. Soto-Gutierrez, L. Vernetti, M.R. Ebrahimkhani, A.M. Stern, and D.L. Taylor, *Human biomimetic liver microphysiology systems in drug development and precision medicine.* Nat Rev Gastroenterol Hepatol, 2021. **18**(4): p. 252-268.

60. Zerbino, D.R., P. Achuthan, W. Akanni, M R. Amode, D. Barrell, J. Bhai, K. Billis, C. Cummins, A. Gall, C.G. Girón, et al., *Ensembl 2018.* Nucleic Acids Research, 2017. **46**(D1): p. D754-D761.

61. Gerhard, G.S., C. Legendre, C.D. Still, X. Chu, A. Petrick, and J.K. DiStefano, *Transcriptomic Profiling of Obesity-Related Nonalcoholic Steatohepatitis Reveals a Core Set of Fibrosis-Specific Genes.* J Endocr Soc, 2018. **2**(7): p. 710-726.

62. Lefever, D. *Software for Selecting Repurposable Drugs using QSP*. 2021 05/13/21]; Available from: https://github.com/lefeverde/QSPpaper.

63. Liberzon, A., A. Subramanian, R. Pinchback, H. Thorvaldsdottir, P. Tamayo, and J.P. Mesirov, *Molecular signatures database (MSigDB) 3.0.* Bioinformatics, 2011. **27**(12): p. 1739-40.

64. Subramanian, A., R. Narayan, S.M. Corsello, D.D. Peck, T.E. Natoli, X. Lu, J. Gould, J.F. Davis, A.A. Tubelli, J.K. Asiedu, et al., *A Next Generation Connectivity Map: L1000 Platform and the First 1,000,000 Profiles.* Cell, 2017. **171**(6): p. 1437--1452.

65. Marinka Zitnik, R.S., Sagar Maheshwari, and J. Leskovec, *BioSNAP Datasets: Stanford Biomedical Network Dataset Collection*. 2018.

66. Wishart, D.S., Y.D. Feunang, A.C. Guo, E.J. Lo, A. Marcu, J.R. Grant, T. Sajed, D. Johnson, C. Li, Z. Sayeeda, et al., *DrugBank 5.0: a major update to the DrugBank database for 2018.* Nucleic Acids Res, 2018. **46**(D1): p. D1074-d1082.

67. Gerhard, G.S., C.D. Still, and J.K. DiStefano, *High False-Negative Rate for Nonalcoholic Steatohepatitis in Extreme Obesity.* Gastroenterology, 2016. **150**(1): p. 283-4.

68. Ahrens, M., O. Ammerpohl, W. von Schonfels, J. Kolarova, S. Bens, T. Itzel, A. Teufel, A. Herrmann, M. Brosch, H. Hinrichsen, et al., *DNA methylation analysis in nonalcoholic fatty liver disease suggests distinct disease-specific and remodeling signatures after bariatric surgery.* Cell Metab, 2013. **18**(2): p. 296-302.

69. Arendt, B.M., E.M. Comelli, D.W. Ma, W. Lou, A. Teterina, T. Kim, S.K. Fung, D.K. Wong, I. McGilvray, S.E. Fischer, et al., *Altered hepatic gene expression in nonalcoholic fatty liver disease is associated with lower hepatic n-3 and n-6 polyunsaturated fatty acids.* Hepatology, 2015. **61**(5): p. 1565-78.

70. Hoang, S.A., A. Oseini, R.E. Feaver, B.K. Cole, A. Asgharpour, R. Vincent, M. Siddiqui, M.J. Lawson, N.C. Day, J.M. Taylor, et al., *Gene Expression Predicts Histological Severity and Reveals Distinct Molecular Profiles of Nonalcoholic Fatty Liver Disease.* Scientific Reports, 2019. **9**(1): p. 12541.

71. Hotta, K., M. Kikuchi, T. Kitamoto, A. Kitamoto, Y. Ogawa, Y. Honda, T. Kessoku, K. Kobayashi, M. Yoneda, K. Imajo, et al., *Identification of core gene networks and hub genes associated with progression of non-alcoholic fatty liver disease by RNA sequencing.* Hepatol Res, 2017. **47**(13): p. 1445-1458.

72. Lefebvre, P., F. Lalloyer, E. Baugé, M. Pawlak, C. Gheeraert, H. Dehondt, J. Vanhoutte, E. Woitrain, N. Hennuyer, C. Mazuy, et al., *Interspecies NASH disease activity whole-*

genome profiling identifies a fibrogenic role of PPARα-regulated dermatopontin. JCI Insight, 2017. **2**(13).

73. Qian, T., N. Fujiwara, B. Koneru, A. Ono, N. Kubota, A.K. Jajoriya, M.G. Tung, E. Crouchet, W.M. Song, C.A. Marquez, et al., *Molecular Signature Predictive of Long-Term Liver Fibrosis Progression to Inform Antifibrotic Drug Development.* Gastroenterology, 2022. **162**(4): p. 1210-1225.

74. Govaere, O., S. Cockell, D. Tiniakos, R. Queen, R. Younes, M. Vacca, L. Alexander, F. Ravaioli, J. Palmer, S. Petta, et al., *Transcriptomic profiling across the nonalcoholic fatty liver disease spectrum reveals gene signatures for steatohepatitis and fibrosis.* Sci Transl Med, 2020. **12**(572).

75. Kiselev, V.Y., T.S. Andrews, and M. Hemberg, *Challenges in unsupervised clustering of single-cell RNA-seq data.* Nature Reviews Genetics, 2019. **20**(5): p. 273-282.

76. Bray, N.L., H. Pimentel, P. Melsted, and L. Pachter, *Near-optimal probabilistic RNA-seq quantification.* Nature Biotechnology, 2016. **34**: p. 525.

77. Soneson, C., M.I. Love, and M.D. Robinson, *Differential analyses for RNA-seq: transcript-level estimates improve gene-level inferences.* F1000Res, 2015. **4**: p. 1521.

78. Ritchie, M.E., B. Phipson, D. Wu, Y. Hu, C.W. Law, W. Shi, and G.K. Smyth, *limma powers differential expression analyses for RNA-sequencing and microarray studies.* Nucleic Acids Res, 2015. **43**(7): p. e47.

79. Law, C.W., Y. Chen, W. Shi, and G.K. Smyth, *voom: precision weights unlock linear model analysis tools for RNA-seq read counts.* Genome Biology, 2014. **15**(2): p. R29.

80. Leek, J.T. and J.D. Storey, *Capturing Heterogeneity in Gene Expression Studies by Surrogate Variable Analysis.* PLOS Genetics, 2007. **3**(9): p. e161.

81. Leek, J.T., W.E. Johnson, H.S. Parker, A.E. Jaffe, and J.D. Storey, *The sva package for removing batch effects and other unwanted variation in high-throughput experiments.* Bioinformatics, 2012. **28**(6): p. 882-3.

82. Hanzelmann, S., R. Castelo, and J. Guinney, *GSVA: gene set variation analysis for microarray and RNA-seq data.* BMC Bioinformatics, 2013. **14**: p. 7.

83. Subramanian, A., P. Tamayo, V.K. Mootha, S. Mukherjee, B.L. Ebert, M.A. Gillette, A. Paulovich, S.L. Pomeroy, T.R. Golub, E.S. Lander, et al., *Gene set enrichment analysis: A knowledge-based approach for interpreting genome-wide expression profiles.* Proceedings of the National Academy of Sciences, 2005. **102**(43): p. 15545-15550.

84. Han, J., M. Kamber, and J. Pei, *3 - Data Preprocessing*, in *Data Mining (Third Edition)*, J. Han, M. Kamber, and J. Pei, Editors. 2012, Morgan Kaufmann: Boston. p. 83-124.

85. Hennig, C., *Cluster-wise assessment of cluster stability.* Computational Statistics & Data Analysis, 2007. **52**(1): p. 258-271.

86. Bazick, J., M. Donithan, B.A. Neuschwander-Tetri, D. Kleiner, E.M. Brunt, L. Wilson, E. Doo, J. Lavine, J. Tonascia, and R. Loomba, *Clinical Model for NASH and Advanced Fibrosis in Adult Patients With Diabetes and NAFLD: Guidelines for Referral in NAFLD.* Diabetes Care, 2015. **38**(7): p. 1347-1355.

87. Portillo-Sanchez, P., F. Bril, M. Maximos, R. Lomonaco, D. Biernacki, B. Orsak, S. Subbarayan, A. Webb, J. Hecht, and K. Cusi, *High Prevalence of Nonalcoholic Fatty Liver Disease in Patients With Type 2 Diabetes Mellitus and Normal Plasma Aminotransferase Levels.* J Clin Endocrinol Metab, 2015. **100**(6): p. 2231-8.

88. Kwok, R., K.C. Choi, G.L. Wong, Y. Zhang, H.L. Chan, A.O. Luk, S.S. Shu, A.W. Chan, M.W. Yeung, J.C. Chan, et al., *Screening diabetic patients for non-alcoholic fatty liver disease with controlled attenuation parameter and liver stiffness measurements: a prospective cohort study.* Gut, 2016. **65**(8): p. 1359-68.

89. Zhu, C., K. Kim, X. Wang, A. Bartolome, M. Salomao, P. Dongiovanni, M. Meroni, M.J. Graham, K.P. Yates, A.M. Diehl, et al., *Hepatocyte Notch activation induces liver fibrosis in nonalcoholic steatohepatitis.* Sci Transl Med, 2018. **10**(468).

90. Zhao, X.K., L. Yu, M.L. Cheng, P. Che, Y.Y. Lu, Q. Zhang, M. Mu, H. Li, L.L. Zhu, J.J. Zhu, et al., *Focal Adhesion Kinase Regulates Hepatic Stellate Cell Activation and Liver Fibrosis.* Sci Rep, 2017. **7**(1): p. 4032.

91. Wang, J.N., L. Li, L.Y. Li, Q. Yan, J. Li, and T. Xu, *Emerging role and therapeutic implication of Wnt signaling pathways in liver fibrosis.* Gene, 2018. **674**: p. 57-69.

92. Sircana, A., E. Paschetta, F. Saba, F. Molinaro, and G. Musso, *Recent Insight into the Role of Fibrosis in Nonalcoholic Steatohepatitis-Related Hepatocellular Carcinoma.* Int J Mol Sci, 2019. **20**(7): p. 1745.

93. Ramachandran, P. and J.P. Iredale, *Macrophages: central regulators of hepatic fibrogenesis and fibrosis resolution.* J Hepatol, 2012. **56**(6): p. 1417-9.

94. Kennedy, L., L. Hargrove, J. Demieville, J.M. Bailey, W. Dar, K. Polireddy, Q. Chen, M.I. Nevah Rubin, A. Sybenga, S. DeMorrow, et al., *Knockout of l-Histidine Decarboxylase Prevents Cholangiocyte Damage and Hepatic Fibrosis in Mice Subjected to High-Fat Diet Feeding via Disrupted Histamine/Leptin Signaling.* Am J Pathol, 2018. **188**(3): p. 600-615.

95. Hintermann, E. and U. Christen, *The Many Roles of Cell Adhesion Molecules in Hepatic Fibrosis.* Cells, 2019. **8**(12): p. 1503.

96. Diedrich, T., S. Kummer, A. Galante, A. Drolz, V. Schlicker, A.W. Lohse, J. Kluwe, J.M. Eberhard, and J. Schulze Zur Wiesch, *Characterization of the immune cell landscape of patients with NAFLD.* PLoS One, 2020. **15**(3): p. e0230307.

97. Murphy, S.K., H. Yang, C.A. Moylan, H. Pang, A. Dellinger, M.F. Abdelmalek, M.E. Garrett, A. Ashley-Koch, A. Suzuki, H.L. Tillmann, et al., *Relationship between methylome and transcriptome in patients with nonalcoholic fatty liver disease.* Gastroenterology, 2013. **145**(5): p. 1076--1087.

98. Ratziu, V. and S.L. Friedman, *Why do so many NASH trials fail?* Gastroenterology, 2020: p. 1-9.

99. Keenan, A.B., S.L. Jenkins, K.M. Jagodnik, S. Koplev, E. He, D. Torre, Z. Wang, A.B. Dohlman, M.C. Silverstein, A. Lachmann, et al., *The Library of Integrated Network-Based Cellular Signatures NIH Program: System-Level Cataloging of Human Cells Response to Perturbations.* Cell Syst, 2018. **6**(1): p. 13-24.

100. Stanley, T.L., L.T. Fourman, M.N. Feldpausch, J. Purdy, I. Zheng, C.S. Pan, J. Aepfelbacher, C. Buckless, A. Tsao, A. Kellogg, et al., *Effects of tesamorelin on non-alcoholic fatty liver disease in HIV: a randomised, double-blind, multicentre trial.* Lancet HIV, 2019. **6**(12): p. e821-e830.

101. Fourman, L.T., J.M. Billingsley, G. Agyapong, S.J. Ho Sui, M.N. Feldpausch, J. Purdy, I. Zheng, C.S. Pan, K.E. Corey, M. Torriani, et al., *Effects of tesamorelin on hepatic transcriptomic signatures in HIV-associated NAFLD.* JCI Insight, 2020. **5**(16).

102. Sakolish, C., C.E. Reese, Y.S. Luo, A. Valdiviezo, M.E. Schurdak, A. Gough, D.L. Taylor, W.A. Chiu, L.A. Vernetti, and I. Rusyn, *Analysis of reproducibility and robustness of a human microfluidic four-cell liver acinus microphysiology system (LAMPS).* Toxicology, 2021. **448**: p. 152651.

103. Kanehisa, M. and S. Goto, *KEGG: kyoto encyclopedia of genes and genomes.* Nucleic Acids Res, 2000. **28**(1): p. 27-30.

104. Lamb, J., E.D. Crawford, D. Peck, J.W. Modell, I.C. Blat, M.J. Wrobel, J. Lerner, J.P. Brunet, A. Subramanian, K.N. Ross, et al., *The Connectivity Map: using gene-expression signatures to connect small molecules, genes, and disease.* Science, 2006. **313**(5795): p. 1929-35.

105. Chen, B., W. Wei, L. Ma, B. Yang, R.M. Gill, M.S. Chua, A.J. Butte, and S. So, *Computational Discovery of Niclosamide Ethanolamine, a Repurposed Drug Candidate That Reduces Growth of Hepatocellular Carcinoma Cells In Vitro and in Mice by Inhibiting Cell Division Cycle 37 Signaling.* Gastroenterology, 2017. **152**(8): p. 2022-2036.

106. Benjamini, Y. and Y. Hochberg, *Controlling the False Discovery Rate: A Practical and Powerful Approach to Multiple Testing.* Journal of the Royal Statistical Society. Series B (Methodological), 1995. **57**(1): p. 289-300.

107. Liu, J., J. Lee, M.A. Salazar Hernandez, R. Mazitschek, and U. Ozcan, *Treatment of obesity with celastrol.* Cell, 2015. **161**(5): p. 999-1011.

108. Guney, E., J. Menche, M. Vidal, and A.-L. Barábasi, *Network-based in silico drug efficacy screening.* Nature Communications, 2016. **7**: p. 10331 EP.

109. Kanehisa, M., M. Furumichi, M. Tanabe, Y. Sato, and K. Morishima, *KEGG: new perspectives on genomes, pathways, diseases and drugs.* Nucleic Acids Res, 2017. **45**(D1): p. D353-d361.

110. Vernetti, L.A., N. Senutovitch, R. Boltz, R. DeBiasio, T.Y. Shun, A. Gough, and D.L. Taylor, *A human liver microphysiology platform for investigating physiology, drug safety, and disease models.* Exp Biol Med (Maywood), 2016. **241**(1): p. 101-14.

111. Miedel, M.T., D.C. Gavlock, S. Jia, A. Gough, D.L. Taylor, and A.M. Stern, *Modeling the Effect of the Metastatic Microenvironment on Phenotypes Conferred by Estrogen Receptor Mutations Using a Human Liver Microphysiological System.* Sci Rep, 2019. **9**(1): p. 8341.

112. Schurdak, M., L. Vernetti, L. Bergenthal, Q.K. Wolter, T.Y. Shun, S. Karcher, D.L. Taylor, and A. Gough, *Applications of the microphysiology systems database for experimental ADME-Tox and disease models.* Lab Chip, 2020. **20**(8): p. 1472-1492.

113. Park, K.C., J.H. Park, J.Y. Jeon, S.Y. Kim, J.M. Kim, C.Y. Lim, T.H. Lee, H.K. Kim, H.G. Lee, S.M. Kim, et al., *A new histone deacetylase inhibitor improves liver fibrosis in BDL rats through suppression of hepatic stellate cells.* Br J Pharmacol, 2014. **171**(21): p. 4820-30.

114. Huang, H.M., S.J. Fan, X.R. Zhou, Y.J. Liu, X. Li, L.P. Liao, J. Huang, C.C. Shi, L. Yu, R. Fu, et al., *Histone deacetylase inhibitor givinostat attenuates nonalcoholic steatohepatitis and liver fibrosis.* Acta Pharmacol Sin, 2022. **43**(4): p. 941-953.

115. Shah, R.A. and K.V. Kowdley, *Obeticholic acid for the treatment of nonalcoholic steatohepatitis.* Expert Rev Gastroenterol Hepatol, 2020. **14**(5): p. 311-321.

116. Younossi, Z.M., V. Ratziu, R. Loomba, M. Rinella, Q.M. Anstee, Z. Goodman, P. Bedossa, A. Geier, S. Beckebaum, P.N. Newsome, et al., *Obeticholic acid for the treatment of non-alcoholic steatohepatitis: interim analysis from a multicentre, randomised, placebo-controlled phase 3 trial.* Lancet, 2019. **394**(10215): p. 2184-2196.

117. Musso, G., M. Cassader, E. Paschetta, and R. Gambino, *Thiazolidinediones and Advanced Liver Fibrosis in Nonalcoholic Steatohepatitis: A Meta-analysis.* JAMA Intern Med, 2017. **177**(5): p. 633-640.

118. Vega, G.L., J.J. Clarenbach, F. Dunn, and S.M. Grundy, *Oxandrolone enhances hepatic ketogenesis in adult men.* J Investig Med, 2008. **56**(7): p. 920-4.

119. Watanabe, M., R. Tozzi, R. Risi, D. Tuccinardi, S. Mariani, S. Basciani, G. Spera, C. Lubrano, and L. Gnessi, *Beneficial effects of the ketogenic diet on nonalcoholic fatty liver disease: A comprehensive review of the literature.* Obes Rev, 2020. **21**(8): p. e13024.

120. Luukkonen, P.K., S. Dufour, K. Lyu, X.M. Zhang, A. Hakkarainen, T.E. Lehtimäki, G.W. Cline, K.F. Petersen, G.I. Shulman, and H. Yki-Järvinen, *Effect of a ketogenic diet on hepatic steatosis and hepatic mitochondrial metabolism in nonalcoholic fatty liver disease.* Proc Natl Acad Sci U S A, 2020. **117**(13): p. 7347-7354.

121. Li, T.T., J.X. An, J.Y. Xu, and B.G. Tuo, *Overview of organic anion transporters and organic anion transporter polypeptides and their roles in the liver.* World J Clin Cases, 2019. **7**(23): p. 3915-3933.

122. Naik, A., A. Belič, U.M. Zanger, and D. Rozman, *Molecular Interactions between NAFLD and Xenobiotic Metabolism.* Front Genet, 2013. **4**: p. 2.

123. Cave, M.C., H.B. Clair, J.E. Hardesty, K.C. Falkner, W. Feng, B.J. Clark, J. Sidey, H. Shi, B.A. Aqel, C.J. McClain, et al., *Nuclear receptors and nonalcoholic fatty liver disease.* Biochim Biophys Acta, 2016. **1859**(9): p. 1083-1099.

124. Sayaf, K., I. Zanotto, F.P. Russo, D. Gabbia, and S. De Martin, *The Nuclear Receptor PXR in Chronic Liver Disease.* Cells, 2021. **11**(1): p. 61.

125. Xu, G., S. Fu, X. Zhan, Z. Wang, P. Zhang, W. Shi, N. Qin, Y. Chen, C. Wang, M. Niu, et al., *Echinatin effectively protects against NLRP3 inflammasome-driven diseases by targeting HSP90.* JCI Insight, 2021. **6**(2): p. 1-17.

126. Nakagami, H., M. Shimamura, T. Miyake, T. Shimosato, N. Minobe, T. Moritani, M. Kiomy Osako, F. Nakagami, H. Koriyama, M. Kyutoku, et al., *Nifedipine prevents hepatic fibrosis in a non-alcoholic steatohepatitis model induced by an L-methionine-and choline-deficient diet.* Mol Med Rep, 2012. **5**(1): p. 37-40.

127. Lee, S., D. Han, H.G. Kang, S.J. Jeong, J.E. Jo, J. Shin, D.K. Kim, and H.W. Park, *Intravenous sustained-release nifedipine ameliorates nonalcoholic fatty liver disease by restoring autophagic clearance.* Biomaterials, 2019. **197**: p. 1-11.

128. Doumas, M., K. Imprialos, A. Dimakopoulou, K. Stavropoulos, A. Binas, and V.G. Athyros, *The Role of Statins in the Management of Nonalcoholic Fatty Liver Disease.* Curr Pharm Des, 2018. **24**(38): p. 4587-4592.

129. Lee, J.I., H.W. Lee, K.S. Lee, H.S. Lee, and J.Y. Park, *Effects of Statin Use on the Development and Progression of Nonalcoholic Fatty Liver Disease: A Nationwide Nested Case-Control Study.* Am J Gastroenterol, 2021. **116**(1): p. 116-124.

130. Oladimeji, P.O. and T. Chen, *PXR: More Than Just a Master Xenobiotic Receptor.* Mol Pharmacol, 2018. **93**(2): p. 119-127.

131. Hundertmark, J. and F. Tacke, *How effective are nonalcoholic fatty liver disease models for drug discovery?* Expert Opin Drug Discov, 2020. **15**(11): p. 1237-1240.

132. Zhang, C., L.W. Jing, Z.T. Li, Z.W. Chang, H. Liu, Q.M. Zhang, and Q.Y. Zhang, *Identification of a prognostic 28-gene expression signature for gastric cancer with lymphatic metastasis.* Biosci Rep, 2019. **39**(5).

133. Geeleher, P., N.J. Cox, and R.S. Huang, *Clinical drug response can be predicted using baseline gene expression levels and in vitro drug sensitivity in cell lines.* Genome Biology, 2014. **15**(3): p. R47.

134. Barretina, J., G. Caponigro, N. Stransky, K. Venkatesan, A.A. Margolin, S. Kim, C.J. Wilson, J. Lehár, G.V. Kryukov, D. Sonkin, et al., *The Cancer Cell Line Encyclopedia enables predictive modelling of anticancer drug sensitivity.* Nature, 2012. **483**(7391): p. 603-607.

135. Salvadores, M., F. Fuster-Tormo, and F. Supek, *Matching cell lines with cancer type and subtype of origin via mutational, epigenomic, and transcriptomic patterns.* Sci Adv, 2020. **6**(27).

136. Teufel, A., T. Itzel, W. Erhart, M. Brosch, X.Y. Wang, Y.O. Kim, W. von Schönfels, A. Herrmann, S. Brückner, F. Stickel, et al., *Comparison of Gene Expression Patterns Between Mouse Models of Nonalcoholic Fatty Liver Disease and Liver Tissues From Patients.* Gastroenterology, 2016. **151**(3): p. 513-525.e0.

137. Law, C.W., K. Zeglinski, X. Dong, M. Alhamdoosh, G.K. Smyth, and M.E. Ritchie, *A guide to creating design matrices for gene expression experiments.* F1000Res, 2020. **9**: p. 1444.

138. Friedman, J., T. Hastie, and R. Tibshirani, *Regularization Paths for Generalized Linear Models via Coordinate Descent.* J Stat Softw, 2010. **33**(1): p. 1-22.

139. Lee, K., A. Haddad, A. Osme, C. Kim, A. Borzou, S. Ilchenko, D. Allende, S. Dasarathy, A. McCullough, R.G. Sadygov, et al., *Hepatic Mitochondrial Defects in a Nonalcoholic Fatty Liver Disease Mouse Model Are Associated with Increased Degradation of Oxidative Phosphorylation Subunits.* Mol Cell Proteomics, 2018. **17**(12): p. 2371-2386.

140. Francque, S., G. Szabo, M.F. Abdelmalek, C.D. Byrne, K. Cusi, J.-F. Dufour, M. Roden, F. Sacks, and F. Tacke, *Nonalcoholic steatohepatitis: the role of peroxisome proliferator-activated receptors.* Nature Reviews Gastroenterology & Hepatology, 2021. **18**(1): p. 24-39.

141. Lake, A.D., P. Novak, P. Shipkova, N. Aranibar, D.G. Robertson, M.D. Reily, L.D. Lehman-McKeeman, R.R. Vaillancourt, and N.J. Cherrington, *Branched chain amino acid metabolism profiles in progressive human nonalcoholic fatty liver disease.* Amino Acids, 2015. **47**(3): p. 603-615.

142. Yang, H., M. Arif, M. Yuan, X. Li, K. Shong, H. Türkez, J. Nielsen, M. Uhlén, J. Borén, C. Zhang, et al., *A network-based approach reveals the dysregulated transcriptional regulation in non-alcoholic fatty liver disease.* iScience, 2021. **24**(11): p. 103222.

143. Collin de l'Hortet, A., K. Takeishi, J. Guzman-Lepe, K. Morita, A. Achreja, B. Popovic, Y. Wang, K. Handa, A. Mittal, N. Meurs, et al., *Generation of Human Fatty Livers Using Custom-Engineered Induced Pluripotent Stem Cells with Modifiable SIRT1 Metabolism.* Cell Metab, 2019. **30**(2): p. 385-401.e9.

144. Smyth, G.K., *Linear models and empirical bayes methods for assessing differential expression in microarray experiments.* Stat Appl Genet Mol Biol, 2004. **3**(1): p. 1-28.

145. Li, X., S.M. George, L. Vernetti, A.H. Gough, and D.L. Taylor, *A glass-based, continuously zonated and vascularized human liver acinus microphysiological system (vLAMPS) designed for experimental modeling of diseases and ADME/TOX.* Lab Chip, 2018. **18**(17): p. 2614-2631.

Appendix

Data files and Supplementary materials

The individual legends for the supplemental tables, data files, and figures (available for download at: http://d-scholarship.pitt.edu/44129/) are in the subsequent pages. The raw data for this project can be found at: http://d-scholarship.pitt.edu/id/eprint/44130

Figure S1. NAFLD associated protein interactome (link to file).

A subnetwork of the human liver protein interactome involving NAFLD associated protein-protein interactions. The indicated nodes represent those proteins encoded by the DEGs among the pairwise comparisons for the three clusters defined in **Figure 5**. The degrees of these nodes are shown in **Data file S6** and the 20 hubs with the highest degrees are shown in **Table 7**.

Table S1. The differentially enriched pathways across 7 NAFLD categories for each pairwise cluster and clinical classification comparison (Link to excel file).

Data file S1 was used to create these tables. The excel file consists of 6 sheets: PLI vs. PN&S, PF vs. PN&S, PF vs. PLI, Lob vs N&S, Fib vs N&S, and Fib vs Lob comparisons. The columns of the tables are as follows:

- KEGG Pathway name and ID
- KEGG pathway group
- KEGG pathway subgroup
- NAFLD categorization of KEGG pathway (see **Methods**)
    - C1: Insulin resistance and oxidative stress
    - C2: cell stress, apoptosis and lipotoxicity
    - C3: Inflammation
    - C4: Fibrosis
    - C5: Disease related pathways
    - C6: Other associated pathways
    - C7: No established relationship
- log2 Fold change: estimate of the log2-fold-change of the comparison
- FDR corrected *p*-value: False discovery rate
- PMIDs: The PMIDs for the references which support the NAFLD categorization

Data file S1. Differentially enriched pathways for each pairwise cluster and clinical classification comparison (Link to csv file).

These results were used to create **Table S1**, the gene signatures (**Table 3; Data file S3**).

See **Methods** for details**.** The columns of this file are as follows:

- comparison: The pairwise comparison
- pathway_name:
- id: KEGG pathway ID
- KEGG pathway group
- KEGG pathway subgroup
- nafld_categories: Denotes the involvement of the pathway in NAFLD pathophysiology (see **Methods**).
    - C1: Insulin resistance and oxidative stress
    - C2: cell stress, apoptosis and lipotoxicity
    - C3: Inflammation
    - C4: Fibrosis
    - C5: Disease related pathways
    - C6: Other associated pathways
    - C7: No established relationship
- logFC: estimate of the log2-fold-change of the comparison (see limma documentation)
- CI.L: LogFC 95% confidence interval lower limit (see limma documentation)
- CI.R: LogFC 95% confidence interval upper limit (see limma documentation)
- AveExpr: average log2-expression across all (see limma documentation)
- t: moderated t-statistic (see limma documentation and Smyth [144])
- P.Value: raw *p*-value (see limma documentation)
- adj.P.Val: FDR corrected *p*-value (see limma documentation)
- B: log-odds that the gene is differentially expressed (see limma documentation)
- pmids: The PMIDs for the references which support the NAFLD categorization

Data file S2. DEGs resulting for each pairwise cluster and clinical classification comparisons (Link to csv file).

These results were used in the creation of gene signatures (**Table 3; Data file S3**) and NAFLD subnetwork (**Figure 16**, **Table 7; Data file S6**). The columns of this file are as follows:

- comparison: The pairwise comparison
- gene_symbol: Common gene name
- Entrez gene ID
- Ensembl gene ID
- logFC: estimate of the log2-fold-change of the comparison (see limma documentation)
- CI.L: LogFC 95% confidence interval lower limit (see limma documentation)
- CI.R: LogFC 95% confidence interval upper limit (see limma documentation)
- AveExpr: average log2-expression across all samples (see limma documentation)
- t: moderated t-statistic (see limma documentation and Smyth [144])
- P.Value: raw *p*-value (see limma documentation)
- adj.P.Val: FDR corrected p-value (see limma documentation)
- B: log-odds that the gene is differentially expressed (see limma documentation)
- kegg_pathway_names: The names of the KEGG pathways that the gene is a member of (if applicable, NA otherwise)
- kegg_pathway_ids: The pathway ids the KEGG pathways that the gene is a member of (if applicable, NA otherwise)

Data file S3. Gene signatures used for CMap analysis (Link to csv file).

The data from **Data files S1-S2** were used to create this file (see **Methods**). It was used for CMap drug prediction (**Tables 4 & 5; Data file S4-S5**, see **Methods** for details on the methodology). The columns are as follows:

- gene_sig_idx: The gene signature index (see **Table 3** and **Data file S3**)
- comparison: The pairwise comparison
- nafld_pathway_category: The NAFLD category of differentially enriched pathways that was used to create the gene signature (see **Methods**), The values are defined as follows:
    - C1: Insulin resistance and oxidative stress
    - C2: cell stress, apoptosis and lipotoxicity
    - C3: Inflammation
    - C4: Fibrosis
- up-regulated_gene_names: List of the upregulated genes (using common gene name) for the signature
- up-regulated_entrez_ids: List of the upregulated genes (using entrez gene id) for the signature
- down-regulated_gene_names: List of the down-regulated genes (using common gene name) for the signature
- down-regulated_entrez_ids: List of the down-regulated genes (using entrez gene id) for the signature

Data file S4. CMAP scores of small molecules with a DrugBank ID for the 24 queries described in the Methods (Link to csv file).

These results were used to create **Table 4 & 5** (see **Methods** for details). columns are as follows:

- gene_sig_idx: The gene signature index (see **Table 3** and **Data file S3**)
- comparison: The pairwise comparison
- nafld_pathway_category: The NAFLD category of differentially enriched pathways that was used to create the gene signature (see **Methods**), The values are defined as follows:
    - C1: Insulin resistance and oxidative stress
    - C2: cell stress, apoptosis and lipotoxicity
    - C3: Inflammation
    - C4: Fibrosis
- sig_id: The L100 perturbation instance signature id (see the GEO CMap LINCS user guide for more information)
- lincs_db: The database (2017, 2020, or both) from which the perturbation instance originates
- pert_id: The Broad's internal drug/small molecule ID (see the GEO CMap LINCS user guide for more information)
- pert_iname: The Broad's drug/small molecule common name (see the GEO CMap LINCS user guide for more information)
- drugbank_id: DrugBrank's drug/small molecule ID
- targets: The drug/small molecule targets from DrugBank v5.1.4
- cmap_score: The CMap score (see **Methods** and [64, 104])
- p_value: *P*-value calculated by permutation testing (see Chen et al[105])
- fdr_*p*-value: False discovery rate corrected *p*-value

Data file S5. List of top 20 CMap predictions from both the 2017 & 2020 LINCS databases and both ranking methods ("Best score" and "Percentile score") from the 24 signatures (link to file).

These results were created from **Data file S4** and were used to create **Table 4** and **Table 5.** The columns are as follows:

- gene_sig_idx: The gene signature index (see **Table 3** and **Data file S3**)
- comparison: The pairwise comparison
- nafld_pathway_category: The NAFLD category of differentially enriched pathways that was used to create the gene signature (see **Methods**), The values are defined as follows:
    - C1: Insulin resistance and oxidative stress
    - C2: cell stress, apoptosis and lipotoxicity
    - C3: Inflammation
    - C4: Fibrosis
- lincs_db: The database (2017 either 2020) from which the perturbation instance originates
- pert_id: The Broad's internal drug/small molecule ID (see the GEO CMap LINCS user guide for more information)
- pert_iname: The Broad's drug/small molecule common name (see the GEO CMap LINCS user guide for more information)
- drugbank_id: DrugBrank's drug/small molecule ID
- summary_stat: Which compound-centric statistic used to rank the compounds (either best_score or prct_67th_score, see **Methods**)
- drug_rank: Relative rank of the compound prediction within the gene signature
- pert_sum_score: The summary score used to rank the compound (see **Methods**)

Data file S6. Degree of the nodes in the NAFLD subnetwork (Link to csv file).

These results are discussed in the **3.3 Results** of the main text and supports **Table 7.** The columns are as follows:

- gene_symbol: The common gene name
- gene_description
- Entrez_gene_id
- degree_liver: The number of connections this protein has to other nodes in the human liver interactome
- degree_nafld_DEGs: The number of connections the encoded protein has with other DEG encoded nodes in the NAFLD associated network

Data file S7. Network proximity determined Z-scores for the highest ranking CMap-predicted drugs with targets mapping to the NAFLD subnetwork (Link to csv file).

These results were used for **Table 8**. The columns are as follows:

- drug_name: Common name of the drug/small molecule
- drugbank_id: DrugBank ID of the drug/small molecule
- z: Z-score of the normalized distance of drug subnetwork to disease associated subnetwork (See **Methods**, [108])
- d: Shortest distance of drug subnetwork to disease associated subnetwork (See **3.2 Methods**, [108])
- mean: Average distance of a reference network to disease associated subnetwork (See **3.2 Methods**, [108])
- sd: Standard deviation of a reference network to disease associated subnetwork (See **3.2 Methods**, [108])

Data file S8. DEGs resulting from the LAMPS pairwise comparisons (EMS vs NF, LMS vs NF, LMS vs EMS) (Link to csv file).

These results were used to create **Data file S9.** The columns of this file are as follows:

- comparison: The pairwise comparison
- gene_symbol: Common gene name
- Entrez gene ID
- Ensembl gene ID
- logFC: estimate of the log2-fold-change of the comparison (see limma documentation)
- CI.L: LogFC 95% confidence interval lower limit (see limma documentation)
- CI.R: LogFC 95% confidence interval upper limit (see limma documentation)
- AveExpr: average log2-expression across all samples (see limma documentation)
- t: moderated *t*-statistic (see limma documentation and Smyth [144])
- P.Value: raw *p*-value (see limma documentation)
- adj.P.Val: FDR corrected *p*-value (see limma documentation)
- B: log-odds that the gene is differentially expressed (see limma documentation)
- kegg_pathway_names: The names of the KEGG pathways that the gene is a member of (if applicable, NA otherwise)
- kegg_pathway_ids: The pathway ids the KEGG pathways that the gene is a member of (if applicable, NA otherwise)

Data file S9. Differentially enriched pathways the LAMPS pairwise comparisons (EMS vs NF, LMS vs NF, LMS vs EMS) (Link to csv file).

These results along with **Data file S1** were used for **Figure 16.** See **4.2 Methods** for details**.**

The columns of this file are as follows:

- comparison: The pairwise comparison
- pathway_name:
- id: KEGG pathway ID
- KEGG pathway group
- KEGG pathway subgroup
- nafld_categories: Denotes the involvement of the pathway in NAFLD pathophysiology (see **4.2 Methods**).
  - C1: Insulin resistance and oxidative stress
  - C2: cell stress, apoptosis and lipotoxicity
  - C3: Inflammation
  - C4: Fibrosis
  - C5: Disease related pathways
  - C6: Other associated pathways
  - C7: No established relationship
- NES: normalized enrichment score (see clusterProfiler documentation)
- pvalue: uncorrected p-value from permutation testing (see clusterProfiler documentation)
- p.adjust: FDR corrected *p*-values (see clusterProfiler documentation)

Data file S10. The 71 features selected by the final MLENet model (Link to csv file).

These results were used to supplement **Figure 14.** See **4.2 Methods** for details**.** The columns of this file are as follows:

- class: the patient clinical classification (Normal, Steatosis, Lobular inflammation, or Fibrosis)
- ensembl_gene_id
- gene_name
- Entrez gene ID
- estimate: the feature coefficients (i.e., association with each class) estimated by MLENet (see glmnet documentation)
- prior_nafld_association: The PMIDs for papers references associating the feature with NAFLD or comparative toxicogeneomics database disease association

Supplementary Methods

Cell sources and culture

A single lot of selected cryopreserved primary human hepatocytes (lot# HU1960) with >90% viability and re-plating efficiency post-thaw were purchased from ThermoFisher. Human liver sinusoidal endothelial cells (LSECs) were purchased from LifeNet Health. The human monoblast cell line, THP-1, used to generate Kupffer cells, was purchased from ATCC and LX-2 human stellate cells were purchased from EMD Millipore. LSECs were cultured in endothelial cell basal medium-2 (EBM-2) supplemented with the endothelial growth medium-2 (EGM-2) supplement pack (Lonza). THP-1 cells were cultured in suspension in RPMI-1640 medium (ThermoFisher) supplemented with 10% fetal bovine serum (FBS; ThermoFisher), 100 µg/mL penicillin streptomycin (ThermoFisher), and 2 mM L-glutamine (ThermoFisher). THP-1 cells were differentiated into mature macrophages by treatment with 200 ηg/mL phorbol myristate acetate (Sigma Aldrich) for 48 h. LX-2 cells were cultured in Dulbecco's Modified Eagle Medium (DMEM; ThermoFisher) supplemented with 2% FBS and 100 µg/mL penicillin streptomycin.

Normal fasting and Early Metabolic Syndrome (EMS) media.

We recently developed MPS culture media conditions to create disease progression from Normal Fasting (NF) to early metabolic syndrome (EMS) over a two-week period in the LAMPS platform [58] that recapitulates key features of the NAFLD disease process. We developed the media around Williams E media that did not have glucose, insulin, glucagon, oleic acid, palmitic acid and then adjusted these components to reflect the pathophysiological conditions.

Normal Fasting (NF) Media: NF media was prepared in a custom formulation of William's E medium without glucose (ThermoFisher) supplemented with 5.5 mM glucose (Sigma Millipore), 1% FBS (Corning), 0.125 g/mL bovine serum albumin (Sigma), 0.625 mg/mL human transferrin, 0.625 µg/mL selenous acid, 0.535 mg/mL linoleic acid (Sigma), 100 nM dexamethasone (ThermoFisher), 2 mM glutamax, 15 mM HEPES (ThermoFisher), 100 U/100 µg/mL pen/ strep (Hyclone Labs), 10 pM insulin (ThermoFisher) and 100 pM glucagon (Sigma).

EMS Media: Early metabolic syndrome (EMS) medium was derived from the NF media formulation with the following modifications: 11.5 mM glucose, 10 nM insulin, 30 pM glucagon, 200 µM sodium oleate (Sigma) and 100 µM palmitate (Cayman Chemical Company).

LAMPS model assembly and maintenance workflow.

Day -3:

(a) *Mixed matrix coating of MPS devices:* The interior of the devices was dried under vacuum prior to protein coating with 100 µg/mL bovine fibronectin (Sigma Millipore) and 150 µg/mL rat-tail collagen, type 1(Corning), in PBS for 1 h at room temperature. The collagen/fibronectin solution was then removed, and devices were filled with PBS and stored at 4°C until use.

(b) *Differentiation of THP-1 cells:* THP-1 cells were treated with 200 ηg/mL phorbol myristate acetate (PMA; Sigma Millipore) to facilitate their differentiation into mature macrophages for seeding into LAMPS models on Day -1 (48 h treatment).

Day -2:

(a) *Hepatocyte seeding:* Cryopreserved hepatocytes were thawed following the manufacturer's recommendations. Hepatocytes were pelleted at 100 x g for 10 minutes using Cryopreserved Hepatocyte Recovery Medium (CHRM; ThermoFisher), and then resuspended at 2.75 x 10^6 hepatocytes/mL in hepatocyte plating media (HPM). Hepatocyte cell solution was then injected into the interstitial compartment of the device for overnight incubation at 37°C to allow for cell adherence and spreading.

Day -1:

(a) *LECM coating of MPS devices:* HPM was removed from the device and a solution of 400 µg/ml of porcine liver extracellular matrix prepared in NF media (LECM; a kind gift from Dr. Stephen Badylak's laboratory at the McGowan Institute for Regenerative Medicine, University of Pittsburgh) was added and incubated for 3 h at 37°C to create a thin matrix layer on top of the hepatocytes to mimic the Space of Disse.

(b) *LSEC and THP-1 seeding:* During the LECM incubation, LSEC and THP-1 cell suspensions are prepared in NF media for seeding into LAMPS. LSECs were thawed and a cell suspension was prepared at a concentration of 3.0 x 10^6 cells/mL. Differentiated THP-1 cells were prepared at a concentration of 1.6 x 10^6 cells/mL. The individual cell solutions were combined at a 1:1 ratio to yield final cell concentrations of 1.5 x 10^6 (LSEC) and 0.8 x 10^6 (THP-1) cells/mL. LECM solution was removed by gentle aspiration using a 1 mL syringe with a blunt needle (Fisher Scientific) and the LSEC/THP-1 cell solution was injected into each device and incubated for 2 h at 37°C.

(c) *Collagen/LX-2 overlay:* LX-2 cells were prepared at a concentration of 0.2 x 10^6 cells/mL and were suspended in 1 mL of a 2.5 mg/mL solution of pH 7.2 collagen I/10 mM HEPES/HBSS and injected into devices. The devices were then inverted for 1 h at 37°C during collagen polymerization to ensure an initial spatial separation of hepatocytes and LX-2 stellate cells. The devices were then re-inverted and incubated overnight at 37°C. The collagen overlay functions to maintain hepatocyte morphology and functionality over extended culture time.

Day 0:

(a) *Establishment of flow:* The next day, flow was initiated using pressure driven pumps (KD Scientific) to perfuse media in glass syringes (Hamilton) at a flow rate of 5 (3-6% O_2) μL/hour to achieve a target oxygen concentration of 3-6% O_2, corresponding to zone 3 (hepatic venule) oxygen levels, as previously described [57]. Devices were then maintained for 10 days at this flow rate.

(b) *Drug testing in LAMPS.* For drug studies, EMS media was prepared as described above and supplemented with the indicated concentration of drug (0.1% DMSO v/v final concentration). EMS media containing drug was added at Day 0 during the initiation of flow for the duration of the experimental time course. The followingdrug treatments were used in these studies: 10 μM obeticholic acid (Selleck Chemicals), 30 μM pioglitazone (Selleck Chemicals), and 1.7 μM or 5 μM vorinostat (Selleck Chemicals). For drug combination studies, 30 μM pioglitrazone was combined with either 1.7 μM or 5 μM vorinostat for the duration of the experimental time course.

Drug binding/recovery in PDMS-containing LAMPS device. To assess the drug binding capability of the polydimethylsiloxane (PDMS)-containing LAMPS device for compounds used in these studies, we used perfusion flow tests and mass spectrometry analysis of efflux collected from LAMPS devices at 72 h to determine the overall effective concentration of each compound compared to the starting concentration of drug as previously described [110, 111]. Briefly, Nortis devices were coated for 1h at RT with 150 µg/mL collagen I and 100 µg/mL fibronectin solution in PBS. Following this, the collagen/fibronection solution was removed and devices were washed 2x with sterile PBS. A 2.5 mg/mL collagen I overlay solution was prepared in perfusion media and injected into each device where they were incubated at 37°C o/n. The next day, drug solutions were prepared at the desired concentrations in EMS media for each compound and loaded into 10 mL glass syringes. A flow rate of 15 µl/h was established, and efflux media was collected at 24, 48, and 72 h of flow and the amount of compound at the 72 h time point was compared to the amount of drug present from the starting solution. Mass spectrometry was then performed by the University of Pittsburgh Small Molecule Biomarker Core where data was collected with a Waters Acquity UPLC (Milford, MA) C18, 1.7 µm, 2.1 X 100 mm reversed-phase column. Separation was carried out in an acetonitrile: water (0.1% formic acid) gradient and detection and quantitation were achieved in the positive ion mode with a TSQ Quantum Ultra Mass Spectrometer interfaced via an electrospray ionization (ESI) probe. Recovery was calculated as the ratio of Efflux Area Under Curve/Influx Area Under Curve.

5 Day Cytotoxicity Assay. Primary human hepatocytes (Thermo Fisher lot Hu1981) were thawed and resuspended in Hepatocyte Recovery Media (Thermo Fisher CM4000). Viable hepatocytes were collected by centrifugation (100g X 11 minutes). The supernate was removed by aspiration and the hepatocyte pellet resuspended in Hepatocyte Plating Media, counted and then 14,000 hepatocytes/well (560,000 hepatocytes/ml) were seeded at into a collagen 1 pre-coated 384 well microtiter plate (Becton Dickinson). The cells were allowed overnight attachment and spreading. The plate was decanted before 25 µl of 1.5% gelling collagen 1/NF media solution added to each well. The gel polymerized 1 hour (37° C, 5% CO_2) before the addition of 25 µl microtiter plate with NF media ± 2X concentration of compound. The plate was incubated 5 days with a single replenishment of 25 µl NF media ± 1X concentration of compound added to each well at 48 hr. Cytotoxicity was assessed by propidium iodide uptake assay. A 4X solution of propidium iodide (PI) and Hoechst nuclear dye was prepared in NF media at 8 µg/ml Hoechst and 20 µg/ml PI. 25 µl of the PI/Hoechst solution was added to each well for 1 hour. Fluorescent images were collected for Hoechst (405/488 ex/em) and PI (488/530 ex/em) using a High Content Screening (HCS) instrument. The compartment analysis algorithm software of the HCS was used to quantitate the intensity of PI co-localized within the nucleus and calculate the % of PI positive hepatocytes.

Secretome measurements. Efflux media from LAMPS devices was collected on days 2,4,6,8, and 10 to measure albumin, blood urea nitrogen, and lactate dehydrogenase. The enzyme linked immunosorbent assay (ELISA) for albumin was purchased from Bethyl Laboratories. The CytoTox 96 for lactate dehydrogenase (LDH) and the urea nitrogen test were purchased from Promega and Stanbio Laboratory, respectively. Collagen 1A1 (R&D Systems and TIMP-1 ELISA measurements were made from day 10 efflux only. All efflux measurements were obtained as described previously [57, 110, 111, 145].

Steatosis measurements. Steatosis measurements were performed after completion of the experimental time course (Day 10) in LAMPS models as previously described [57, 58]. Cells were fixed with 4% paraformaldehyde in PBS for 30 min then washed twice with PBS for 10 min. Following fixation, HCS LipidTOX Deep Red Neutral Lipid Stain (ThermoFisher) was diluted 1:500 in PBS and perfused into devices and incubated overnight at 4°C. The following day, devices were washed twice with PBS and then incubated for 15 min with 5 µg/mL Hoechst (ThermoFisher) to label nuclei. Images were collected with a Nikon 20x (0.45 NA) objective using the IN Cell Analyzer 6000 (GE Healthcare) in confocal mode using the 405 nm (Hoechst) and 640 nm

(LipidTOX) lasers and associated filter sets with the aperture set to 1 airy unit and were acquired with a sCMOS 5.5 Mp camera (2560 x 2160 pixels). Images for each media treatment were acquired using the same exposure time (100 ms) and laser power (80%) settings to ensure that intensity values were ~50-75% of the total dynamic range of the InCell system (65,000 bits). Additionally, imaging parameters were set using the EMS media vehicle control because this condition served as the positive control, demonstrating the most LipidTOX staining. Z-stacks totaling 100 µm distance (5 µm spacing between slices) were obtained and then imported into FIJI (ImageJ) to generate maximum intensity projections. Lipid droplets were identified using FIJI by interactive selection of a threshold (default method) using uniform intensity minimum (background) and intensity maximum values across the image sets. Watershed segmentation and the analyze particles function was then used to measure the total lipid intensity in each device. Intensity values were then normalized on a per cell basis by counting the total number of Hoechst-positive nuclei per field using the cell counting function in FIJI. A total of 10 images per device were collected from n =3 devices for each experimental condition. Statistical significance of LipidTOX labeling was assessed using a One-Way ANOVA with Tukey's multiple comparisons test to make comparisons between each control and drug treatment group, where *p*-values less than 0.05 were considered statistically significant.

Stellate cell activation. Staining for LX-2 cell expression of α-smooth muscle actin (α-SMA) was performed after completion of the experimental time course (Day 10) in LAMPS models as previously described [58]. Cells were fixed with 4% paraformaldehyde in PBS for 30 min, washed twice with PBS for 10 min, then were permeabilized for 30 min. with 0.1% TX-100 in PBS and blocked for an additional 1 h in PBS containing 1% BSA. Mouse monoclonal anti-α-

SMA antibody (Sigma Millipore) was diluted 1:100 in PBS containing 0.5% BSA and was incubated overnight at 4°C. The primary antibody was rinsed 3 times for 15 min. with PBS before the cells were then incubated for 1 h with Alexa FluorÒ Goat anti-mouse 555 (ThermoFisher) secondary antibody diluted 1:250 in PBS. The secondary antibody solution was removed, and cells were incubated for 15 min with PBS containing 5 µg/mL Hoechst and then washed 2 more times for 10 minutes with PBS. Images were collected with a Nikon 20x (0.45 NA) objective using the IN Cell Analyzer 6000 (GE Healthcare) in confocal mode using the 405 nm (Hoechst) and 561 nm (α-SMA) lasers and associated filter sets with the aperture set to 1 airy unit. Images for each media treatment were acquired using the same exposure time and laser power settings. Z-stacks totaling 100 µm distance (5 µm spacing between slices) were obtained and then imported into FIJI to generate maximum intensity projections. Image analysis of LX-2 α-SMA expression was quantified using an interactive selection of threshold (Default mode) to mask α-SMA-specific fluorescence. The analyze particles function was then used with a size exclusion setting of 100 µm^2 to exclude non-specific staining to measure the integrated intensity of α-SMA expression. A total of 10 images per device were collected from n = 3 devices for each experimental condition. Statistical significance of α-SMA intensity was assessed using a One-Way ANOVA with Tukey's multiple comparisons test test to make comparisons between each control and drug treatment group, where *p*-values less than 0.05 were considered statistically significant.

Multiplex immunoassays. Day 10 efflux media from LAMPS devices was collected for each drug treatment group and the levels of various human cytokines (IL-1b, IL-6, IL-8, TNF-a, and MCP-1) were assayed using a custom version (5-plex) of the Human XL Cytokine Discovery Panel (R&D systems). Assays were completed according to the manufacturer's instructions at The

University of Pittsburgh Cancer Proteomics Facility Luminex® Core Laboratory. All multiplex panels were run at the same time to avoid run-to-run and operator error variability utilizing the xMAP platform licensed by Luminex®. All the cytokine target profiling experiments were performed from efflux obtained from $n = 3$ devices for each drug treatment condition. Statistical significance of cytokine secretion between treatment groups was assessed using a One-Way ANOVA with Dunnett's test to make comparisons between each drug treatment group and the vehicle control, where p values less than 0.05 were considered statistically significant.